ABSTRACT

Title of dissertation: SWITCHING AND SCALING EFFECTS IN FERROELECTRIC CAPACITORS

Sanwarit Prasertchoung, Doctor of Philosophy, 2006

Dissertation directed by: Professor Ramamoorthy Ramesh
Department of Materials Science and Engineering

Ferroelectric materials are one of the most attractive candidates for the next generation of nonvolatile memories due to their unique properties such as spontaneous polarization, low operating voltage, and high fatigue resistance. In the development of high density ferroelectric memories, the density must be increased by reducing both lateral and thickness dimensions occupied by a memory capacitor. At the same time, sufficient and stable ferroelectric properties must be maintained. Therefore, it is desirable to investigate size effects, which can disturb the ferroelectric properties, both experimentally and theoretically, and evaluate the fundamental aspects governing the scaling. In this dissertation, the switching behavior of ferroelectric materials was investigated as a function of capacitor lateral size and film thickness.

To investigate the properties, a novel method of atomic force microscopy and pulse switching measurement was used, where an atomic force microscope was used for making an electrical contact with a submicron capacitor top electrode, and the pulse switching setup was used to provide the testing conditions simulating the operation of real ferroelectric memory devices. The thesis begins with a look at results of lateral scaling of ferroelectric capacitors from the micron to the submicron range. In the study of lateral size

scaling, the switching properties of lead zirconium titanate ($PbZrTiO_3$) were evaluated. The second half of this dissertation focuses on thickness scaling of the ultra thin films of thicknesses less than 100 nm.

The study on the lateral size effects revealed that there was no change in the switching polarization for the capacitor sizes investigated. However, the intrinsic size effects were observed as the lateral size scaled down from the micron to the submicron range. The study on the thickness scaling showed the suppression of polarization at a critical thickness and an increase of coercive field as the film thickness decreased.

This work was supported by the National Science Foundation - Materials Research Science and Engineering Center (NSF-MRSEC).

PULSE SWITCHING AND SCALING EFFECTS IN FERROELECTRIC CAPACITORS

by

Sanwarit Prasertchoung

Dissertation submitted to the Faculty of the Graduate School of the
University of Maryland, College Park in partial fulfillment
of the requirements for the degree of
Doctor of Philosophy
2006

Advisory Committee:
Professor Ramamoorthy Ramesh, Chair/Advisor
Professor Chi H. Lee
Professor John Melngailis
Professor Alexander Roytburd
Professor Lourdes Salamanca-Riba

DEDICATION

To my beloved parents

Dr. Chamnan and Dr. Nantavan Prasertchoung

ACKNOWLEDGMENTS

Throughout my study in the Ph.D. program at the University of Maryland, I have always felt grateful to have Prof. Ramamoorthy Ramesh as my advisor. There are no words that can describe his kindness and the knowledge that he has given me. I want to thank him for taking me into his research group. The group is one which I considered to be one of the best research groups in the engineering school at the University of Maryland. Being in his group has provided me the best experience that a graduate student can possibly get. Not only did I have an advisor who was very famous worldwide in his field but I also had access to all the tools that I needed to conduct my research at its best. I thank him for all the hardwork that made my research possible. I am also thankful for his generosity in providing all the equipment that I needed. He has given me many opportunities to collaborate with many scientists and researchers from within and outside the university. Without him, I would not have had an opportunity to work with many exciting research projects, and a chance to meet Dr. Jeff Cross and travel to Japan. As I was finishing up this thesis, I had an opportunity to look through hundreds of emails that he wrote to me. These emails always contained valuable advice and suggestions. They remind me of how kind he was. Those messages guided and encouraged me to become successful in my Ph.D. It has been an exciting road. I want to thank him for his patience and for not giving up on me. The experience that I have had working with him always brings back good memories.

I would like to thank Dr. Nagarajan Valanoor (Nagi) for his help, and guidance. I could not have asked for a better mentor and a colleague. Apart from Ramesh, Nagi was always there for me. There has not been one time that he has not helped me. He pushed me to work hard, and made me realize what hardwork is all about. There were many endless evenings and nights that he stayed and worked with me. I want to thank him for supervising my work closely, and for all the attention that he gave me and for energizing and motivating me. His endless passion and appetite for research has set a good example for me to follow. I want to thank him for many valuable discussions, training, and teaching. I will surely miss working with him.

I would like to thank the Materials Research Science and Engineering Center (MRSEC) for funding my education throughout my studies at the University of Maryland. I would like to thank all the MRSEC staff, both past and present. I would like to thank Shirley Winter and Julie Callis for taking care of my purchase orders, and many other administrative tasks. I would like to thank Ellen Williams, MRSEC director, for her advice and support. My special thanks goes to Donna Hammer, MRSEC associate director, for her continuing support, and being extremely kind to me.

I would like to thank past and present staff members in the Department of Materials Science and Engineering. I would like to thank Barret Cole, Annette Mateus, Rachelle Beasley and Kathleen Hart for their help and support. They have been very kind, and treated me very well.

I would like to thank all the professors who taught me, and were involved with my research for giving me of their knowledge, help, and advice.

I would like to thank all the professors in my thesis committee for their guidance and

involvement with my Ph.D. thesis. It is such a privilege to have them in the committee.

I would like to thank all of my colleagues and associates in Ramesh's group; Seung-Yeul Yang, Junling Wang, Ladan Ardabili, Haimei Zheng, Tong Zhao, Zhengkun Ma, Jun Oyang, and Lang Chen for their help with work and collaboration. Special thanks go to Seung-Yeul who had been my colleague for so many years and who helped me with the photo lithography and deposition of top electrodes. I would like to thank Zhengkun for her help with the fabrication of the submicron capacitors by FIB, and providing the SEM images. I would like to thank Haimei for her help with the electrodes deposition, and providing the TEM image in the thickness scaling study. I would like to thank Tong Zhao for providing the thin film samples in the thickness scaling study.

I would like to thank Al Godinez, and Jesse Anderson in the Department of Physics for helping with the purchase orders throughout the years for their friendship, and kindness.

I would like to thank to all the International Education Services (IES) staff for their help and support. My special thanks goes to Jody Heckman-Bose and Nancy Lee Gong whom I have known for a long time.

I would like to thank to all of my colleagues at the Fujitsu Laboratories: Dr. Jeffrey Cross, Dr. Mineharu Tsukada, Yoshimasa Horii, Dr. John Baniecki, Nobuhiro Kin (whom I still keep in touch), Dr. Ei Yano, and the Fujitsu FRAM technology division for their contributions to this study as well as the financial support from the Fujitsu visiting researcher scholarship program (VRSP). This scholarship program helped to get my thesis off the ground. Fujitsu also provided access to advanced equipment and samples. Special thanks go to Dr. Cross and Dr. Tsukada. I would like to thank Dr. Cross for given

me the opportunity do research in Japan and for supervising my research, and putting so much effort in making sure that I had a pleasant stay, and that my research went smoothly. I want to thank Dr. Tsukada for being very kind to me and for his tremendous support in providing me all the tools and equipment; and especially for giving me a ride home after many late evenings. I was very fortunate to have this privilege, and I am always thankful to him.

I would like to thank Dr. Stephan Tiedke, and Mr. Thorsen Schmitz (aixACCT System) for many fruitful discussions on the switching measurements. I would also like to thank Joe Evans (Radiant Technologies) for giving so much knowledge on ferroelectric testing and for lending me his ferroelectric testers for so many months.

I also would like to thank Dr. Jeff Simpson from the Department of Physics for getting started with LaTex, for all his great advice and support, and especially for his time in writing me long emails, and sending me a sample of his thesis. Without him, writing my thesis in LaTex would not have been possible.

I would like to thank Mr. Jim Bitgood of the English Editing for International Graduate Students (EEIGS) program for editing the English in my thesis. His help has been outstanding. I really appreciate his hard work, effort, commitment, and good will in helping me.

I would like to thank Dan Hines for his help in mentoring my Ph.D. defense presentation. I want to thank him for his time, valuable suggestions, and patience for sitting through so many practice sessions with me. He really helped me to get my presentation in order.

I would like to thank my parents for their tremendous support, love, patience and

understanding. I especially want to thank them for the financial support, and encouragement for so many years until I finally got my Ph.D. Without their love, and support, I would not have come this far. I would especially like to thank my father for all his advice about my research and studies, and my mother for encouraging and keeping me in good spirits. I would like to dedicate this thesis solely to them.

I would like to thank my parents for their tremendous support, love, patience and understanding. Thank you very much for the financial support, and encouragement for so many years until I finally got my Ph.D. Without their love, and support, I would have not come this far. I would like to dedicate this thesis solely to them. I also would like to thank my sisters and my aunt for being part of my life. I apologize for being out of touch with them for so many years during my graduate study. I promise that I will make it up to them. Finally, I would like to thank Wilasinee Kiatapiwat for her love, and support. She has made my life complete. Thank you very much for great advice and encouragement. She has given me so much knowledge about the world. Thank you for advising me to eat good food which kept me strong. Thank you so much for being there for me.

TABLE OF CONTENTS

List of Tables x

List of Figures xi

1 Introduction 1
1.1 Ferroelectric materials . . . 1
1.2 Switching properties . . . 5
1.3 Pulse switching polarization . . . 7
1.4 Applications . . . 9
1.5 Overview of thesis . . . 12

2 Experimental 14
2.1 Atomic force microscopy . . . 14
2.2 Electrical measurements . . . 17
2.3 Pulse switching . . . 18
2.3.1 Setup . . . 20
2.3.2 PUND pulse train . . . 21
2.4 Pulse switching and atomic force microscopy combined . . . 24
2.4.1 The Experimental setup . . . 26
2.4.2 Experimental conditions . . . 32
2.4.3 Parasitic capacitance . . . 32
2.4.4 Signal optimization . . . 36
2.4.5 LabVIEW^{TM} programming . . . 41
2.5 Summary . . . 45

3 Lateral scaling 47
3.1 Introduction . . . 47
3.2 Background . . . 47
3.2.1 Polarization reversal . . . 47
3.2.2 Landau-Ginzburg-Devonshire theory . . . 50
3.3 Thin film preparation . . . 53
3.4 Results . . . 54
3.4.1 Hysteresis . . . 54
3.4.2 Pulse switching . . . 56
3.5 Analysis . . . 65
3.5.1 Ishibashi Model . . . 65
3.5.2 Shur model . . . 72
3.5.3 Ishibashi-Merz-Shur model . . . 74
3.5.4 Switching time . . . 79
3.5.5 Activation field . . . 82
3.6 Further Discussions . . . 86
3.7 Summary . . . 89

4 Thickness scaling 94
4.1 Introduction . . . 94
4.2 Background . . . 95
4.2.1 Theoretical studies . . . 95
4.2.2 Experimental studies . . . 97
4.3 Thin films preparation . . . 99
4.4 Results . . . 105
4.4.1 Hysteresis . . . 105
4.4.2 Pulse switching . . . 105
4.5 Analysis . . . 110
4.5.1 Intrinsic model . . . 110
4.5.2 Depolarization model . . . 114
4.5.3 Coercive Fields . . . 121
4.6 Further Discussion . . . 128
4.7 Summary . . . 130

5 Conclusions and Further studies 132

Bibliography 135

LIST OF TABLES

1.1 Design rules of next generation high-density FRAMs. 12

2.1 Properties of cantilevers used in pulse switching measurements. 17
2.2 Capacitance measurements micron size capacitors. 37
2.3 Capacitance estimations of micron size capacitors. 37

3.1 Summary of the switching parameters obtained from the switching transients of 21.5, 7.74, 0.69, and 0.19 μm^2 capacitors taken at 3V. 71
3.2 Theoretical values of $i_m t_m / \triangle P$ of 21.5, 7.74, 0.69, and 0.19 μm^2 capacitors at 3V. 72
3.3 Theoretical values of t_0 and n obtained from the Ishibashi-Merz fraction switching curves of 21.5, 7.74, 0.69, and 0.19 μm^2 capacitors at 3V. . . . 78

4.1 Summary of data for PZT(20/80) used in thickness analysis calculations. . 111

LIST OF FIGURES

1.1 Ferroelectric perovskite structure and polarization hysteresis loop. 2
1.2 Comparison of single- and poly-crystal polarization hysteresis loops. . . . 3
1.3 Phase diagram of ferroelectric materials. 4
1.4 Perovskite structure and tetragonality. 4
1.5 Tetragonality and compositions dependence of PZT. [1] 5
1.6 Steps in switching of ferroelectric domains 6
1.7 Definition of switching time. 8
1.8 Comparison between 2T2C and 1T1C memory cell architectures. 10
1.9 Roadmap showing scaling trend of FRAMs device. 11

2.1 Setup of atomic force microscope components. 15
2.2 Setup of commercial ferroelectric tester and atomic force microscope. . . 19
2.3 Modified Sawyer-Tower circuit used in pulse swtching measurements. . . 21
2.4 PUND pulse train. 22
2.5 Subtraction of P^* by $P^\wedge$ gives $\triangle P$. 23
2.6 Criteria for successful pulse switching measurement and AFM combined. 26
2.7 Setup of pulse switching measurement and atomic force microscope combined. 27
2.8 Detailed setup of pulse switching and AFM combined. 29
2.9 Construction of the load resistor used in pulse switching. 30
2.10 Diagram showing integration of pulse switching and Multimode AFM. . . 30
2.11 Diagram showing preparation of sample holder for pulse switching integrated with Multimode AFM. 31
2.12 Isolated sample stage and its associated components. 31
2.13 The switching transient contains equal contribution of parasitic charges in both switching and non-switching pulses. 33
2.14 Profile of capacitance vs. sample-AFM tip separation obtained from experiments (circles), and calculations (solid line). 34
2.15 Capacitance measurements and estimation as function of capacitor sizes. . 36
2.16 Voltage transients measured from 100 pF and 10 pF linear capacitors. . . 38
2.17 Switching transients dependent on resistors used in the circuit. Voltage signal increases as a function of resistance. 39
2.18 Reflection, noise, and ringing in small signal measurements. 40
2.19 Noise level pick up by Labview data acquisition before and after system improvement. The noise level was reduced to $\pm$ 0.05 mV. 41
2.20 LabVIEW^{TM} pulse switching program for real-time measurements. . . . 42
2.21 LabVIEW^{TM} (SETPUND) pulse switching program for inputting the PUND pulse train. 43
2.22 LabVIEW^{TM} (ANALYZE) pulse switching program for analyzing the pulse measurement data. 43

3.1 Gibbs free energy diagram shows the free energy necessary to switch from a -P_s to a +P_s spontaneous polarization state. [2, 3] 51

3.2 Secondary Electron Microscopy images showing capacitors of different sizes used in the study. 53
3.3 Polarization hysteresis loops of square shape capacitors scaled down from 225 to 9 μm^2. 54
3.4 Polarization hysteresis loops of scaled capacitors (a) as measured, and (b) 40-points averaging with parasitic compensation. 55
3.5 Switching transient of voltage versus time as a function of capacitor areas scaled from 225 to 9 μm^2. 56
3.6 Profile of P and U pulses applied to 0.19 μm^2 capacitor. 57
3.7 Graphical description of the three methods used to identify onset of the transients. The arrows point out the respective onset for each method. . . 58
3.8 Switching (P^*), nonswitching ($P^\wedge$) and the $\triangle P$ transients for a 0.19 μm^2 capacitor. The figure also shows $\triangle P$ with and without curve smoothing. . 59
3.9 $\triangle P$ vs voltage as a function of the data analysis method. 60
3.10 $\triangle P$ vs voltage as a function of lateral capacitor size, obtained by the deflection method. The plot shows that the switchable polarization for 21.5 and 0.19 μm^2 capacitors are comparable. 61
3.11 Switching transients as a function of voltage of (a) 225, (b) 49, (c) 21.5, (d) 7.74, (e) 0.69, and (f) 0.19 μm^2 capacitors. 62
3.12 Switching transients of 0.69 μm^2 capacitor showing excellent symmetry when measuring under positive and negative pulses. 63
3.13 2Pr vs voltage as a function of device size. 63
3.14 $\triangle P$ vs pulse width for all three capacitors measured by applying a pulse of 3 V with a 3 s delay. The plot shows no observable pulse width dependence, within experimental error. 64
3.15 Current density vs. time of 225, 7.74, and 0.19 μm^2 capacitors. The shape of transients becomes narrower with reduction of the RC time constant as capacitor area decreases from micron to submicron range. 65
3.16 Type of domain growth and dimensionality (n) where (a) n=1, (b) n=2, (c) n=3. 66
3.17 Switched volume diagram showing P in volume A but not in volume B. . 67
3.18 Comparison between experimental result and switching model for micron capacitors at 3 V where the dots represent the experimental results, and the lines the switching model. 69
3.19 Comparison between experimental result and switching model for submicron capacitors at 3 V where the dots represent the experimental results, and the lines the switching model. 69
3.20 Current transient in Shur model is divided into segments I and II where the dimensionality of segment I must be greater than segment II by one i.e. we can either have 3D and 2D, or 2D and 1D in I and II. 73
3.21 Comparison between experimental result and Shur's switching model for submicron capacitors. 75
3.22 Normalized polarization, experimental results vs. Ishibashi-Merz model fitting, of 7.74 μm^2 capacitor. 76

3.23 Normalized polarization, experimental results vs. Ishibashi-Merz model fitting, of 0.19 μm^2 capacitor. 76
3.24 Characteristic switching time plotted as a function of capacitor areas obtained from the Ishibashi-Merz model. 79
3.25 Switching time versus fields as a function of capacitor size. 81
3.26 Switching time decreases as a function of capacitor areas indicating that measurements were limited by RC time constant. 82
3.27 Plot of log(i_{max}/A) vs. 1/E (a) as function of capacitor area. 84
3.28 Plot of activation fields as a function of capacitor area from micron to submicron range. 85
3.29 SEM image of submicron capacitor of 0.16 μm^2 as received (a) and with grid count (b). 87
3.30 PFM images of a ferroelectric capacitor showing topography (a), d_{33} amplitude (b), and 180° phases (c). 88

4.1 Variation of the local polarization P(z) in the vicinity of a plane free surface situated at z=0. The bulk polarization is denoted by P_∞ while P_1 denotes the polarization at the surface. λ is the so-called extrapolation length. 96
4.2 Phase diagram of PZT(20/80) epitaxial film grown on dissimilar cubic substrate. The second and first order phase transformations are shown by thin and thick lines. The quadruple point where S_m=0 is the Curie-Weiss temperature (θ). [4] 97
4.3 Model system (Landolt Bornstein Tables). [2] 99
4.4 TEM image of 4 nm film. 100
4.5 $\triangle P$ vs pulse width for 8 nm and 15 nm capacitors measured at constant field. The plot shows pulse width dependence indicating that 2 μs pulse width is the most suitable width to fully switch micron size capacitors without shorting them. 101
4.6 SEM image of the SRO/PZT/SRO structure with the capacitor area of 0.2×0.2 μm^2 of the 80 nm film fabricated by FIB. 102
4.7 Comparison of the switching polarization of the continuous (micron size) and FIB (submicron size) capacitors. 102
4.8 Comparison of switching polarization of 80 nm film with SRO and Pt electrodes. 104
4.9 AFM section analysis images showing a) height profile, b) top view of submicron capacitor. 104
4.10 Polarization hysteresis as a function of thickness. 106
4.11 Voltage density showing suppression of the voltage signal measured from 15 nm, 8 nm, and 4 nm films. The inset shows P^* and $P^\wedge$ responses for the 4 nm thick film. 107
4.12 Switching polarization profile as a function of applied fields of different film thickness. 108
4.13 Switching polarization plotted as a function of film thickness. 109

4.14 Switching transient shows a shorted capacitor of 8 nm thick film indicated by the shift of the base voltage level away from 0 V. 109
4.15 Theoretical fitting of Li's intrinsic model with the experimental data. . . . 113
4.16 Depolarization conditions of thin film showing a) boundary conditions, b) depolarization charges, and c) potential profile across the capacitor and electrodes. [5] 115
4.17 Theoretical fitting for depolarization of a different dielectric constant. . . 117
4.18 Comparison of the order parameter as a function of thickness with the theoretical prediction. 118
4.19 Plot of $\log(T_{c(d)} - T_c/T_c)$ vs. $\log(d)$ showing the transition of ζ as a function of thickness. 120
4.20 Plot of Curie temperature (T_c) as a function of misfit strain (S_m). 120
4.21 Coercive fields are plotted as a function of film thickness. 124
4.22 Comparison of experimental results with theoretical models from Mehta and Kay-Dunn. [5, 6] 125
4.23 Plot of ln(E_c) vs. ln(thickness), where the slope was found to be -0.5. . . 125
4.24 Fitting of the experimental data using Dawber's model and $d^{-1/2}$. Dawber's model does not fit the data at the thicknesses below 15 nm whereas the $d^{-1/2}$ expression shows a perfect fit. 127
4.25 Coercive fields calculations with consideration of depolarization in the cases where $4\pi P_s \gg \epsilon_f E$ and $4\pi P_s \ll \epsilon_f E$. 128
4.26 Tetragonality (c/a) measured as a function of thickness between 4 nm and 50 nm. 129
4.27 Modified depolarization model with intrinsic contribution. 131

5.1 Hysteresis measurements as function of lateral scaling of epitaxial film $PbZrTiO_3$. 134

Chapter 1

Introduction

1.1 Ferroelectric materials

Ferroelectric materials belong to a class of polar crystals in a subset of piezoelectric crystals. They lack a center of symmetry, and exhibit moment per unit volume or *spontaneous polarization* under an applied field. Under stress, they produce a linear strain response called *piezoelectric* effect.[2] Ferroelectric materials have a distorted *perovskite* structure with a general formula ABO_3 where A is a monovalent or divalent metal, and B is a tetravalent or pentavalent metal. A classic example of ferroelectric material is barium titanate ($BaTiO_3$), which can be considered as a predecessor of lead zirconium titanate ($PbZr_xTi_{(1-x)}O_3$ or PZT). In PZT, the Pb^{2+} ions are located at the cube corners, Zr^{4+} /or Ti^{4+} ions at the body center, and O^{2-} ions at the face centers. The switched polarization arises from shifting up/down of Zr^{4+} /Ti^{4+} ions with respect to the position of the O^{2-} ions. The perovskite structure is shown in Fig. 1.1a. A typical relationship between polarization and applied field can be described by the polarization hysteresis loop shown in Fig. 1.1b, where the *remanent polarization* (P_r) is the polarization at zero field, and the *coercive field* (E_c) is the minimum field required to switch polarization between the two opposite states. Under an applied field, the polarization can be switched between the two thermodynamically stable states +P_r and -P_r. This represents the working principle

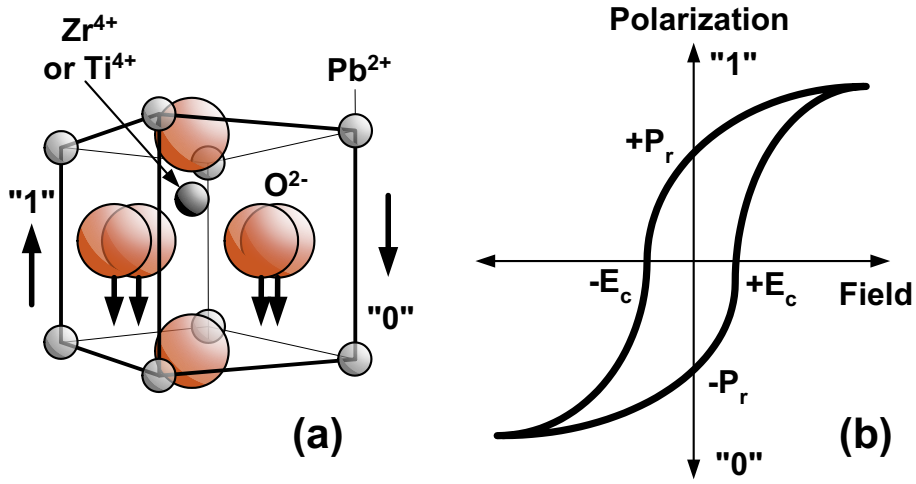

Figure 1.1: a) Structure of PZT showing the shift of Zr^{4+} or Ti^{4+} with respect to O^{2-} representing the logic states of "1" and "0", and b) Hysteresis polarization of ferroelectric materials.

of the binary logic states "1" and "0" used in the *nonvolatile* memory device.[7] The polarization versus field behavior of a single ferroelectric crystal is a superposition of two contributions: i) dielectric ionic and electronic polarization (non-ferroelectric), and ii) spontaneous polarization where the remanent polarization P_r, and the spontaneous polarization P_s are the equal. In a *poly* crystal, P_r is less than P_s because of backswitching induced by space charges or elastic stress. This is shown in Fig. 1.2. Switching polarization is temperature dependent. It decreases as the temperature increases, and disappears at the *Curie* point or the Curie temperature T_c. The change of polarization as a function of temperature is called the *pyroelectric effect*. The Curie temperature can be defined as the temperature at which the transformation from the *paraelectric* to the *ferroelectric* phases takes place. This temperature is associated with a change in differential dielectric response or *permittivity* ε. The relationship between permittivity and temperature is described by the Curie-Weiss law where,

$$\varepsilon = \frac{C}{T - \theta}, \tag{1.1}$$

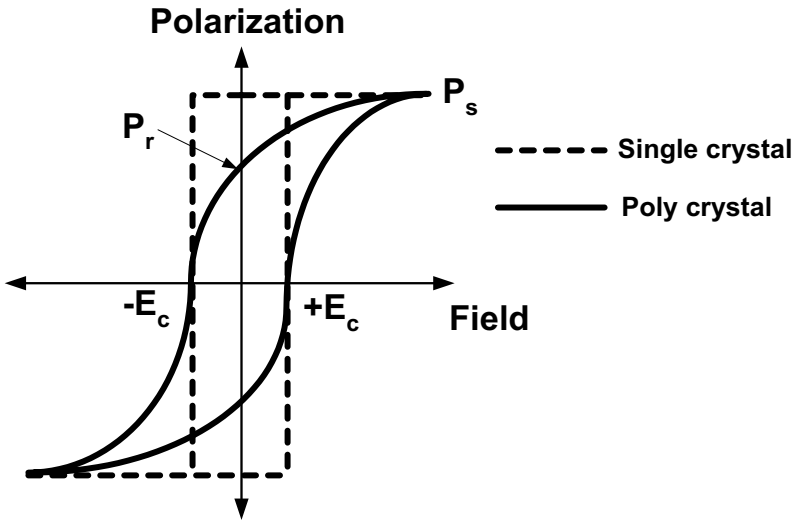

Figure 1.2: Comparison of single- and poly-crystal polarization hysteresis loops.

and θ is the Curie-Weiss temperature, which is equal to the Curie temperature T_c in the case of continuous transition. Often the transition is discontinuous. At below T_c, there are *depolarizing* fields associated with the spontaneous polarization. To minimize these fields, different regions of crystal are polarized in opposite directions. As a result, a volume of uniform polarization called a *ferroelectric domain* is formed. The formation produces a near complete compensation of polarization, and the crystals would exhibit very small or no pyroelectric effects unless they are poled by an external field.[2] Figure 1.3 shows the phase diagram of the Pb-Zr-Ti system. [8] *Tetragonality* describes the degree of distortion of a perovskite unit cell, and can be expressed as

$$Tetragonality = c/a - 1, \tag{1.2}$$

where *a* and *c* are the lattice parameters shown in Fig. 1.4. The degree of tetragonality is affected by the PZT composition. A decrease in zirconium content, and an increase in titanium content results in an increase in the tetragonality. And the higher degree of

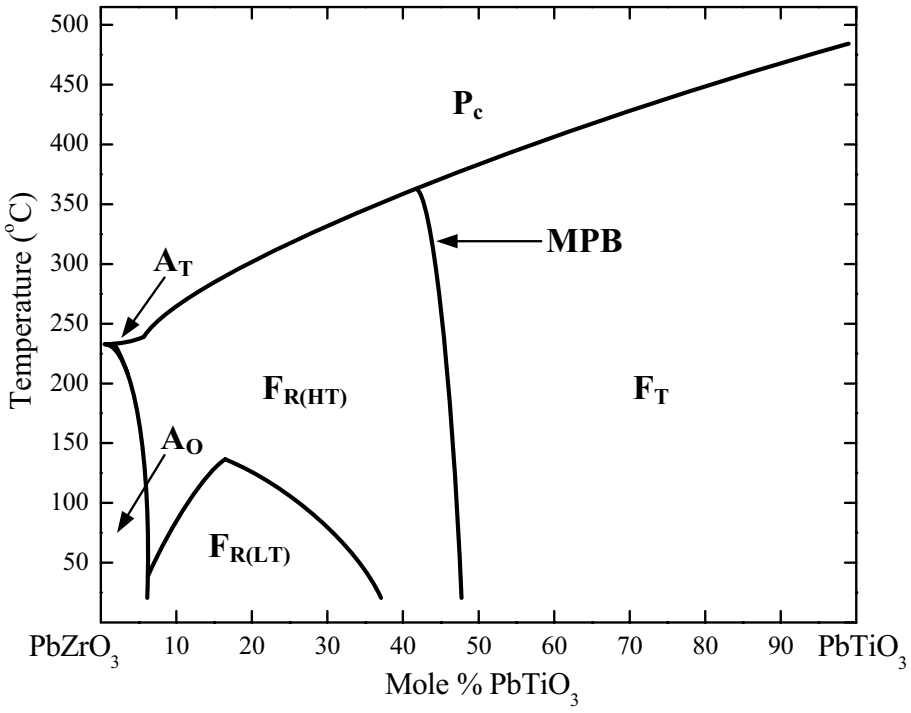

Figure 1.3: Phase diagram shows the transition from *pyroelectrics* to *ferroelectrics*, and the Curie temperature T_c as the transition temperature. [8]

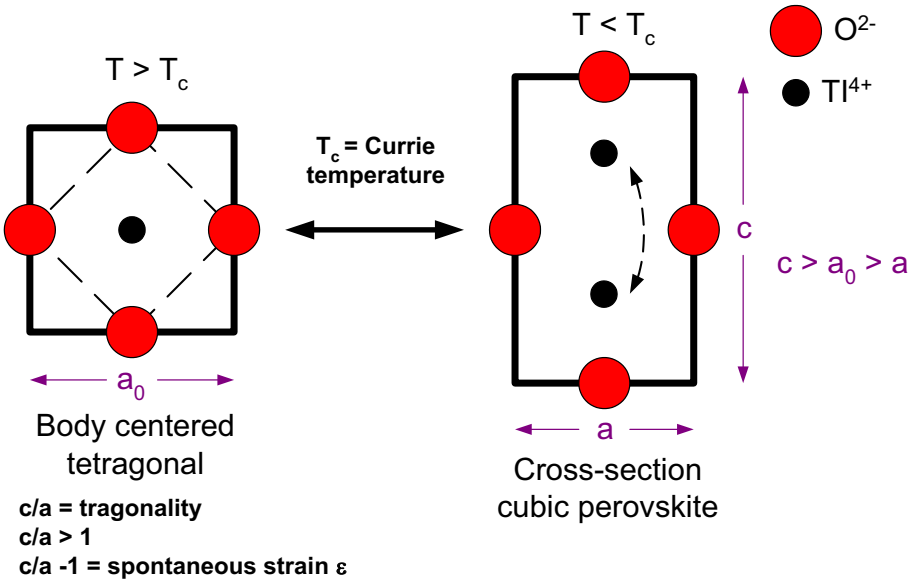

Figure 1.4: Degree of tetragonality and the lattice ratio of “c” and “a”.

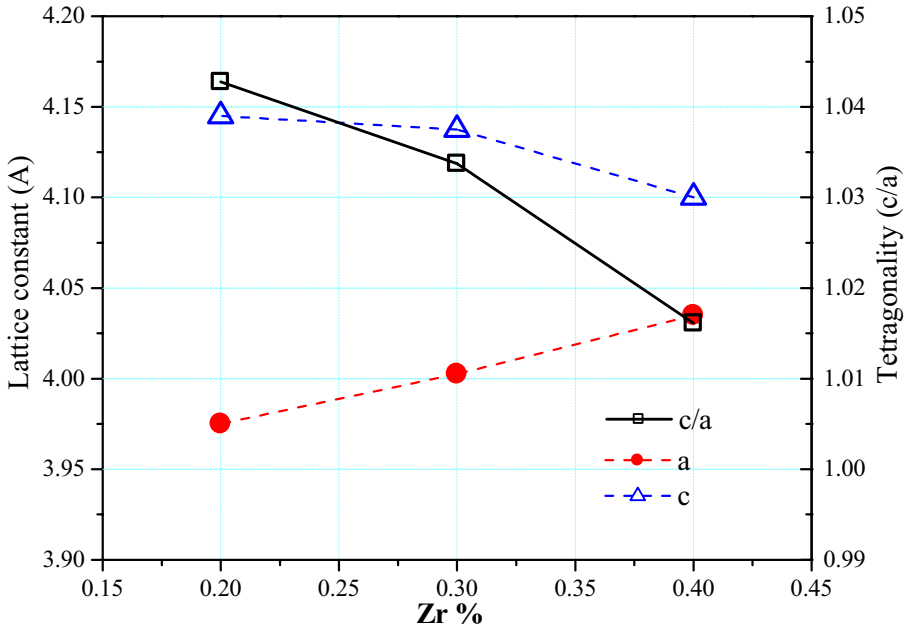

Figure 1.5: Tetragonality and compositions dependence of PZT. [1]

tetragonality or $c/2$ ratio gives higher polarization where *tetragonality* $\propto P^2$. Figure 1.5 shows the plot tetragonality, calculated from (c/a) of different Zr% or PZT compositions.

1.2 Switching properties

Early studies of ferroelectric switching were by Merz in 1954 [7, 9], Stadler, and Miller in the late 1950s [10–12], and Fatuzzo in 1962 [13] The most popular ferroelectric material studied in that period was barium titanate ($BaTiO_3$). Merz observed that by reversing the applied electric field many new domains were created, and $BaTiO_3$ preferred to create many new small domains instead of making an existing polarized domain grow.[7] Merz proposed the two switching mechanisms in the $BaTiO_3$ crystals: i) formation of new domains when the electric field was reversed called nucleation, and ii) growth of small domains called domain wall motion. The later publication by Fatuzzo, however,

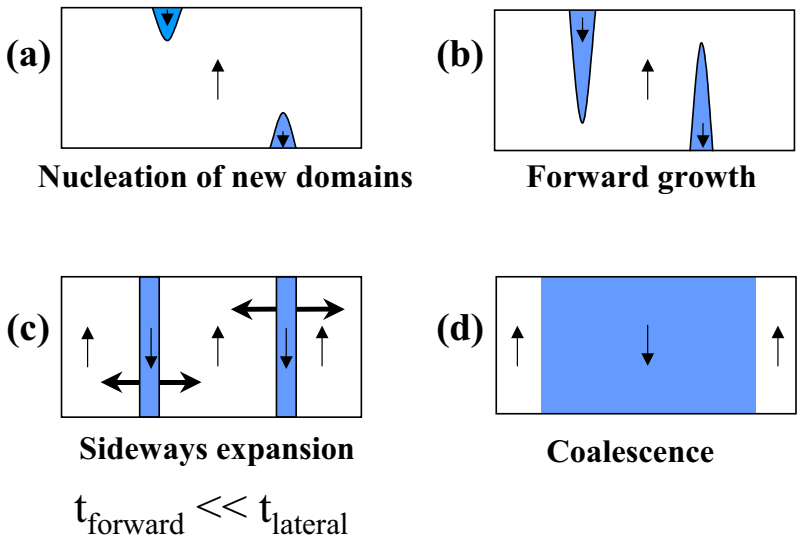

Figure 1.6: Steps in switching of ferroelectric domains.[14]

suggested that switching mechanisms could in fact be broken down into four stages: a) homogeneous nucleation, usually at the anode or cathode; b) forward growth regime; needle-like domains moved at the speed of sound parallel or anti-parallel to the applied field; c) sideways growth in which the needle-like domains spread out laterally; d) coalescence. The rate limiting parameter can be a), b), or c) in different materials. [13] Figure 1.6 shows the stages in the switching of ferroelectric domains.[13] Generally the time for the lateral growth was much slower than the forward growth *i.e.* $t_{forward}$ (1 ns) $<< t_{lateral}$ (20 ns to 1μs). Therefore, the lateral growth was the rate determining step.

In 1971, Ishibashi published the theoretical model which described the switching behavior of ferroelectrics.[15] The model was based on the combination of the classical theories from Kolmogorov and Avrami (also called the K-A theory). [16–18] The Kolmogorov and Avrami theories were based on the study of statistical behavior and the probability of nucleation and growth. The details of these theories will be presented in a later chapter.

Overall, the studies mentioned above lead us to the study of the switching kinetics which is critically important in understanding the switching behavior, and the types of switching processes taking place. As a result, the materials quality, in terms processing and properties, could be evaluated and improved. [19–21]

1.3 Pulse switching polarization

In this study, we will use the pulse switching measurement as a tool in our study to measure the switching property. A typical current vs. time measurement from a ferroelectric capacitor is shown in Fig. 1.7. From the current transient, we can calculate the switching properties such as the switching polarization, and coercive field. The switched polarization from this measurement, compared to polarization hysteresis, is more relevant to the ferroelectric memory since the memory uses square pulses to operate, and it offers a much faster speed. The switching results also allow us to determine other extrinsic and intrinsic properties. From the switching transient, we can extract many switching parameters such as maximum current (i_{max}), time at the maximum current (t_m), and switching time (t_s), all of which are interesting and useful properties. [15] The shape of the switching transient can be modeled, which would allow us to obtain insight into the type of nucleation and growth during the switching process. [21] The switching time t_s for polarization reversal of ferroelectric thin-film capacitors was of direct relevance for such applications and should be as small as possible. The details of the switching properties, and the theories governing them will be discussed in more detail in Chapter 3.

Figure 1.7 shows the switching response, current vs. time, of a ferroelectric ca-

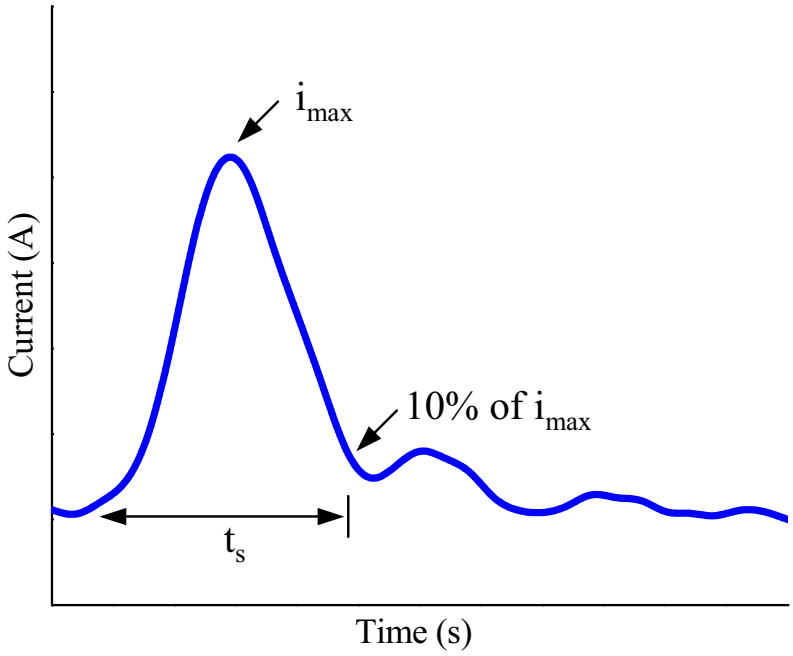

Figure 1.7: Definition of switching where t_s was defined as the time at 10 $\%$ of i_{max}.

pacitor where i_{max} is the maximum current, and t_s is the switching time. The graph can be described by equation 1.3 where t_s is the switching time which is defined as the time required to transfer 90 $\%$ of the charge from one side of the nonlinear capacitor to the other or the time when the switching current i becomes $0.1i_{max}$, and P_s and n were the spontaneous polarization and the dimensionality of the domain growth.[19, 22] From the switching current transient, the polarization can be found by integrating the current as follows:

$$P = \int idt. \tag{1.3}$$

In addition, the activation field which describes the intrinsic switching property can be found from the exponential dependence of the maximum current (i_{max}) or the switching time (t_s) on the applied electric field E. These can be written as

$$i_{max} = i_0 e^{-\alpha/E}, \tag{1.4}$$

and

$$t_s = t_s e^{\alpha/E}. \tag{1.5}$$

The activation field (α) has the same units as the coercive field E_c but its magnitude is much higher (typically, the ratio of α/E_c is of the order of 10 in single crystals as well as in thin films).[20]

1.4 Applications

Ferroelectric materials have a lot of useful properties such as large piezoelectric effect, high dielectric and high pyroelectric coefficients. They can be used for a wide range of applications such as electromechanical sensors, actuators and transducers, dynamic random access memories (DRAMs), and infrared sensors. Apart from these applications, there is a great interest in ferroelectric materials for the next generation nonvolatile high-density memory applications, where the direction of the spontaneous polarization is used to store information digitally. The most basic component of the memory is the capacitor built from a ferroelectric layer sandwiched between top and bottom electrodes, which are connected to the transistors. In ferroelectric random access memories (FRAMs), the memory function is obtained by applying an appropriate voltage across a capacitor to switching the remanent polarization between two polarization directions. The nonvolatile property is due to the ability of the material to hold the polarization state when an external field is removed. FRAMs are attractive for the next generation of high densities nonvolatile memories due to: i) fast writing speed; ii) low power consumption; iii) high endurance; and, iv) compatibility with integrated silicon based semiconductor devices. These proper-

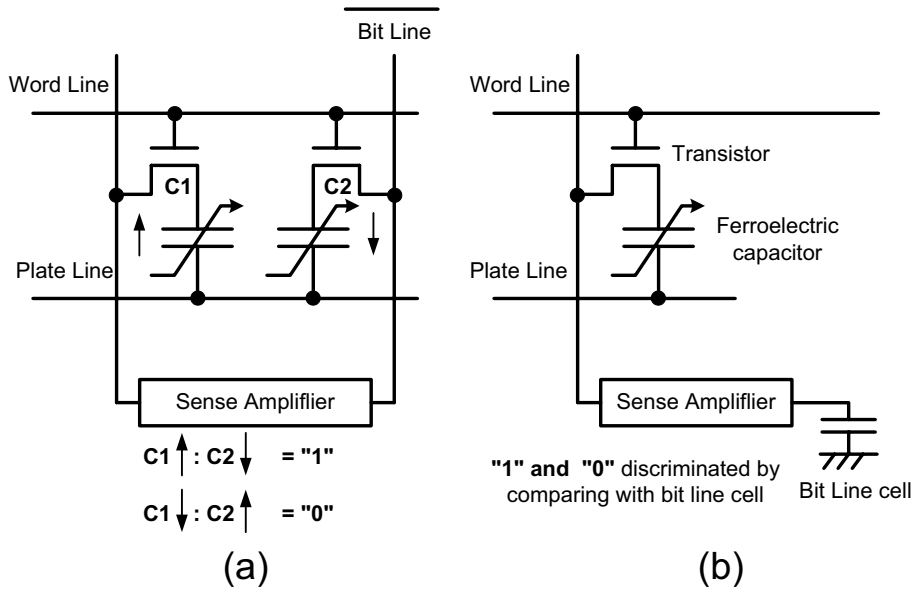

Figure 1.8: Comparison between a) 2T2C and b) 1T1C architectures.[14]

ties make they more superior to any other memory types. FRAMs can be used for a wide range of memory applications such as

- Low-density applications (up to 16kB) for smart ID, memory cards, and contactless TAG.
- Moderate density (up to 256kB) for computer games.
- High density (up to 64MB) for high-end smartcards, networking cards, cellular phones, and audio/video/image/fax/ printing storage.

The FRAM cells of 2T/2C and 1T/1C structures are shown in Fig. 1.8. The 2T/2C was used until the year 2000. Not until recently, the 1T/1C was being used to increase the capacitor density. In the 1T/1C architecture, a memory cell contains one ferroelectric capacitor and one access transistor. The information is stored in the ferroelectric capacitor and the transistor addresses the desired cell. The memory addresses “1” and “0” by

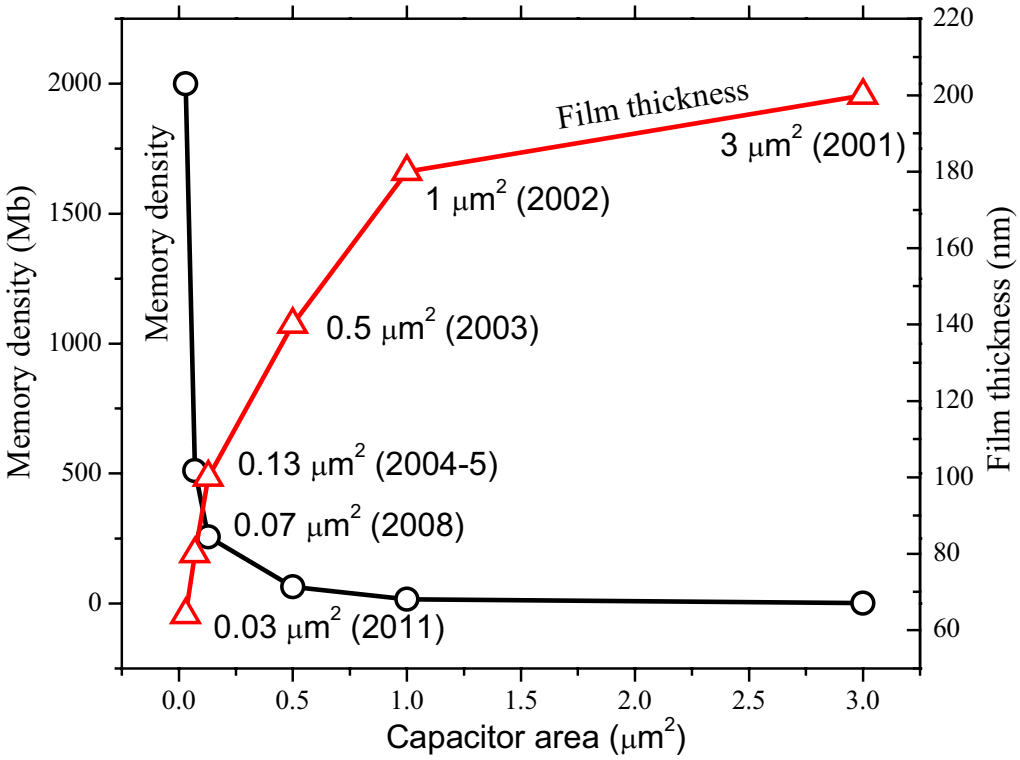

Figure 1.9: Roadmap showing scaling trend of FRAMs device.[23, 24]

comparing the signal output with the bit line (dummy) capacitor. At present, the standard value of of the operating voltage V_{IC} is 3 V but will become 1.8 V for the next generation of submicron high-density memories. Figure 1.9 shows the roadmap of future scaling of the FRAM device. It can been seen that there is a demand to scale the ferroelectric capacitor area to less than 1 μm^2, and the film thickness to less than 100 nm to achieve the next generation 1 Gbit high-density memories. Details regarding the recent and future development are summarized in Table 1.1. With the current trend, the memory density is expected to reach 2000 Mbit (2 Gbit) in the year 2007.[23]

Design rule (μm)	0.5	0.35	0.25	0.18	0.13	0.1
Density (Mb)	1	16	64	256	512	2000
Architecture	2T2C	2T2C/1T1C	1T1C	1T1C	1T/1C	3D1T1C
Capacitor area (μm^2)	3.0	1.0	0.5	0.13	0.07	0.03
PZT thickness (nm)	200	180	140	100	80	65
Operating voltage (V)	5	3.3	2.5	1.8	1.5	1.2
Q_{sw} (μC/cm^2)	30	30	30	35	40	45
Endurance (cycles)	10^{10}/10^{14}	10^{14}	10^{15}	10^{15}	10^{15}	10^{16}
Retention (yr)	10	10	10	10	10	10
Access time (ns)	70	50	30	20	15	10
Switching time (ns)	$<$10	$<$10	$<$10	$<$10	$<$5	$<$5

Table 1.1: Design rules of next generation high-density FRAMs.[23]

1.5 Overview of thesis

The thesis is divided in into two main themes: i) lateral size scaling, and ii) thickness scaling. Chapter 2 introduces the experimental method of pulse switching and atomic force microscopy which can be considered as state-of-the-art measurement for modern electrical characterization of discrete submicron ferroelectric memory devices. Chapter 3 begins with a look at the general switching behavior as the lateral dimensions of capacitors are scaled down from micron to submicron areas. Theoretical issues related to the switching kinetics, and related models are discussed. Chapter 4 concentrates on the thickness scaling where the switch properties of ultra thin films studied with thicknesses from 100 nm to 4 nm (10 unit cells) were studied. This chapter finishes with an investigation of coercive field behavior as a function of thickness, and a discussion of the depolarization

models which played an important role in the thickness effects. Chapter 5 concludes the findings with suggestions of further studies.

Chapter 2

Experimental

2.1 Atomic force microscopy

An atomic force microscope (AFM) is a type of microscope used for imaging a topography. Atomic force microscopy is a non-destructive imaging technique which provides images at nanometer resolution. The microscopes can be operated under ambient conditions, and the samples require no special preparation. This makes AFM one of the favorite microscopy techniques as compared to scanning electron microscope (SEM) and tunneling electron microscope (TEM). Its basic components include a micron-size cantilever with a sharp tip, a laser source, and a photo-detector. The topography image is generated from sensing of the laser beam movements, reflected from a cantilever, through the photo-detector. The movements of the laser beam in the x,y,z directions translate into an image on a computer screen. Apart from the topography, AFM provides useful information such as surface roughness, cross-sectional view, and dimensional analysis. There are three modes of AFM operation; contact mode, tapping mode, and non-contact mode. For electrical measurements, the contact mode is used. Figure 2.1 shows a typical setup of the atomic force microscope. This modern electrical measurements technique utilizes the AFM for making an electrical contact with the nanosize features. Hence, a variety of the electrical signals, such as sine, triangle, and square waves, can be applied to a fer-

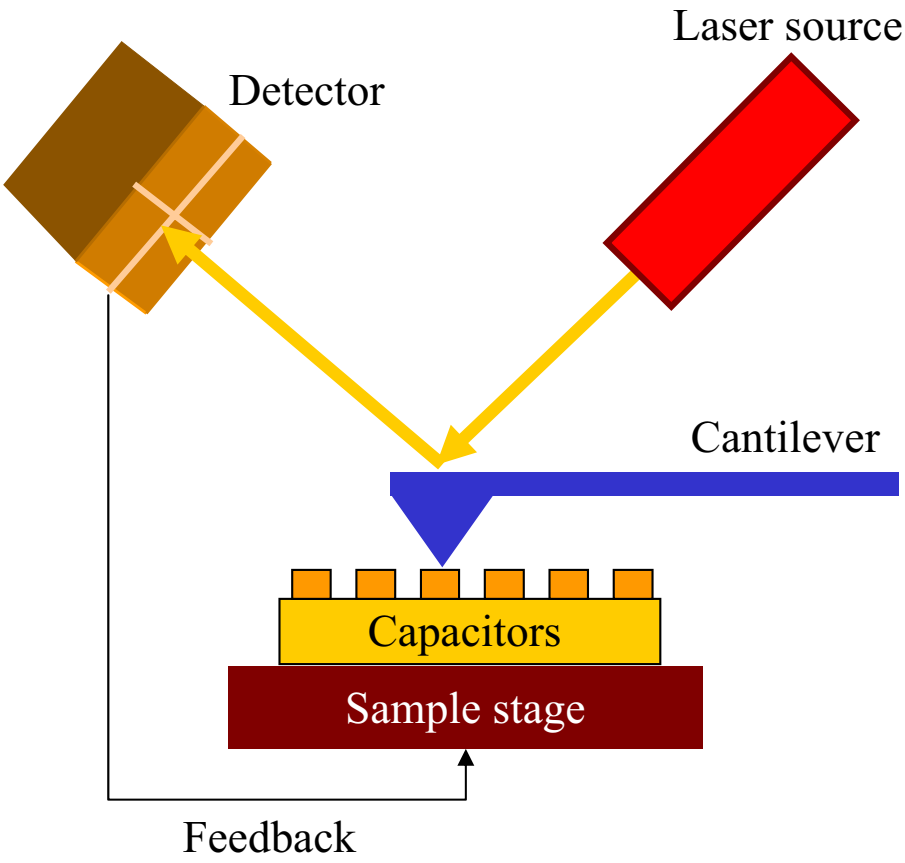

Figure 2.1: Setup of atomic force microscope components.

roelectric device. AFMs have often been used for piezoelectric measurements (d_{33}), and polarization hysteresis (P_r).[25, 26]

As the methodology of AFM has been well documented elsewhere[27], this thesis will concentrate on the key AFM component that is important for the pulse switching studies. The most important AFM component which affects the pulse switching setup is the AFM cantilever. The cantilever properties such as its dimensions, force constant, resonance frequency, and coatings played a crucial role in the measurement sensitivity. In this research, the coating is the most important property. Theoretically, for the contact mode AFM, the ideal cantilever should be short in length to provide a high resonance frequency and small force constant. This makes the cantilever more sensitive to deflection by very small forces to increase the imaging resolution. [27] However, it was found that the measurement resolution was unaffected by size but by the coating. Bigger cantilevers with thicker coating are more robust and have better fatigue resistance.

In the electrical measurements, typical cantilevers used were silicon based with conductive coatings. During the course of this work, a number of the conductive coated tips such as Rh, Au (Seiko Instruments Inc.), Pt-Ir (NanoWorld), W_2C (MikroMasch), Co-Cr, doped diamond (Veeco Instruments Inc.), and carbon nanotubes (University of Wisconsin) were tested. Table 2.1 shows properties of cantilevers used in the pulse switching experiments. The dimensions of the Pt-Ir, and Co-Cr coated cantilevers were 225 μm (l) $\times$ 28 μm (w) $\times$ 3 μm (t). The dimensions of Rh and Au coated cantilevers were not available from the manufacturer but from the comparison through an optical microscope, the sizes of the Rh and Au coated cantilevers were estimated to be about 10 times larger in area than the Pt-Ir, and Co-Cr cantilevers. Among these cantilevers, the Rh coated

Coating materials	Ph	Au	Pt-Ir
Resonance frequency (kHz)	28	28	75
Force constant (N/m)	1.9	1.9	2.8
Coating thickness (nm)	100	100	23
Performance rating	Excellent	Good	Fair

Table 2.1: Properties of cantilevers used in pulse switching measurements.

cantilever showed the best wear resistance and electrical conductivity. In summary, it was found that the cantilevers used in the pulse switching experiments should have i) Rh coating, ii) Thick coating, and iii) Large size.

2.2 Electrical measurements

Although quasistatic hysteresis (60-1000 Hz) and piezoelectric loops for submicron capacitors have been well documented [25, 26, 28] and Tiedke et al. have shown non-averaged hysteresis curves down to 0.09 μm^2 with excellent signal-to-noise (S/N) ratio [29]; there is a critical need to understand the dynamic switching behavior of such nanoscale capacitors.

The standard electrical characterization such as polarization hysteresis, capacitance (C-V), and current (I-V) measurements on the large micron size capacitors with diameters between 30-50 μm were usually carried out using Precision Premier (Radiant Technologies, Inc.) and an electrical probe station. Precision Premier was a commercial ferroelectric tester, with its signal output and input connected to the probe station equipped with two metallic needles, and an optical microscope. In this setup, the probe needles were

used to make the electrical contacts with the capacitor's top and bottom electrodes. The smallest capacitor diameter that could be measured using this setup was 9 μm. Apart from the standard characterizations, many modern electrical characterizations were becoming more common but needed different kinds of tools and experimental techniques. For example, the Precision LC (Radiant Technologies, Inc.), and TF Analyzer 2000 (aixACCT system) were developed for electrical measurements of submicron capacitors [26], while the lock-in techniques were used for piezoelectric measurements. [25, 30]

Polarization hysteresis, which allows a fast characterization of the ferroelectric thin films, was considered a standard technique. In the measurement, a triangle waveform was applied to a ferroelectric capacitor in a Sawyer-Tower circuit. The number of charges was measured across a couple capacitors, and plotted as a function of applied voltage. The polarization hysteresis setup of a commercial TF 2000 Analyzer (aixACCT Systems, Germany) is shown in Fig. 2.2. The C-V and I-V measurements on the submicron capacitors were carried out using the Precision LC (Radiant Technology, Inc.). This testing unit allowed the electrical measurements to be done at the submicron level with accuracy and precision. The LC unit was very portable with programmable software. The purpose of using the LC unit specifically for the C-V and I-V measurements was that the Radiant's equipment has been long established as the standard equipment in laboratories.

2.3 Pulse switching

In the 1950s, Walter J. Merz used pulse switching measurements to study the switching kinetics of ferroelectric material (Barium Titanate) for the first time.[7] The experimental

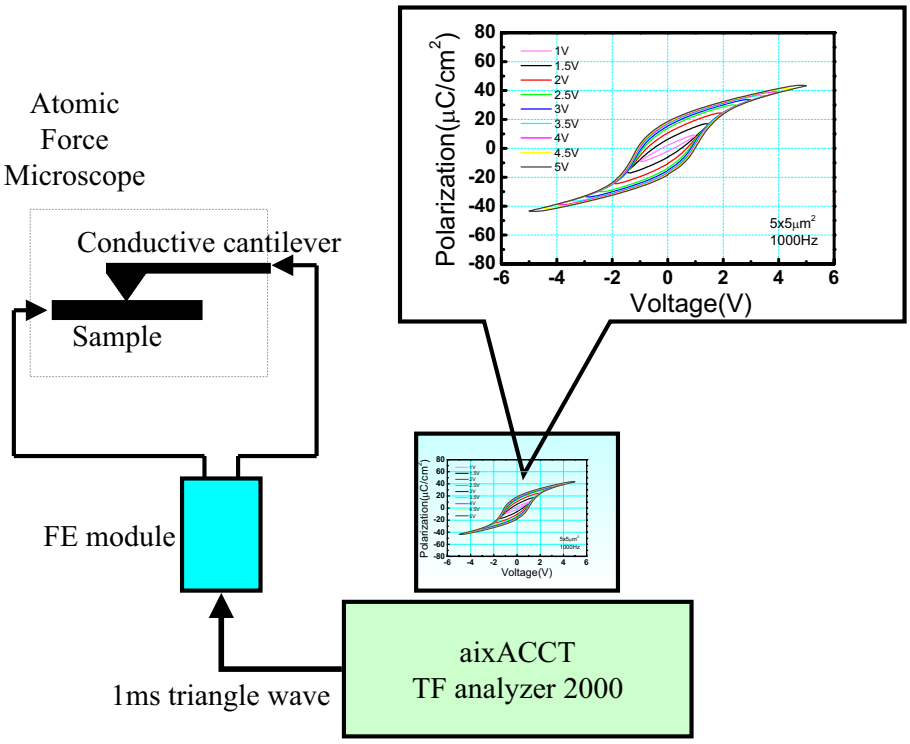

Figure 2.2: Setup of commercial ferroelectric tester and atomic force microscope.

results show the dependency of switching current and switching time on applied electrical fields, temperatures, and sample sizes. In his study, it was found that the maximum current i_{max} obtained from the switching transient can be represented by

$$i_{max} \sim^{-\alpha(T)/E}, \tag{2.1}$$

where $\alpha(T)$ is the activation field which is also temperature dependent, and E is the electric field. In this study, the activation field decreases linearly with temperature. In 1980s, the pulse switching measurements were standardized to solve the problems of different testing practices which could lead to different conclusions. [31] This would allow a direct comparison of test data generated at different facilities. The methodology of pulse switching was carried out as a function of voltage, and the measured switching polarization was obtained from the integration of the voltage transient measured across a capacitor or a

shunt resistor coupled to a ferroelectric capacitor. According to the standardized methodology, five pulse "PUND" type pulse train (- + + - -) should be used, with the minimum sample size of 5 capacitors, and preconditioned with a bipolar waveform. It was also suggested that pulse width below 100 ns was necessary for high speed memory design. [31]

Li's experimental setup had a resolution that detected switching times in the pico second range but lacked the ability to make a direct measurement on submicron capacitors. In Li's experiments, the micron size capacitors measured were connected to the pulse switching setup using a wire bonding. [32]. Larsen commented that a direct measurement is necessary. [33] Tests on series of capacitors connected together yield the average properties but do not explain the failure and deviation of properties of a single capacitor. In his studies, electrical measurements on capacitors down to 0.04 μm^2 were presented. Direct electrical measurements on an array of 800 capacitors (800×800 nm^2 or 300×300 nm^2) connected in parallel shows good but average results.

2.3.1 Setup

The electrical circuit used in the pulse switching measurement was a modified Sawyer-Tower circuit where a reference capacitor was replaced with a resistor. The resistor used in this method is called the "Shunt" resistor. Figure 2.3 shows the modified Sawyer-Tower circuit. [34] The transient current i_{FE}(t) of the ferroelectric capacitor C_{FE} during switching was determined by measuring the transient voltage $V(t)$ developed over the Shunt resistor R. By applying a pulse of sufficient amplitude and width to produce polarization reversals and measuring $V(t)$, both the switched charge $\triangle P$ (polarization times area) and the switching time t_s could be determined from the integration of $V(t)/R(i_{FE})$ over its

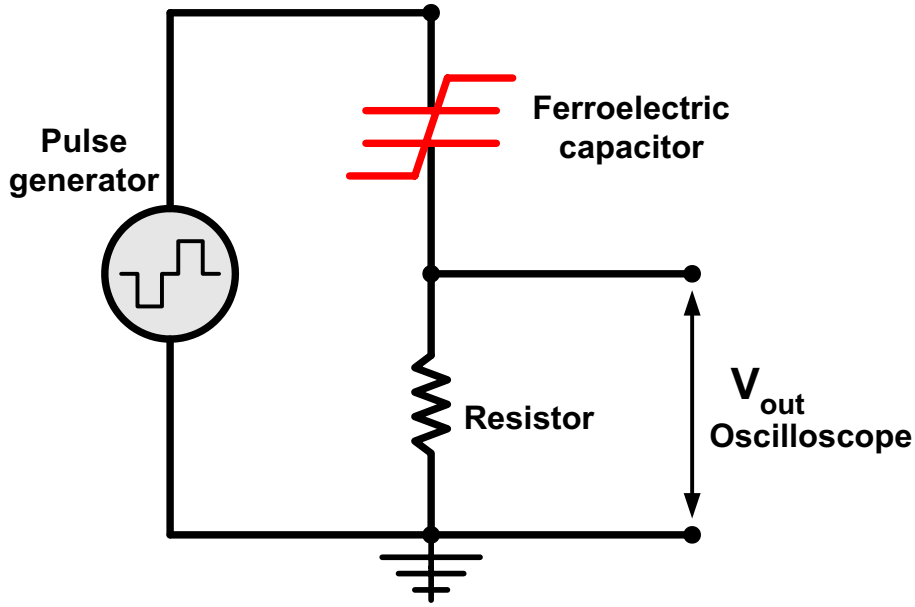

Figure 2.3: Modified Sawyer-Tower circuit used in pulse switching measurements.

transient.

2.3.2 PUND pulse train

The pulses used to measure the positive (+$\triangle P$) and negative (-$\triangle P$) switching charges were configured as a pulse sequence called a "PUND" pulse train [1] shown in Fig. 2.4. The pulse train consisted of five pulses: negative, positive, positive, negative, and negative separated by a period called "delay time". In the experiment, the preset negative pulse was applied to arrange the ferroelectric domains in the same initial polarity state before being switched. Then, the first positive pulse (pulse P) was applied to switch the capacitor to the opposite polarity (positive). The charges measured from this pulse P^* contained the contribution of the switching ($\triangle P$) and the non-switching ($P^\wedge$) components. To separate the two components, the second positive (pulse U) was applied where

[1] The term PUND stands for Positive Up Negative Down.

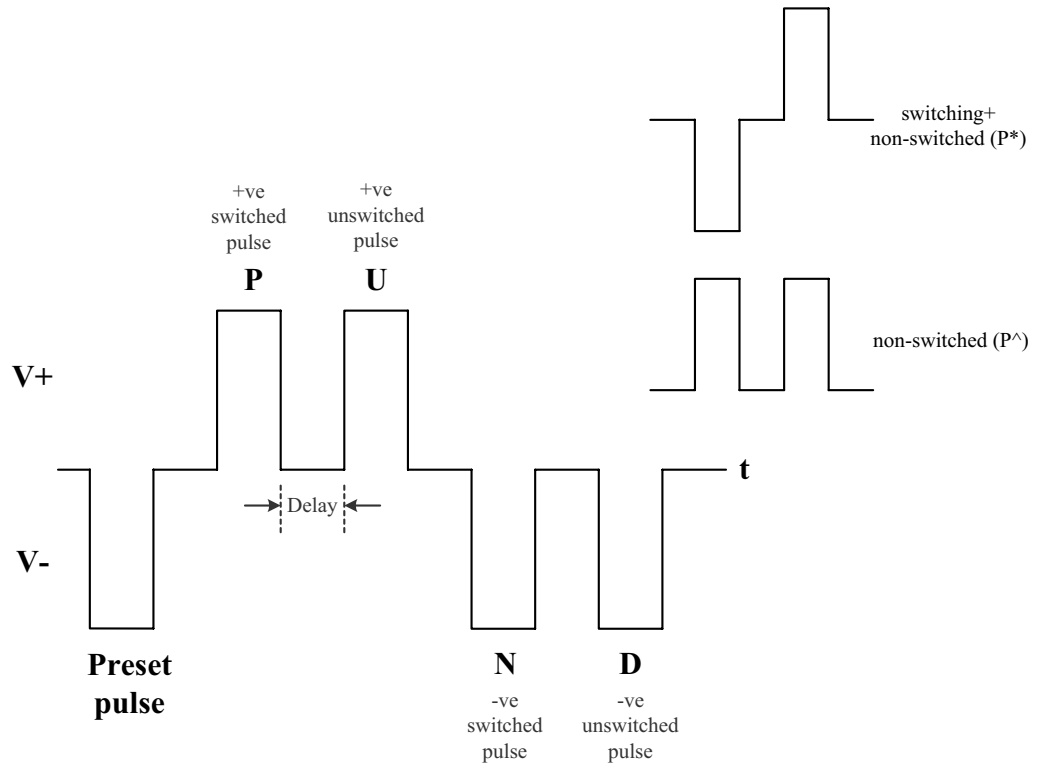

Figure 2.4: PUND pulse train.

it would measure only the non-switching ($P^{\wedge}$) component as the ferroelectric domains were no longer switched. Thus, the subtracting the charge of pulse U from the charge of pulse P would give the switching polarization ($\triangle P$) corresponded to the switching of the ferroelectric domains, and can be expressed as

$$\triangle P = P^{*} - P^{\wedge}, \tag{2.2}$$

Figure 2.5 shows the subtraction of the transient responses of P^{*} and $P^{\wedge}$ giving $\triangle P$. The switching polarization ($\triangle P$) was defined by the integral of the difference between the switching current and non-switching current. Here, A was the top electrode area of the capacitor.

$$\triangle P = \frac{1}{A}\int (i_{P^{*}} - i_{P^{\wedge}})dt, \tag{2.3}$$

The experiment was repeated in the negative polarity by applying two negative

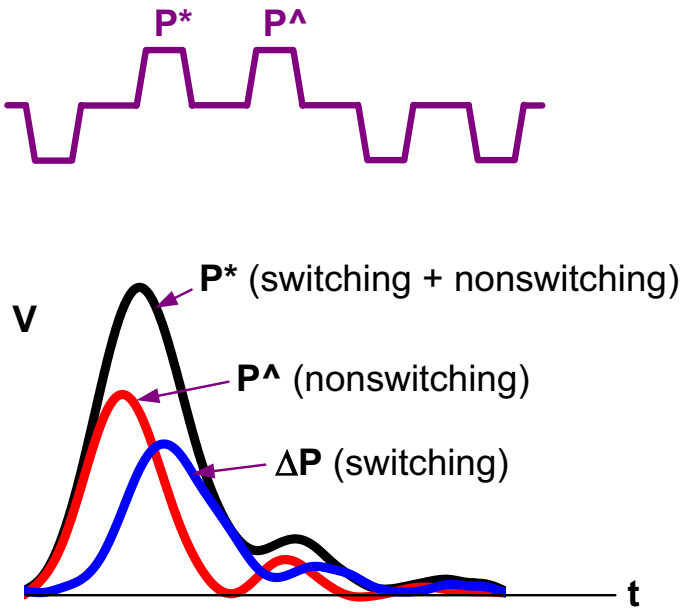

Figure 2.5: Subtraction of P^* by $P^\wedge$ gives switching polarization $\triangle P$.

pulses. These two pulses were necessary because the switching properties in both positive and negative polarities were not always the same. As shown by Abe *et al.* a ferroelectric capacitor could possess asymmetry due to asymmetry of top and bottom electrodes or the discrepancy in coercive voltage between polarities.[35]. The switching polarization ($\triangle P$) was usually quoted as the average value obtained of positive and negative pulses

$$\triangle P = [(P - U) + (N - D)]/2, \tag{2.4}$$

It should be noted that $\triangle P$ is sometimes referred as "Q_{sw}" (Q switched). This term was popularly used in the industry when referring to the switching charges of the FRAM devices. The PUND measurement can be combined with single bipolar pulse sequences to switch the ferroelectric capacitor over extended pulse cycle ranges, *e.g.* from 10^3 up to $10^{10} - 10^{13}$ cycles, to test the fatigue properties. From the nonvolatile memory point of view, the pulse switching measurement method is most relevant for characterizing the ferroelectric properties since the memory write and read processes, and their speed are

governed by the applied voltage pulses. In this method one measures $\triangle P$, which is the difference between the switched P^* and nonswitched $P^\wedge$ responses. [31, 33, 36–38]

2.4 Pulse switching and atomic force microscopy combined

The electrical characterization of ferroelectric thin films is usually performed under conditions not close to the real device operating conditions. For example, the actual real device size is expected to be in the range of 1 μm or less with an excitation frequency of several MHz, whereas a typical measurement is usually performed on 200 μm^2 at kHz or lower frequencies. However, it should be noted that the polarization hysteresis test was not the most suitable test for the memory applications because: i) Polarization hysteresis measurement uses triangle pulses whereas ferroelectric memory uses square pulses for read and write functions. ii) Polarization hysteresis is measured at kHz frequencies whereas ferroelectric memory operates at hundreds of MHz. Since the pulse switching measurement uses square pulses, it could be considered as the most relevant testing method for the memory applications. However, the existing pulse switching tests needed improvement because:

- Most pulse switching measurements were carried out using microsecond pulses whereas ferroelectric memory operates using nanosecond pulses. For example, the write speed of FRAMs is 70 ns.[23].

- If nanosecond pulses were used, the measurements were carried on either micron size capacitors, or an array of submicron capacitors connected together.[38] No measurements using nanosecond pulses have ever been performed on a single sub-

micron capacitor.

Fujisawa *et al.* used AFM and pulse switching combined, but did it on micron size capacitors using microsecond pulse widths.[39] The experimental setup for polarization hysteresis was a lot simpler than pulse switching. This is because there are commercial ferroelectric testers available which provide the test circuit, and computer programs to calculate and plot the polarization hysteresis. Even though the hysteresis measurement was a simpler one, it gives much useful information on the switching properties such as remanent polarization, and coercive field. Furthermore, the shape and position of the loop could give qualitative information on current leakage, and fatigue properties.

In this research, attempts at combining the commercial equipment with an AFM to perform the pulse switching measurements on a discrete ferroelectric submicron capacitors were unsuccessful. Therefore, it was necessary to construct a pulse measurement setup combined with AFM to carry out the studies.

Atomic force microscopy (AFM) can be considered as the elegant tool for electrical measurements of ferroelectric devices. It is now widely used for characterizing the size effects in ferroelectric materials. [26, 30, 39–41] The objectives of the experimental setup in this research were to fulfill the following criteria:

1. Measure discrete submicron capacitors: The setup must be able to measure the switching polarization $\triangle P$ of a discrete submicron capacitor via AFM and pulse switching setup.

2. Automated and programmable: A computer program which could be written to control the equipment, and to acquire the data, where a number of experiments

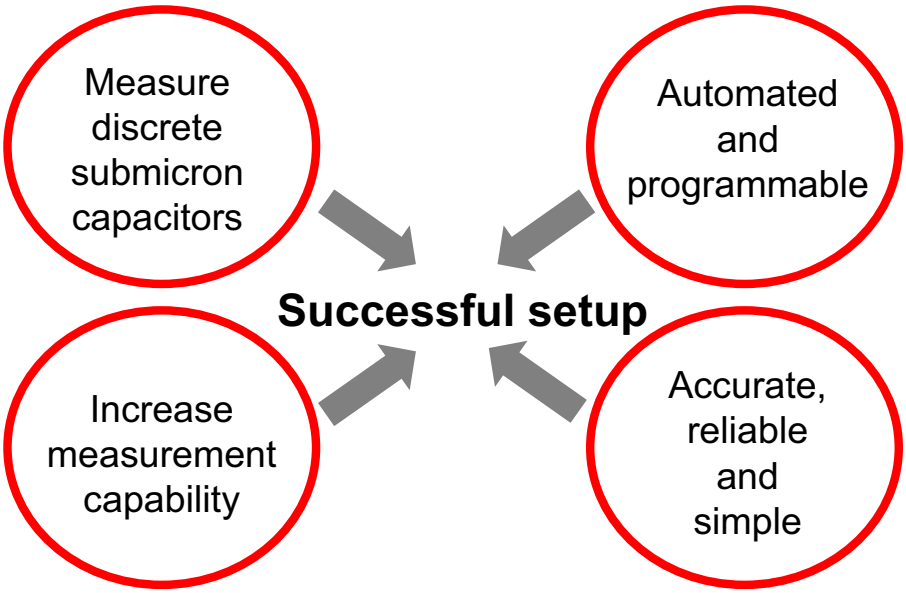

Figure 2.6: Criteria for successful pulse switching measurement and AFM combined.

could be repeated automatically, and the experimental conditions could be input through the computer.

3. Increase measurement capability: The measurement capability must be increased to measure smaller and smaller submicron capacitors until it is instrumentally limited.

4. Accurate, reliable, and simple: The equipment setup, and the computer software must give accurate, and reliable results. The equipment must also be reliable when operating, and the computer software interface must be simple, and easy to use.

These are illustrated in Fig. 2.6.

2.4.1 The Experimental setup

The setup of the pulse switching measurement and AFM combined is shown in Fig. 2.7, and the key components are listed below:

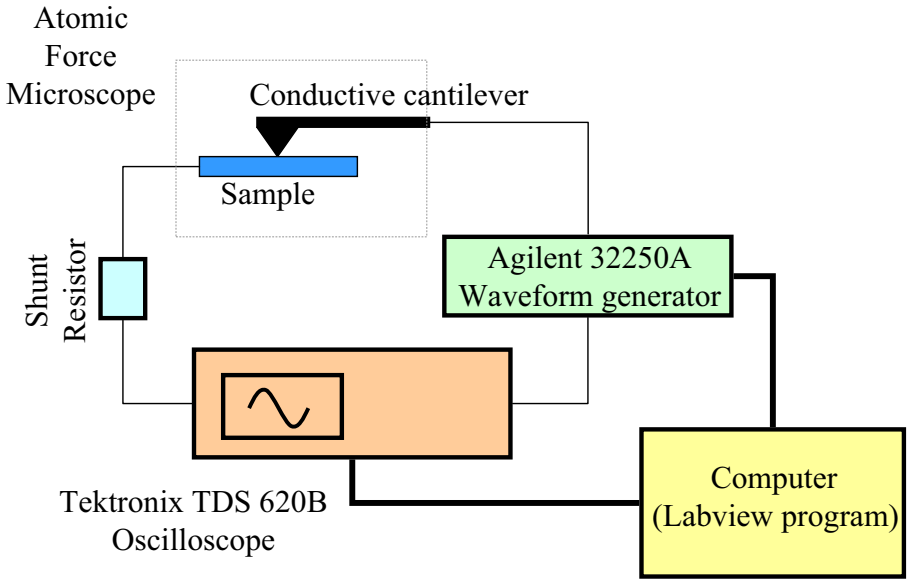

Figure 2.7: Setup of pulse switching measurement and atomic force microscope combined.

1. Atomic force microscope (Digital Instruments Nanoscope IV, D3000).

2. Rh-coated 100-nm-thick silicon based conductive cantilever.

3. Waveform generator (Agilent 32250A).

4. Oscilloscope (Tektronix^{TM} 620B).

5. Active probes (Tektronix^{TM} P6245).

6. Resistor.

7. RF cables.

8. Isolated Au wire.

The measurement setup for pulsed probing was based on a combination of a pulse generator, an AFM, a shunt resistor and a digital sampling oscilloscope, which was used to measure the switchable polarization of a submicron capacitor. The input parameters

such as pulse sequence, width, delay, and amplitude were adjustable and could be used to mimic the operating conditions for the actual FRAMs capacitors, such as 3V voltage pulses of 10-50 ns with similar delay times between the pulses. The circuit layout for the pulse measurement was the same as the modified Sawyer-Tower circuit except that a commercial atomic force microscope (Digital Instruments Nanoscope IV, D3000) equipped with an Rh-coated 100-nm-thick silicon based conductive cantilever was used to make electrical contact with the capacitor. The thicker Rh layer helped to prevent the vaporization of the coating due the high current density, and thus it prolonged the good electrical conductivity of the tip. A waveform generator (Agilent 32250A) was used to generate pulses, in conjunction with an oscilloscope (Tektronix 620B) that was used to record the switching responses, and a LabVIEW^{TM} program was used to run the experiments, and to acquire the experimental data. Figures 2.8 and 2.9 show the detailed setup of the pulse switching and AFM combined, and the construction of the load resistor.

The pulse switching setup can also be integrated with the Multimode AFM. The advantages of the Multimode were: i) the sample's stage could be heated up to $\sim 250\ ^{\circ}$C, ii) it could be used with a gas cell to test a sample under different gaseous conditions. The disadvantage was that the sample stage was relatively small with the maximum diameter of 15 mm. Figure 2.10 shows the pulse switching setup with the Multimode AFM, Fig. 2.11 shows the preparation of the sample holder for the Multimode AFM and the pulse switching setup, and Fig. 2.12 shows a photograph of the isolated sample stage and its associated components.

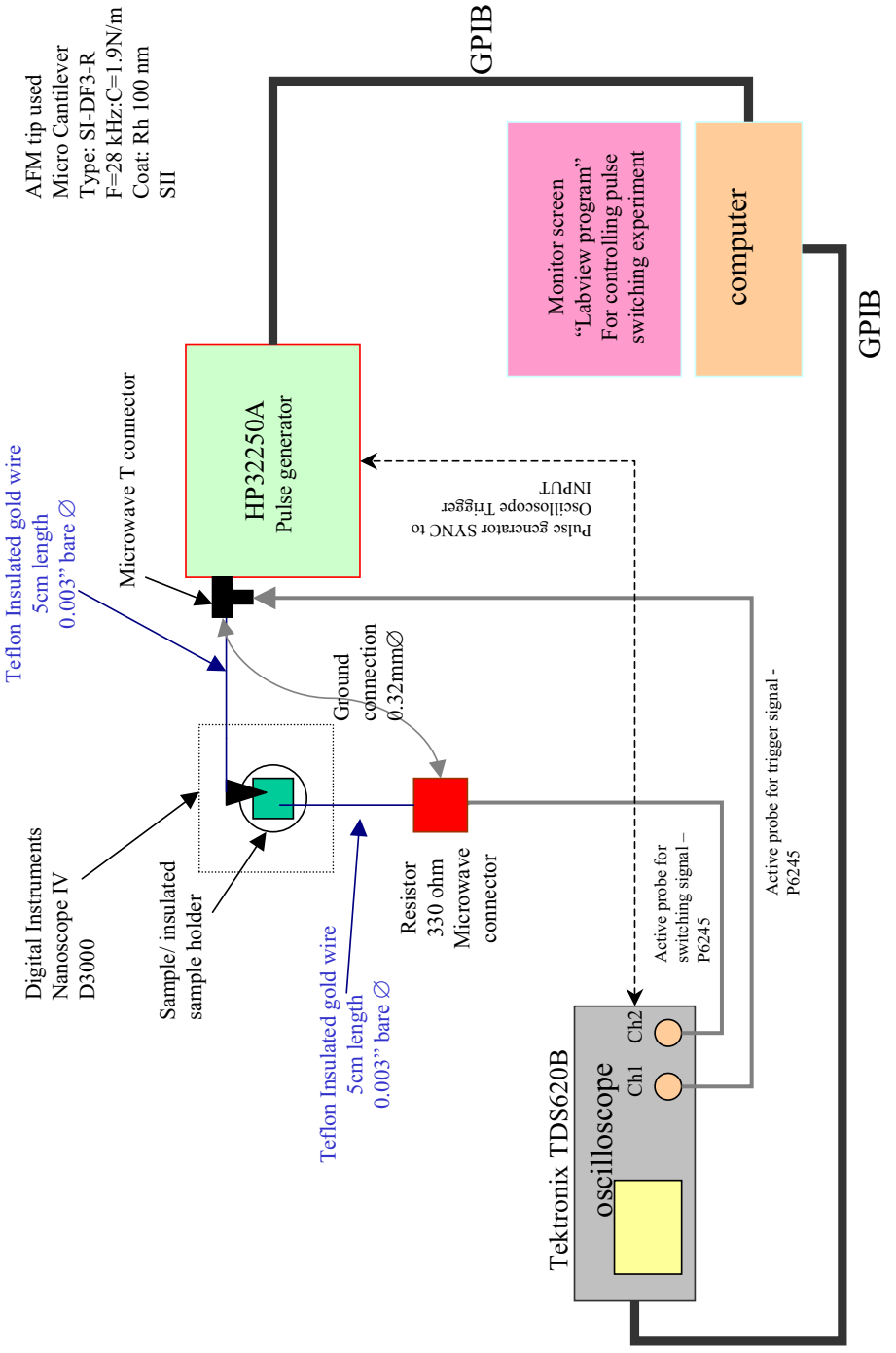

Figure 2.8: Detailed setup of pulse switching and AFM combined.

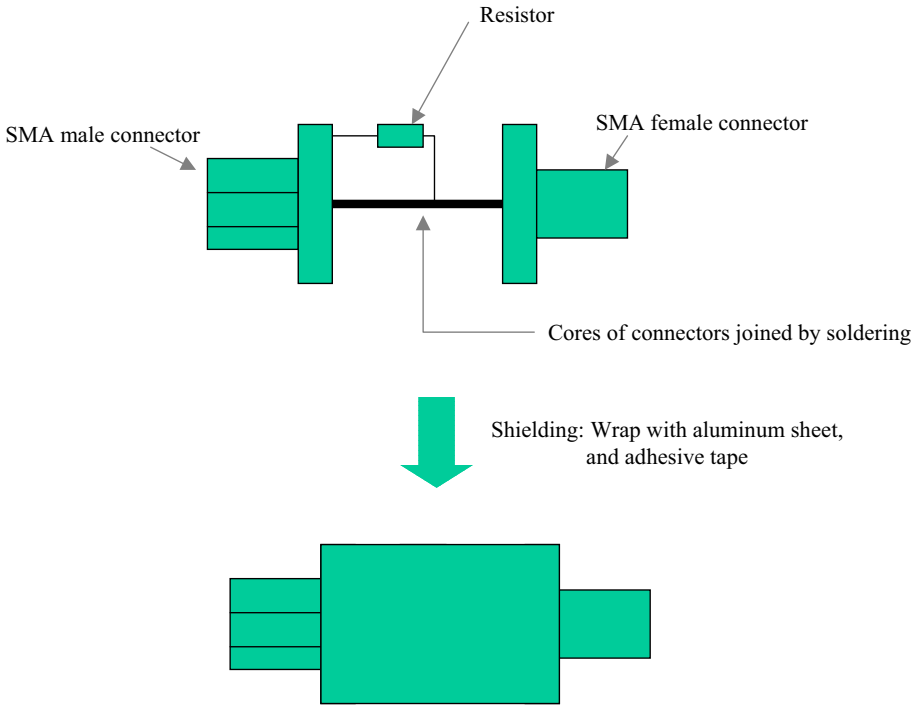

Figure 2.9: Construction of the load resistor used in pulse switching.

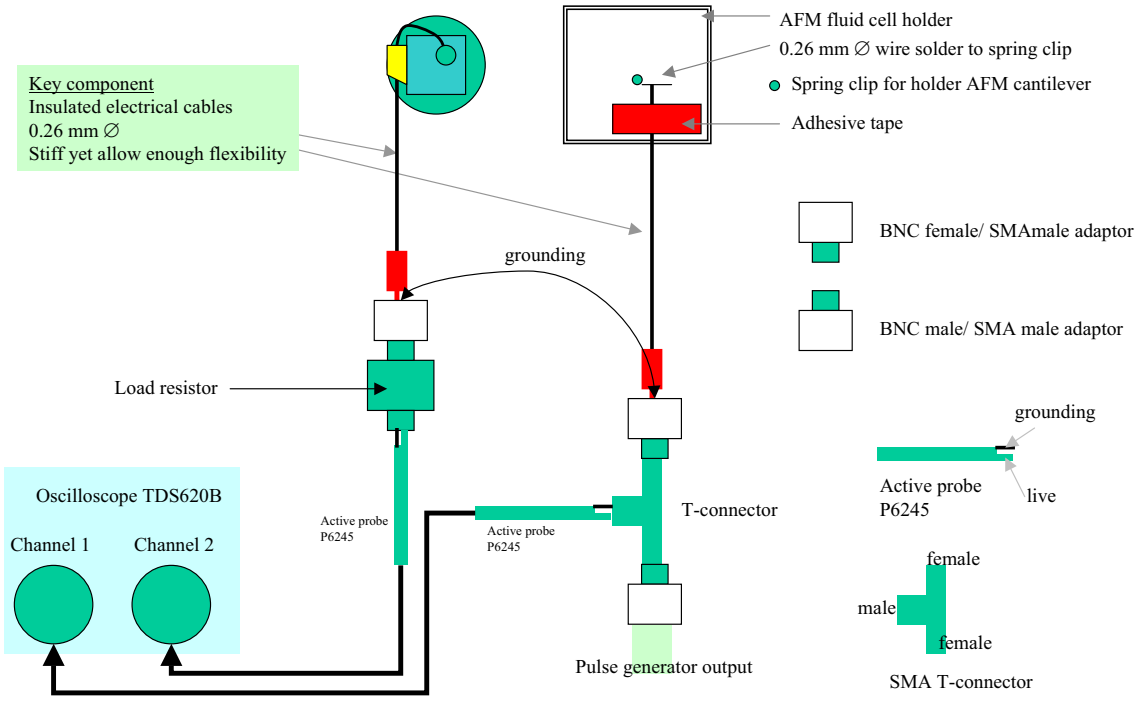

Figure 2.10: Diagram showing integration of pulse switching and Multimode AFM.

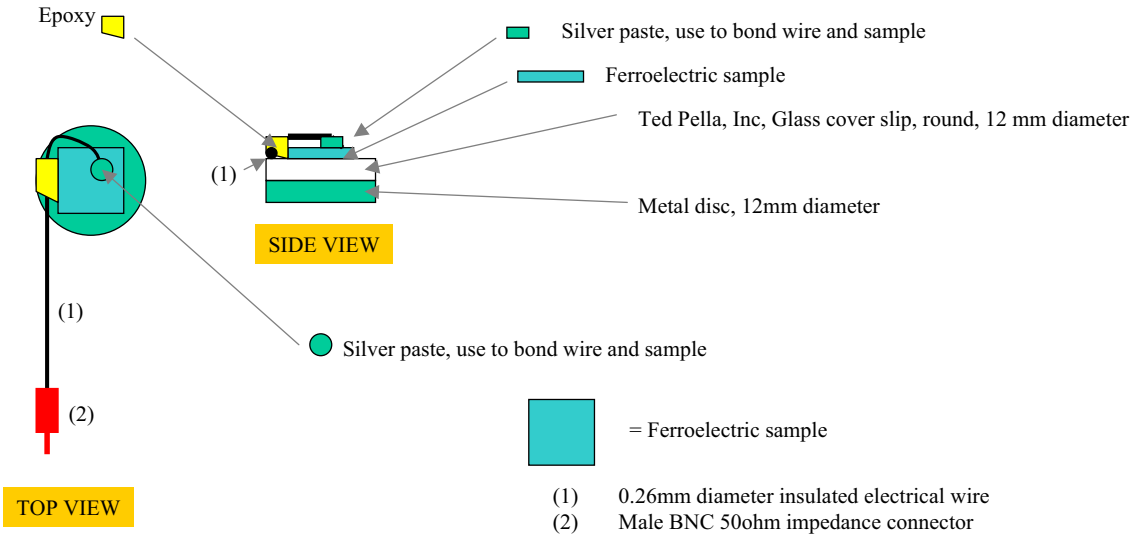

Figure 2.11: Diagram showing preparation of sample holder for pulse switching integrated with Multimode AFM.

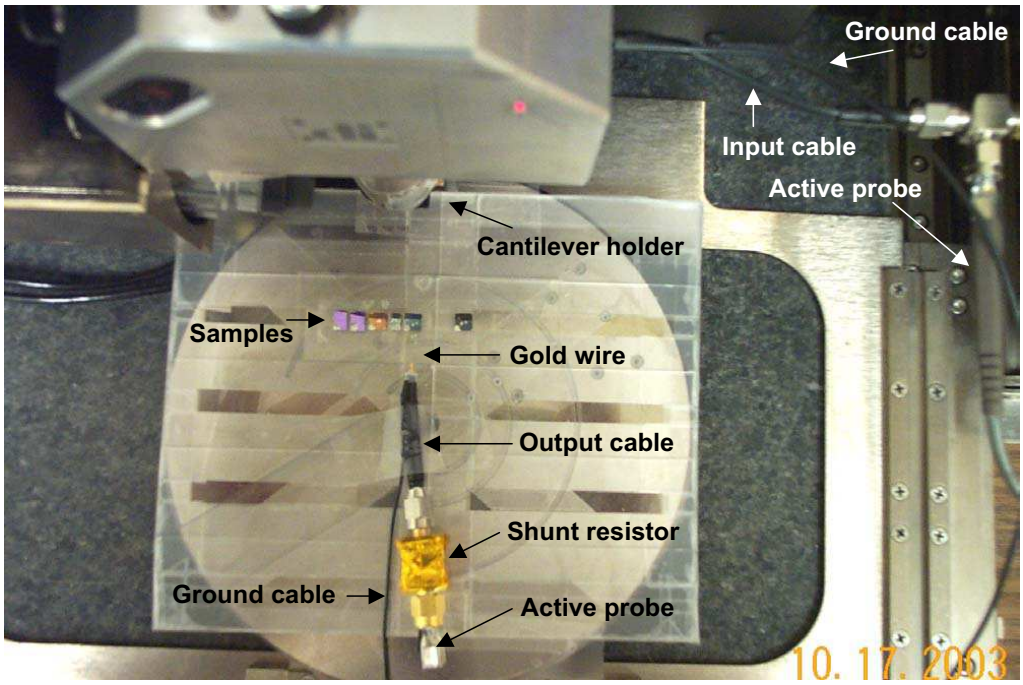

Figure 2.12: Isolated sample stage and its associated components.

2.4.2 Experimental conditions

To take the measurement, the PUND sequence of pulses was applied to a ferroelectric capacitor to obtain the switching transients corresponding to P, U, N, and D pulses. [31] Before a PUND pulse train was applied, the capacitor was trained by applying bipolar pulses of 3 V (200 ns width and delay) for 60 s to obtain a saturated $\triangle P$ value. It should be noted that for the study of switching dynamics, such as the switching speed, a rise time less than 1ns is desirable. [33] However such conditions cause ringing in the switching signal, thereby distorting it. Therefore, in my measurements, the optimum conditions were 8 ns rise time (10%-90%), sensed through a 330 Ω load resistor. These conditions minimized the ringing effect, and provided sufficient signal strength of 16 mV for the submicron capacitors. The maximum noise level in the measurement was $\pm$0.05 mV_{pk-pk}.

2.4.3 Parasitic capacitance

Parasitic capacitance can be described as unwanted capacitance in the measurement circuit. This capacitance arises from the components such as the electrical cables (transmission lines), equipment parts, and the AFM cantilever. In the polarization hysteresis measurement, a parasitic compensation procedure was necessary to extract the polarization of the capacitor material from the parasitic influence of the measurement setup. [26] On the other hand, in the pulse switching measurement, parasitic compensation was not needed. Figure 2.13 illustrates that the switching (P^*) and the non-switching ($P^\wedge$) responses contained the same parasitic contributions of "b" and "c". Hence, when subtracting P^* and $P^\wedge$ to calculate the switching polarization ($\triangle P$), the parasitic influence of "b" and "c"

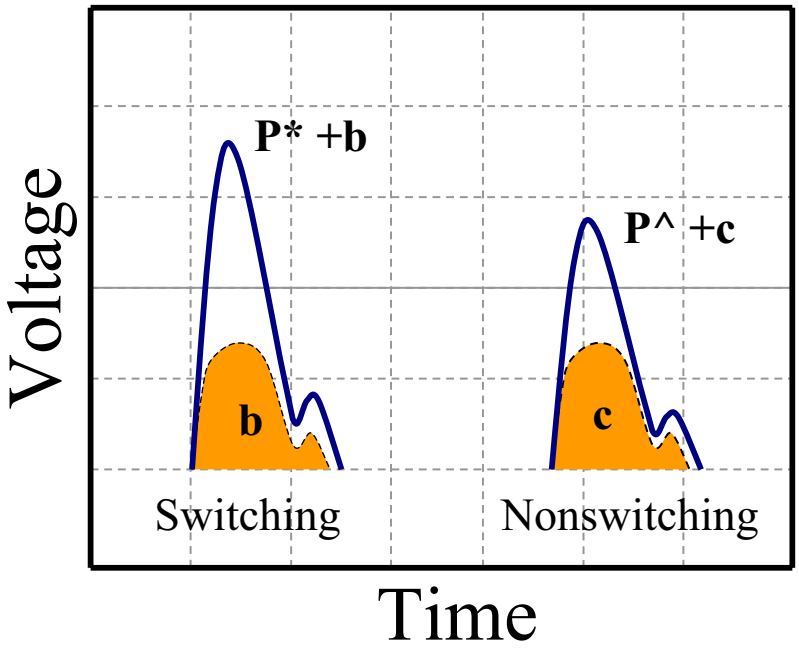

Figure 2.13: The switching transient contains equal contribution of parasitic charges in both switching and non-switching pulses.

would canceled each other out. This could be considered as one of the advantages in doing the pulse switching measurement where the parasitic compensation procedure was not necessary. However, it should be noted that the parasitic component still remained a big problem in small signal measurements and had to be minimized by reducing the length of the transmission cables. If the magnitude of the switching transient was smaller than the parasitic transient, it would not be possible to extract the switching polarization.

Prume et al. developed a finite element model of an AFM cantilever to calculate its parasitic capacitance. This model enables us to calculate the parasitic capacitance, which has to be subtracted from the measurement data dependent on geometric parameters of the cantilever and parameters defined by the measurement setup, e.g. the distance from the wafer in the lifted position. The compensation procedure was carried out on a sample capacitor with an electrode area of 0.09 μm^2.[28] It could be seen from published mea-

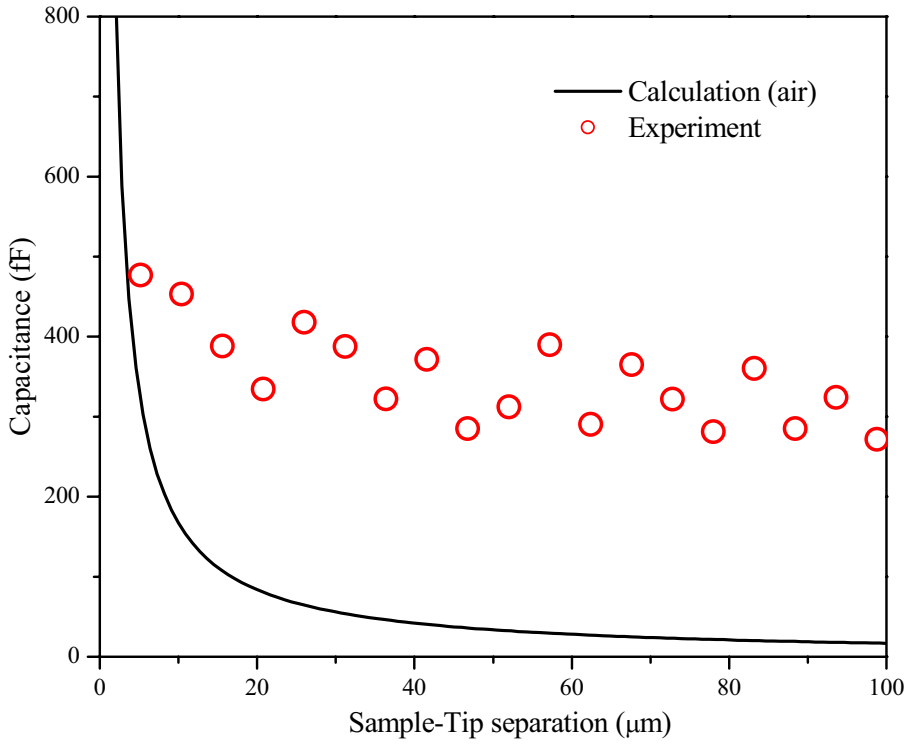

Figure 2.14: Profile of capacitance vs. sample-AFM tip separation obtained from experiments (circles), and calculations (solid line).

surements that it is not sufficient to perform an open measurement with a lifted cantilever and subtract this measurement from the recorded data to obtain the material characteristics. Lifting the cantilever results in a decrease of parasitic capacitance, which cannot be neglected. In my study, it was also found that the parasitic component changes with the cantilever lift height from the top electrode. Figure 2.14 shows the decrease of capacitance as a function of tip separation. In the study by Larsen, a bonding pad was used as a common electrode connecting capacitors but this leads to parasitic capacitance. Evans and Tiedke indicated that the largest source of the parasitic capacitance comes from the AFM cantilever, and the parasitic capacitance from the transmission line is negligible if it was properly shielded and grounded. [26] However, the length of the transmission cable used should be minimized to reduced the parasitic capacitance from the transmission line

to as low as possible. For example, Li used the transmission lines of different length to vary the rise time and the RC time constant. [32]

RC time constant

Generally, the total capacitance of the measurement setup can be approximated by the equation,

$$\frac{1}{C_{total}} = \frac{1}{C_{FE}} + \frac{1}{C_{air}} + \frac{1}{C_{cantilever}} + \frac{1}{C_{cable}}, \tag{2.5}$$

where C_{total} is the total capacitance of the circuit,C_{FE} is the capacitance of the ferroelectric capacitor, C_{Air} is the capacitance of the air gap, $C_{cantilever}$ is the capacitance of the AFM cantilever, and C_{cable} is the capacitance of the transmission lines. The capacitance between the two electrodes can be defined as

$$C = \epsilon_0 \epsilon_r \frac{A}{d}, \tag{2.6}$$

where C is the capacitance (F), ϵ_0 is the permittivity of free space (F/m), ϵ_r is the dielectric constant or relative permittivity of the insulator used, A is the area of each plane electrode (m^2), d is the separation between the electrodes (m). Substituting equation 2.6 into 2.5, we can calculate the total capacitance of the system. Figure 2.14 shows the comparison between the approximation from equation 2.5 and the experimental measurements. The approximation only agrees with the measurements at the small lift height of 5.4 μm where the RC time constant was estimated to be 7.62 ns. As the tip and sample were moved further apart, the electric field lost its strength, and the air gap no longer behaved like a capacitor. This method was not an accurate way to define the parasitic capacitance as shown by Tiedke but good enough for an approximation. [26]

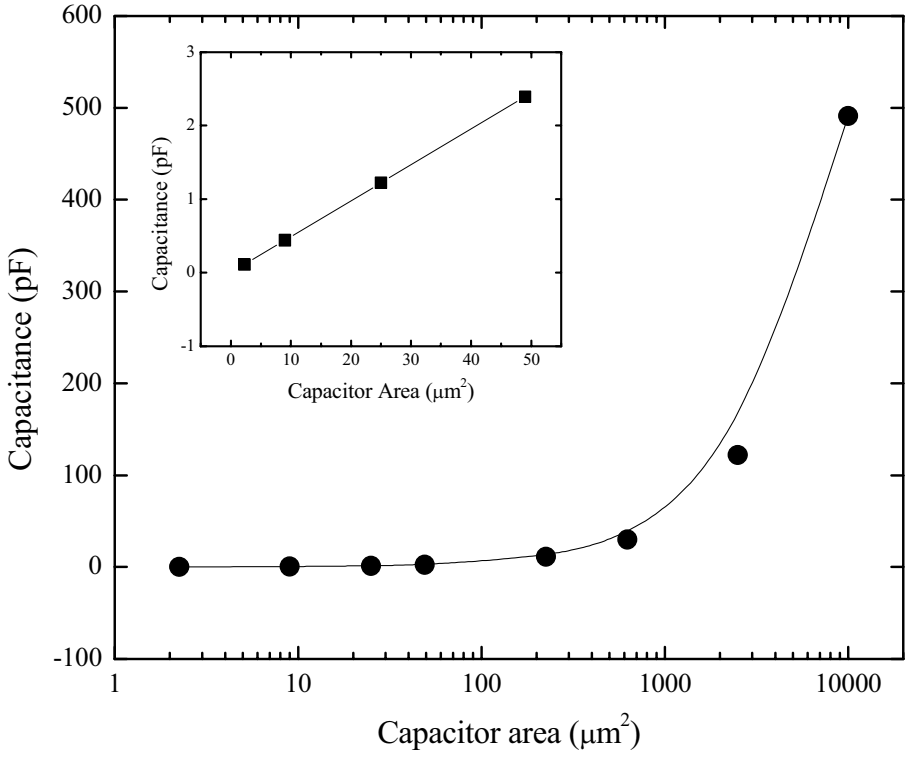

Figure 2.15: Capacitance measurements and estimation as function of capacitor sizes.

2.4.4 Signal optimization

In an early investigation, it was very important to determine the capability of the system i.e. noise level, and signal strength. Thus, this enabled us to get an accurate pulse switching signal measurement from a submicron capacitor. Figure 2.15 shows the measurements and estimation of the capacitances of micron capacitors. Capacitance measurements of 15×15, 25×25, 50×50, 100×100 μm^2 capacitors were obtained from HP4194A impedance/gain-phase analyzer, with frequency sweep $100-1$KHz, 0.5 V AC. From Table 2.2, it can be seen that the ratio of capacitance per unit area remains constant, and equals to 0.049 pF/μm^2. If we assume that this ratio remains the same, we can estimate the capacitance of the smaller sizes capacitors (shown in sub Fig. 2.15, and Table 2.3).

Further more, we could use the 0.049 ratio to estimate the capacitance of the sub-

Capacitor size (μm)	Capacitance (pF)	Capacitance/Unit area (pF/μm^2)
100	491	0.049
50	122	0.049
25	30	0.049
15	11	0.049

Table 2.2: Capacitance measurements of micron size capacitors.

Capacitor size (μm)	Capacitance = 0.049 $\times$ Area (pF)
7	2.39
5	1.22
3	0.44
1.5	0.11

Table 2.3: Capacitance estimations of micron size capacitors.

micron capacitors. For example, the capacitance of 1 μm, 0.5 μm, 0.1μm were found to be 49 fF, 24.5 fF, and 4.9 fF, respectively. The advantage of doing this estimation was that we could use a linear capacitance with the equivalent value of a ferroelectric capacitor as a dummy capacitor for testing the circuit. Figure 2.16 shows the voltage transients measured from 100 pF and 10 pF linear capacitors. Here, the 10 pF capacitor is equivalent to $\sim 15\times15$ μm^2 capacitor. As the voltage signal measured across a capacitor gets lower, it will be necessary, in the next step, to amplify the signal level.

Signal amplification

In the small signal measurements of submicron capacitors, a shunt resistor was needed to amplify the output voltage transient. Figure 2.17 shows an increase of the transient

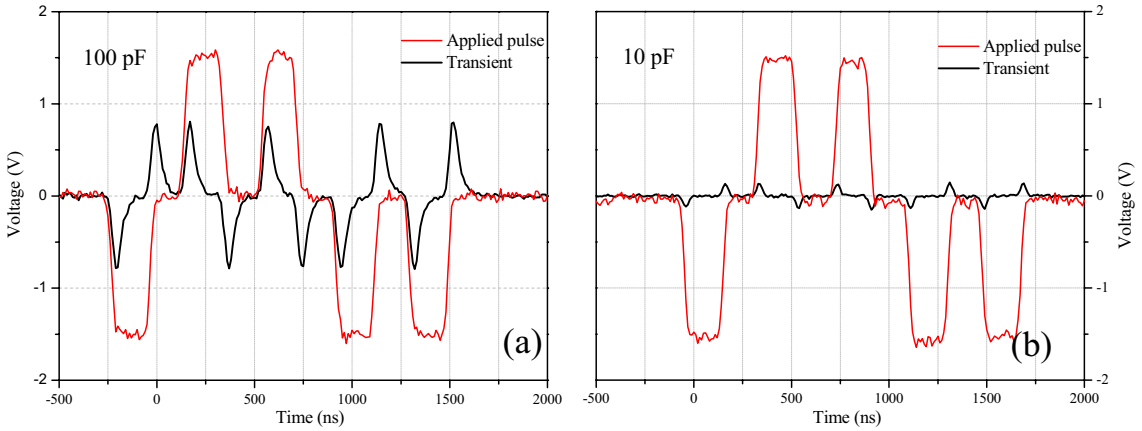

Figure 2.16: Voltage transients measured from 100 pF and 10 pF linear capacitors.

output measured from a ferroelectric capacitor as the value of the resistor increases. If was found that a 330 Ω resistor was the optimum size for submicron size capacitors. Further increase of the resistor value barely improved the signal strength i.e. using a 3 kΩ resistor gave the switching strength of 1.2 times higher while using a 7 kΩ resistor increased the signal strength about 1.6 times. Increasing the resistor beyond this value resulted in a distorted switching transient, which appeared as a distorted square pulse. In summary, the experimental setup was successfully optimized to obtain a clean switching transient output measured from a submicron ferroelectric capacitor, and the noise level was minimized to increase the measurement resolution.

Other problems associated with measurements

The most common problems associated with pulse switching measurements are reflection, noise, and ringing of the signal. Figure 2.18 shows an example of these problems appearing on the switching transients. These problems could be solved by impedance matching, electrical shielding, and grounding. In the experimental studies, it was necessary to use

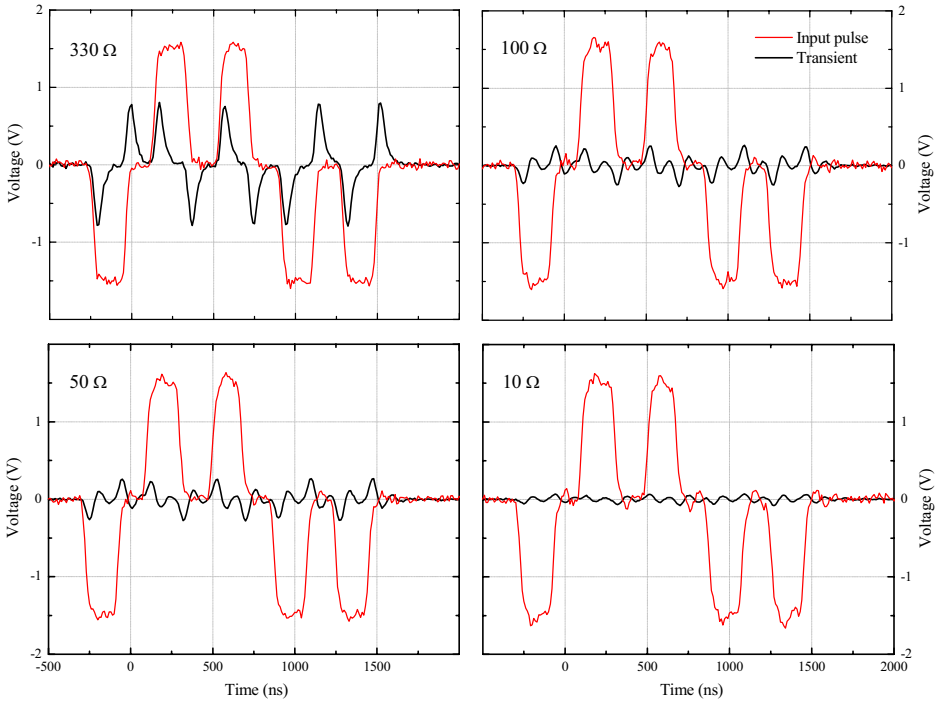

Figure 2.17: Switching transients dependent on resistors used in the circuit. Voltage signal increases as a function of resistance.

shielded cables to protect the live wire carrying the electrical signal from the electrical noise of the measurement circuit, equipment, and environment. Figure 2.19 shows the background noise level of the AFM-pulse switching setup. During the course of my research, I discovered that there was noise associated with the Labview program. When Labview was acquiring data, the module in the Labview program called CONFIG amplified the signal level, and thus, the noise level. This destroyed the smoothing configuration (S/N averaging of 200 times) that should have been obtained from the oscilloscope. The CONFIG module was required in order to get correct data acquisition. To get around this problem, the ”WAIT TIME” used in the program had to be increased i.e. from 1000 ms to 3000 ms. The contents of the computer program will not be presented in this thesis.

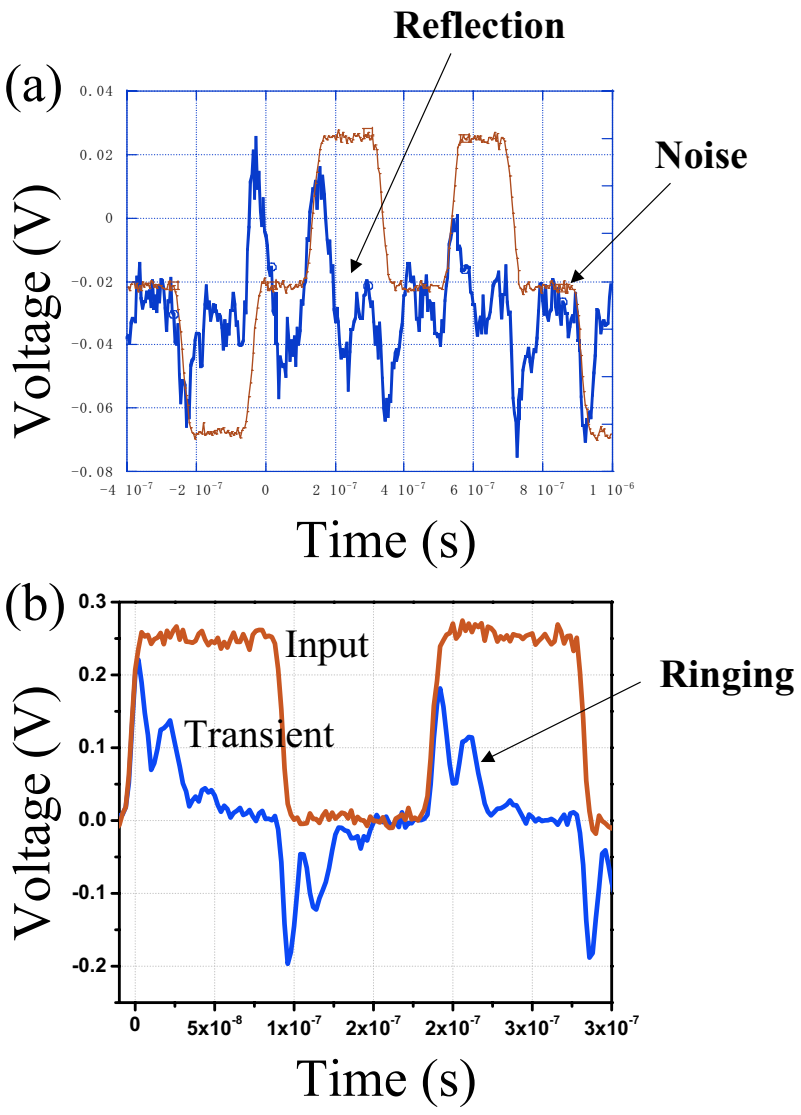

Figure 2.18: Reflection, noise, and ringing in small signal measurements.

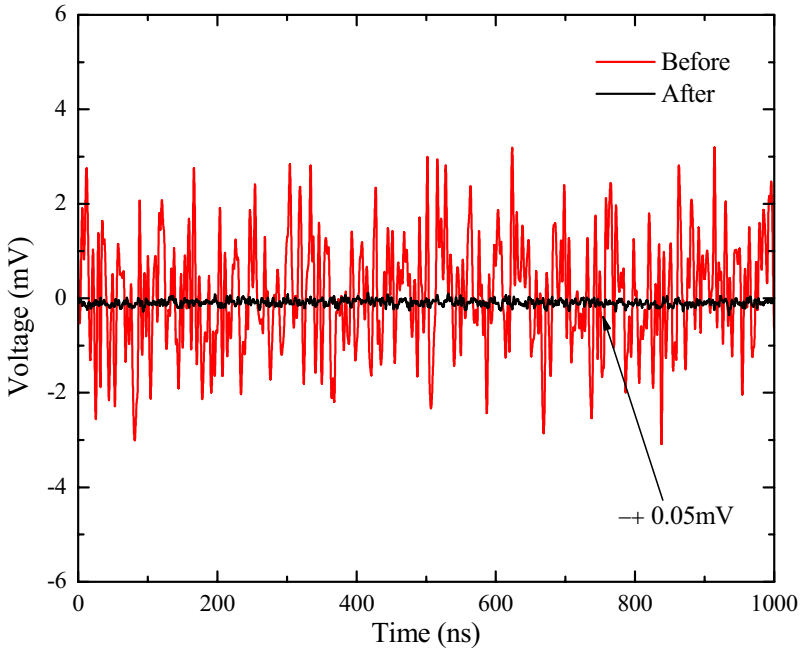

Figure 2.19: Noise level pick up by Labview data acquisition before and after system improvement. The noise level was reduced to $\pm$ 0.05 mV.

2.4.5 LabVIEW^{TM} programming

LabVIEW programs contain many variation of modules or virtual instruments (VIs) such as signal generators, oscilloscopes, and multimeters etc. These modules can be linked and built into an electrical circuit or virtual instrument on a computer. For example, a virtual user interface with a front panel containing control knobs, push buttons, and graph displays could be built to control the operating functions of the pulse generator, and to acquire the voltage output data from the oscilloscope. LabVIEW communicates with hardware and other devices via GPIB, PXI, VXI, RS-232, and RS-485. [42] Figure 2.20 shows the Labview measurement program used for the real-time measurements. This program shows the measurement results as the pulses were applied to a capacitor. For the submicron capacitors, it is recommended that passive measurements should be used i.e. the data is taken first, and analyzed later. This is because, in many cases, the small

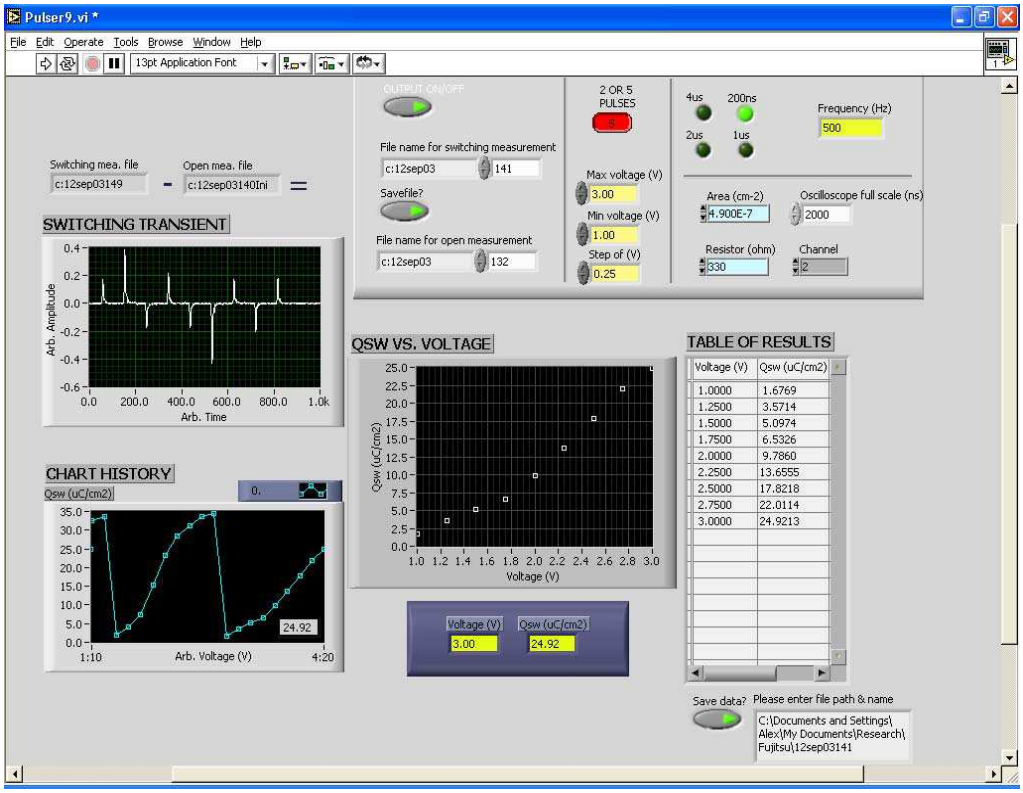

Figure 2.20: LabVIEW^{TM} pulse switching program for real-time measurements.

signal measurements need more attention in analysis. Figures 2.21 and 2.22 show the programs that were used in the passive measurements where SETPUND was used to input the PUND pulse train, and ANALYZE was used to analyze the data. Here, the SETPUND program (Fig. 2.21), containing the applied pulse information, such as pulse width, amplitudes, and cycles, was first applied to a capacitor, and recorded the data. Once the data was recorded, the ANALYZE program was then used to recall the data for the detailed analysis. The passive ANALYZE program offers more functions than the dynamic program with many capabilities such as calculations of switching parameters V_{max}, t_{max}, and t_s, data averaging and subtraction, and breaking down and saving data in different formats.

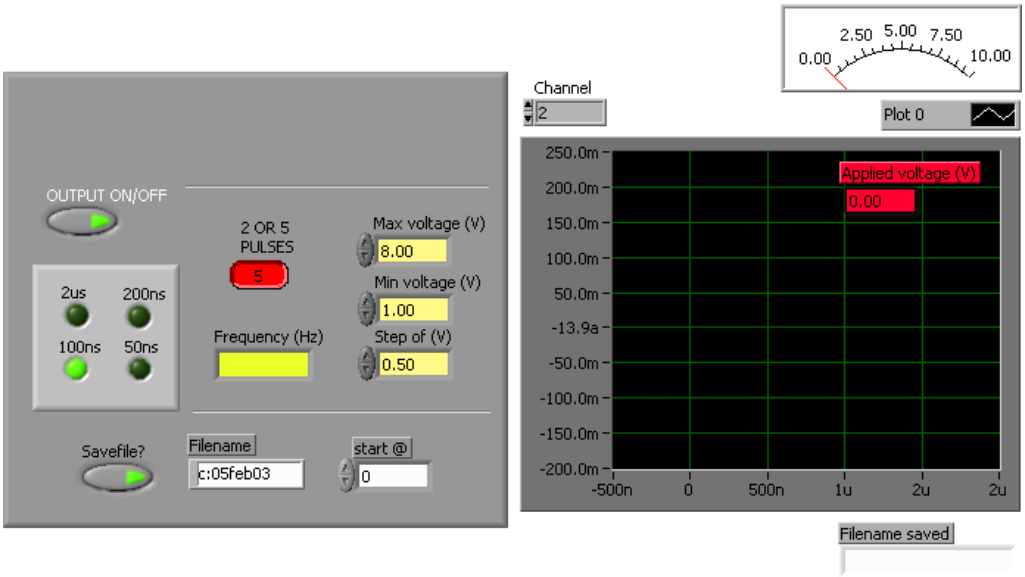

Figure 2.21: LabVIEW^{TM} (SETPUND) pulse switching program for inputting the PUND pulse train.

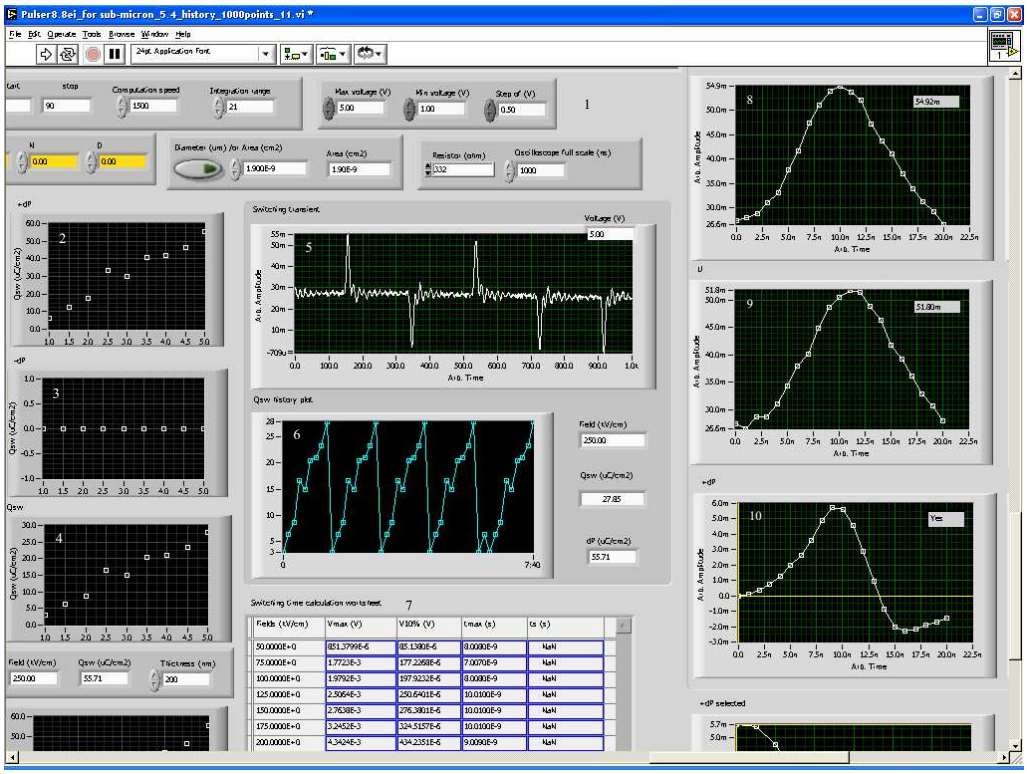

Figure 2.22: LabVIEW^{TM} (ANALYZE) pulse switching program for analyzing the pulse measurement data.

Manual method

In this method, it is assumed that users have fundamental knowledge about the functions of pulse generators and oscilloscopes. Instructions for using this equipment can be found in the user manuals. In the manual method, the PUND train is set on the pulse generator. The PUND waveform can be saved on the pulse generator for later use. Once the pulse width and delay periods and their amplitudes are set, press the output button on the pulse generator to apply (input) the PUND pulse train to a capacitor. The voltage signal output from the circuit corresponding to switching of the ferroelectric capacitor will appear on the oscilloscope display screen. The waveforms on the oscilloscope can be saved onto a floppy disk as the ASCII file and transferred to a computer. Finally, use the computer software Microcal Origin to plot the voltage transient output and integrate the area under the graph to find the number of charges, and hence the switching polarization.

Automated method

In this method, it is assumed that users have basic knowledge of Labview programming. The PUND waveform parameters such as pulse width, delay, and amplitude are set in the program. For the voltage series measurement, set the minimum and maximum voltage, and voltage interval i.e. minimum voltage = 1 V, maximum voltage = 5 V, and voltage interval /or step = 0.5 V. In this case, the pulse generator will apply the PUND pulse train from 1 to 5 V at intervals of 0.5 V. After each PUND pulse train is applied, the voltage output signal from the measurement circuit is recorded. The recorded transient waveform is then divided into different sections P, U, N, and D. The voltage data is transferred to the Labview mathematic integration module where the integration starting point and

range can be set. The methods of finding the starting points for the integration will be discussed in Chapter 3. In this case, the starting points were calculated automatically from the voltage signal. After integration, other mathematic functions were used to compute the switching properties such as polarization versus voltage /or fields, P^*, $P^\wedge$, and $\triangle P$ voltage transients, i_{max}, t_m, and switching time t_s. The raw data saved could be pulled up and analyzed off-line for later use. Comparing between the manual and automatic methods, the manual method takes a few hours for each data series, whereas the automatic method takes a few minutes.

2.5 Summary

The measurement setup for pulsed probing was based on a combination of a pulse generator, an AFM, a shunt resistor, and a digital sampling oscilloscope that was used to measure the switchable polarization of a submicron capacitor. The input parameters, such as pulse sequence, width, delay, and amplitude, were adjustable and could be used to mimic the operating conditions for the actual FRAM capacitors, such as 3 V pulses of $10-50$ ns with similar delay time between the pulses. The circuit layout for the pulse measurement was the same as Aoki et al., [34] except that a commercial AFM (Digital Instruments Nanoscope IV, D3000), equipped with an Rh-coated 100-nm-thick silicon-based conductive cantilever, was used to make electrical contact with the capacitor. The thick-coated Rh layer helps to prevent the vaporization of the coating due to the high current density, and it thus prolongs good electrical conductivity of the tip. A waveform generator (Agilent 32250A) was used to generate pulses, in conjunction with an

oscilloscope (Tektronix^{TM} 620B) that was used to record the switching responses. In the measurement, we applied the PUND sequence of pulses and obtained the switching transients corresponding to P, U, N, and D pulses. [31, 43]

Before a PUND pulse train was applied, the capacitor was trained by applying bipolar pulses of 3 V (200 ns width and delay) for 60 s to obtain a saturated $\triangle P$ value. It should be noted that for the study of switching dynamics, such as the switching speed, a rise time less than 1 ns is desirable. [33] However, such conditions cause ringing in the switching signal, thereby distorting it. Therefore, in our measurements, the optimum conditions were an 8 ns rise time ($10\% - 90\%$), sensed through a 330 V load resistor. These conditions minimized the ringing effect, and provided sufficient signal strength of 16 mV for the submicron capacitors. The maximum noise level in the measurement was ± 0.05 mV$_{pk-pk}$. In order to compare our results with quasistatic behavior, I also measured the polarization hysteresis of capacitors using a TF Analyzer 2000 from aixACCT Systems. In both voltage and pulse width experiments, I used the average integrated values of transients corresponding to each P, U, N, and D pulse to calculate the $\triangle P$. [35, 44] The voltage transients of the capacitor and the parasitic were processed with a S/N averaging of 200 times, and followed by a five-point curve smoothing. For each capacitor, we repeated this experiment 10 times, and measured 10 capacitors in total to find the mean $\triangle P$.

Chapter 3

Lateral scaling

3.1 Introduction

The objective of this chapter is to investigate the scaling effects of ferroelectric capacitors from micron to the submicron areas. In this investigation, the pulse switching setup equipped with AFM was used to measure the switching voltage vs. time transients. From the measurement results, various switching parameters such as maximum current (i_{max}), switching time (t_s), and switching polarization (ΔP)were extracted. This information was fed into the theoretical models to determine the intrinsic properties. In this chapter, we are trying to answer the following questions: i) Is there a change in the intrinsic properties as a function of scaling? If so, what is the critical lateral size? ii) What is the ultimate switching speed of a ferroelectric capacitor and what is the rate-limiting parameter? [45]

3.2 Background

3.2.1 Polarization reversal

The linear relationship between electric displacement, field, and polarization can be expressed as

$$D = \epsilon_0 E + P, \tag{3.1}$$

The polarization arises from both the polarizability in the presence of a field $P_E = \chi E$, and from the spontaneous alignment of dipoles P_s. Ferroelectrics can be distinguished from other pyroelectrics due to the reversibility of spontaneous polarization. Valasek demonstrated the polarization reversal for the first time in 1920 using the Sawyer-Tower circuit to observe the hysteresis loops. At low and high fields, the ferroelectric material behaves like ordinary dielectric (usually with high a dielectric constant) but around the coercive field E_c, polarization reversal occurs giving a large hysteretic, dielectric non-linearity. The area under the loop measures the energy required to reverse the polarization twice. At zero field, the electric displacement of a single domain has two values corresponding to the opposite orientations of the spontaneous polarization; but in the multi-domain crystal, the average zero-field displacement can have any value between the two extremes. In principle, the spontaneous polarization is equal to the saturation value of the electric displacement extrapolated to zero field. It is important to note that the remanent polarization P_r may be different from the spontaneous polarization P_s if reverse nucleation occurs before the applied field reverses. This can happen either in the presence of internal (or external) stresses or if the free charges below the crystal surfaces cannot reach their new equilibrium distribution during each half-cycle of the loop. This effect can be minimized by cycling the loop at very low frequencies. However, there are precautions that must be considered for this type of measurement. First, the measurement can be erroneous if part of P_s is clamped. Second, the ferroelectric hysteresis can easily be confused with non-linear dielectric loss. The coercive field is also a function of the frequency of the alternating field since there is some switching time associated with polarization reversal. The shape of the loop consequently depends on the dependence of the switching time on

the applied field.

The first quantitative experiments to determine the time and field dependence of polarization reversal were carried out by Merz (1954) on $BaTiO_3$. [7] The experimental procedure involved applying a step-function field to the crystal and measuring the displacement current density J = dP/dt as a function of time. This procedure is the most direct method for studying the switching behavior for crystals of very low conductivity. For conducting crystals the conduction current obscures the displacement current, and other techniques such as piezoelectric (Husimi and Kataoka 1960) are more suitable because that one also gives a quantitative, non-destructive measure of the polarization. For $BaTiO_3$, the switching time followed an exponential law

$$t_s \propto e^{\alpha/E} \tag{3.2}$$

for fields from 1 to 15 $kVcm^{-1}$, while higher fields up to 100 $kVcm^{-1}$

$$t_s \propto E^{-n} \tag{3.3}$$

where the index n was about 1.5 for $BaTiO_3$.

There has been a great deal of experimental and theoretical work on the mechanism of polarization reversal and domain dynamics. The switching behavior can be greatly affected by the nature of the electrodes, crystal surfaces, electrical conductivity, domain geometry, and presence of defects. Polarization reversal can be accomplished by the growth of existing domains antiparallel to the applied field, by domain-wall motion, or by the nucleation and growth of new antiparallel domains. The domains can grow either along the polar direction or by sideways motion of 180° domain walls. Sideways motion

of 180° domain walls is preferred to forward motion. Direct measurement of the domain-wall motion and switching current showed that the wall velocity in $BaTiO_3$ varied as

$$\nu = \nu_\infty e^{-\delta/E} \tag{3.4}$$

where δ is a constant up to 300 Vcm^{-1} which appears to depend on the defect concentration of the crystal.

3.2.2 Landau-Ginzburg-Devonshire theory

This section is to introduce the activation field parameter which will be used as a tool to explain the scaling phenomenon. To explain the meaning of the switching polarization, two approaches have been taken. The first is the theory proposed by Devonshire to describe the free energy as a function of temperature and polarization. The second uses nucleation and growth kinetics and the domain wall energy calculations. The activation field can be described as the amount of energy required to switch 95% of the total polarization and is not the same as the coercive field. The theory relates the free energy as a function of temperature and polarization. The elastic Gibbs free energy expressed in terms of stress, displacement and temperature can be represented as the polynomial function,

$$G = G_0 + (\alpha/2)D^2 + (\beta/4)D^4 + (\gamma/6)D^6 \tag{3.5}$$

under the assumptions that all stresses equal zero, the paraelectric phase is centrosymmetric and the spontaneous polarization is directed along only one crystallographic axis with the electric field. (It is assumed that this field is along the z-direction perpendicular to the plane of the capacitor). The signs of β and γ are all assumed positive for a second order

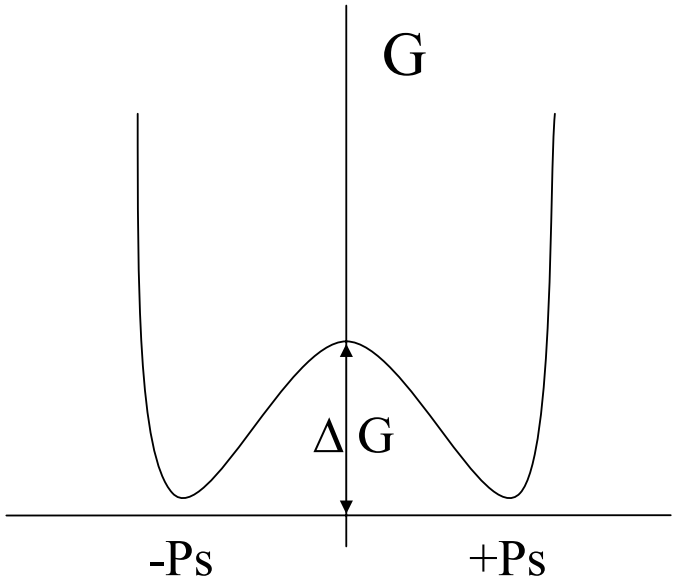

Figure 3.1: Gibbs free energy diagram shows the free energy necessary to switch from a -P_s to a +P_s spontaneous polarization state. [2, 3]

phase transition, but a negative sign of β implies a first order phase transition. The ferroelectrics described in this dissertation all undergo a first-order paraelectric-ferroelectric phase transition. The coefficients β and γ are generally assumed temperature independent for simplicity. The α coefficient on the other hand can be expressed as $A(T - \theta)$, where θ is the Curie-Weiss temperature and A is the reciprocal Curie constant. A is positive for all known ferroelectrics, and ν is the reciprocal isothermal permittivity at constant stress in the paraelectric phase. θ represents the temperature above which the metastable non-polar paraelectric phase exists and below which only that stable ferroelectric phase exists. θ should not be confused with the Curie temperature T_c where the ferroelectric-paraelectric phase transition occurs. Equation 3.5 can be used to determine the minimum free energy necessary to switch from a -P_s to a +P_s spontaneous polarization state, for example, as shown in the Gibbs free energy diagram in Fig. 3.1. [2, 3] When equation 3.5 is differentiated with respect to P, equation 3.6 for the electric field E is obtained as a

function of P. This equation also helps in describing the general shape of the hysteresis loop.

$$(dG/dP) = E = \alpha P + \beta P^3 + \gamma P^5 \tag{3.6}$$

Since the thermodynamics quantities α, β and γ have been studied extensively and determined by Merz, Devonshire, and Drougard for $BaTiO_3$, one can use these values to get some idea about the amount of energy necessary to cross the barrier, considering the above assumptions. [3, 7] Equation 3.6 can be minimized with respect to P and set to zero in order to obtain the polarization at +P and -P at the coercive field of the P-E curve. The equation is

$$(dE/dP)_{X,T} = \alpha + 3\beta P^2 + 5\gamma P^4 = 0 \tag{3.7}$$

It was found that the theoretical values are significantly higher than the calculated values. This is because the phenomenological theory does not account for the microscopic details of the ferroelectric capacitor. It assumes that the ferroelectric is a homogeneous material with no preferential sites to initiate the reversal of polarization. These factors are not necessarily true in real crystals. One can conclude from the comparison of the theoretical and the observed coercive fields that the ferroelectric in practice has a shallower energy well compared to that predicted by the theoretical model. The measured values of the coercive field are much lower than would be the case if the material changed its polarization in a uniform fashion throughout the ferroelectric. It is therefore assumed that the reversal of polarization is made particularly easy at certain points within the ferroelectric and that the domains of reversed polarization spread out from these preferential sites. The reversal of the domains therefore must proceed by a method other than a uniform reversal manner

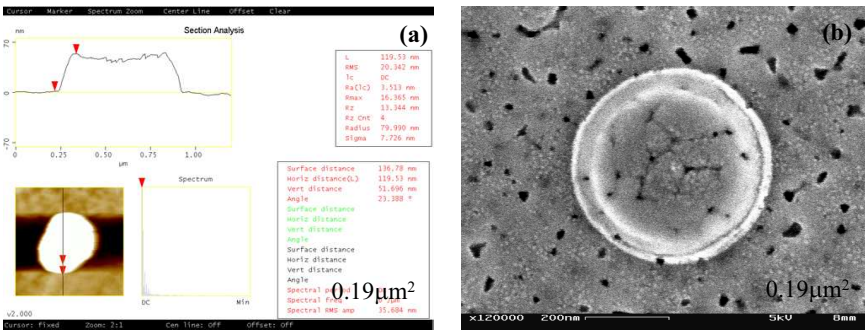

Figure 3.2: (a) and (b) shows AFM and SEM images of 0.19 μm^2 capacitor patterned by RIE.

throughout the ferroelectric.

3.3 Thin film preparation

The sample used in this study was the sputtered 200-nm-thick polycrystalline (111) lead zirconium titanate $PbZrTiO_3$ thin films, with an IrO_2 top electrode and a Pt bottom electrode, deposited on a Si/SiO_2 /Ti substrate, with capacitor sizes from 40000 to 0.19 μm^2. The scaled capacitors were patterned using reactive ion etching (RIE). Figure 3.2 (a) and (b) shows AFM and secondary electron microscopy (SEM) images of 0.19 μm^2 capacitor patterned by reactive ion etching (RIE). Both AFM and SEM instruments were calibrated. The images show excellent conformity and uniformity of the submicron capacitor investigated. The capacitor areas were calculated by counting the number of grids drawn on the SEM image. In addition, the AFM image was used to confirm the accuracy of the area calculations.

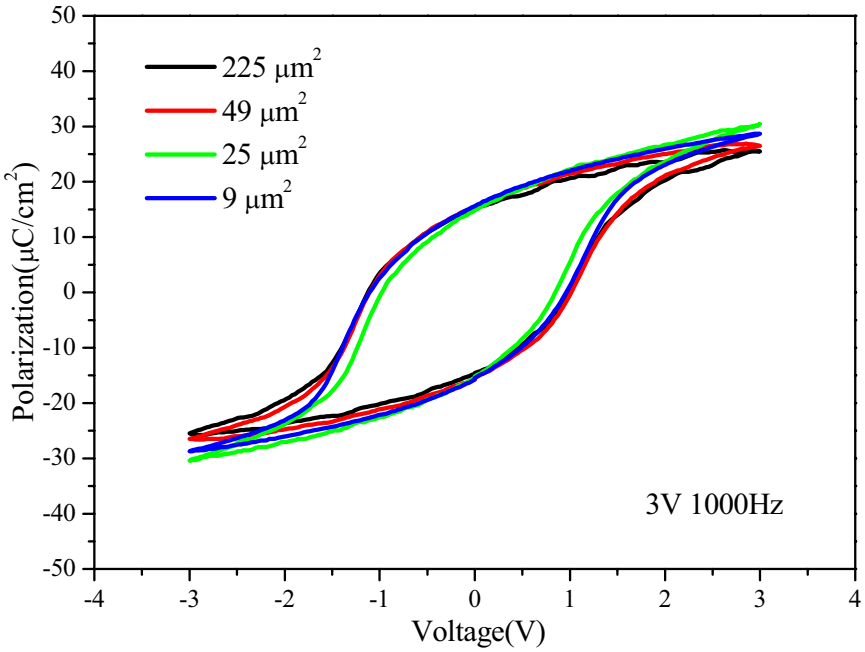

Figure 3.3: Polarization hysteresis loops of square capacitors scaled down from 225 to 9 μm^2.

3.4 Results

3.4.1 Hysteresis

Prior to the pulse switching measurement, polarization hysteresis measurements were carried out to screen and evaluate the polarization properties. Figure 3.3 shows the polarization hysteresis loops of square shape capacitors scaled down from 225 to 9 μm^2. The capacitors show approximately the same properties where the remanent polarization equals 15.2$\pm$0.37 μC/cm^2, and the coercive voltage equals 1.02$\pm$0.07 μC/cm^2.

Figure 3.4 shows the polarization hysteresis loops of the scaled capacitors (a) as measured, and (b) 40-points averaging with parasitic compensation. In Fig. 3.4(a), it can be seen that as the capacitors scaled down from micron to submicron areas, the quality of the hysteresis loop deteriorated due to parasitic, and electrical noise. Figure 3.4(b) shows the measurements using the enhanced compensation procedure described by Tiedke to

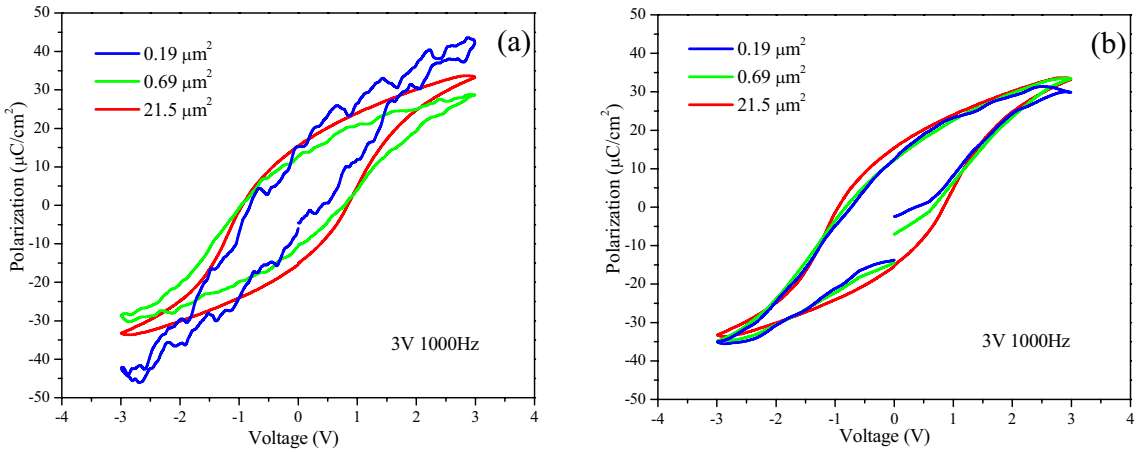

Figure 3.4: Polarization hysteresis loops of scaled capacitors (a) as measured, and (b) 40-points averaging with parasitic compensation.

eliminate the influence of parasitic capacitance from the measurement setup.[26] The parasitic value is obtained from the hysteresis when the AFM tip is lifted above the capacitor's top electrode. The parasitic capacitance is subtracted from the polarization hysteresis of a capacitor. It should be noted that this compensation method can be inconsistent because the slope could be tilted, and the amount of the parasitic varied depending on tip-sample separation which means that the polarization values could be manipulated. Even though, the enhanced compensation procedure was used, the quality of the hysteresis measurement still needs to be improved as the polarization hysteresis of 0.19 μm^2 is affected by noise [see Fig. 3.4(a)]. The noise level was reduced by using the shielded coaxial cables, and proper grounding of cables. The parasitic capacitance was reduced by minimizing cable length and diameter. Otherwise, further optimization of the hysteresis measurement was limited, and mostly depended on the ferroelectric tester.

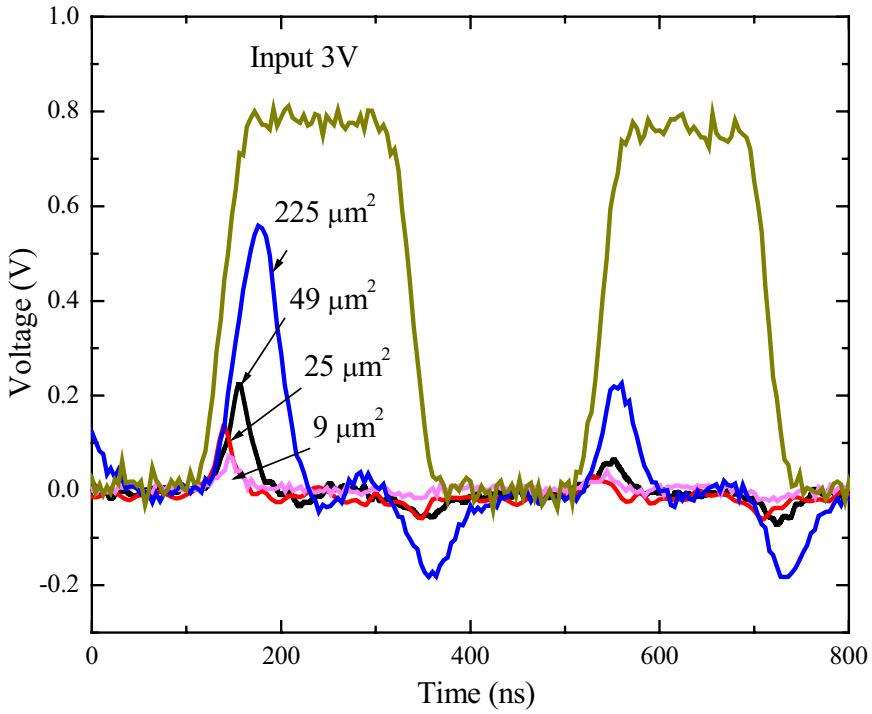

Figure 3.5: Switching transient of voltage versus time as a function of capacitor areas scaled from 225 to 9 μm^2.

3.4.2 Pulse switching

To evaluate the capacitor properties, two sets of experiments were conducted. The $\triangle P$ was measured first as a function of voltage between 1.5 and 5 V, where the pulse width and the delay time were fixed at 200 ns, and second, as a function of pulse width between 100 ns and 1 μs, where the delay time and the applied voltage were fixed at 3 s and 3 V, respectively. Figure 3.5 shows the switching transients of voltage versus time as a function of the capacitor for the same areas scaled from 225 to 9 μm^2. It can be seen that as the capacitor area scales down to 9 μm^2, there is a drastic decrease in the switching signal. Therefore, it was necessary to increase the equipment's resolution by increasing the signal to noise ratio. This could be done by amplifying the output voltage signal and reducing the noise level.

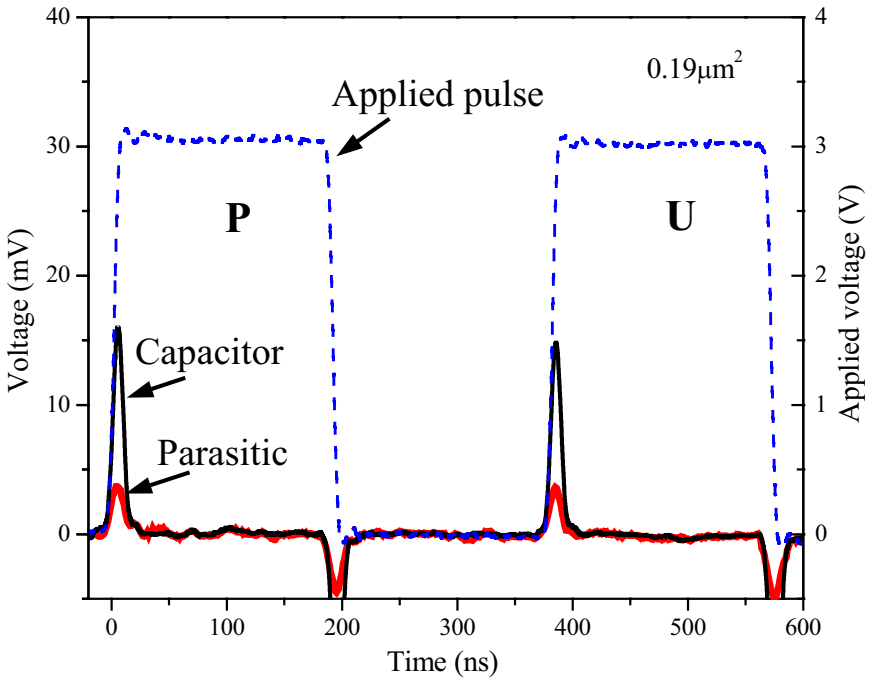

Figure 3.6: Profile of P and U pulses applied to 0.19 μm^2 capacitor. The figure shows the applied pulse as dashed lines, and the response of the capacitor and the parasitic in black and red, respectively.

Figure 3.6 shows the input pulse, the transients of a 0.19 μm^2 capacitor and a parasitic signal. The transients of the switching and the nonswitching terms were found to be symmetrical in both positive and negative polarities. Figure 3.6 also plots the parasitic contribution measured by lifting the AFM tip. It shows an equal parasitic contribution to the P and U pulses, therefore, the subtraction between switching (P^*) and nonswitching terms ($P^\wedge$) to calculate $\triangle P$ will automatically eliminate the parasitic contribution.

Measurements processing and analysis

The small magnitude of the actual voltage signal corresponding to the switched polarization necessitates careful analysis of the output data, specifically, the location of V=0 and t=0 points. We have therefore used three methods to analyze the data, as depicted in Fig. 3.7, in order to locate these zero-points.

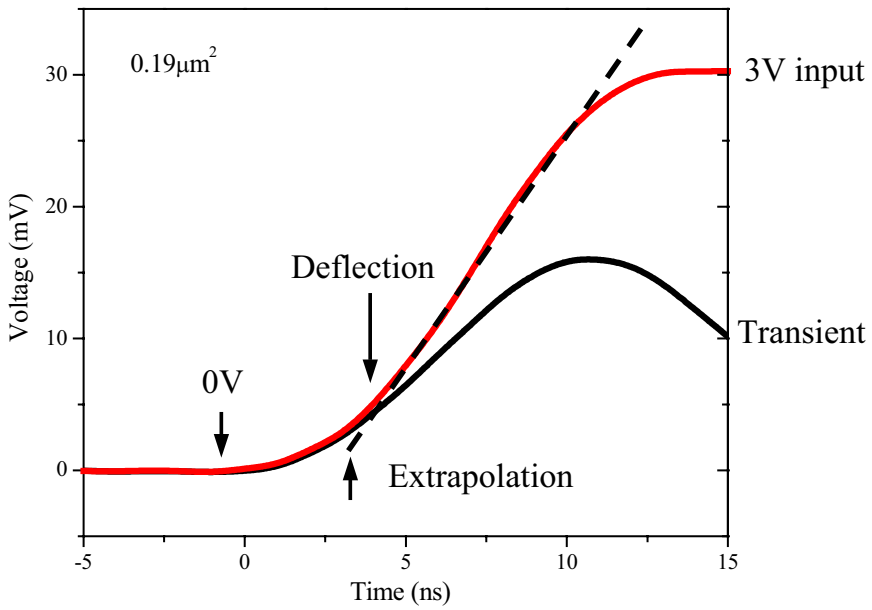

Figure 3.7: Graphical description of the three methods used to identify onset of the transients. The arrows point out the respective onset for each method.

1. An arbitrary zero voltage point, for which the first zero value in the input pulse was used as the starting point. In this method, the onset was not well defined since it was possible to use any onset positions between the transient peaks as long as dV/dt=0. [46]

2. Determining the deflection point ($d^2V/dt^2=0$) in the input voltage pulse.

3. Linear extrapolation of the rising part of the input signal.

In this study, we present the output responses, analyzed using the deflection approach, since that could be executed consistently. Figure 3.8 shows the plot of P^*, $P^\wedge$, and $\triangle P$ by this technique (with and without smoothing) of 0.19 μm^2 capacitor at 3 V. The $\triangle P$ value calculated by integrating the area under the transient was 30 μC/cm^2($\pm$3 μC/cm^2).

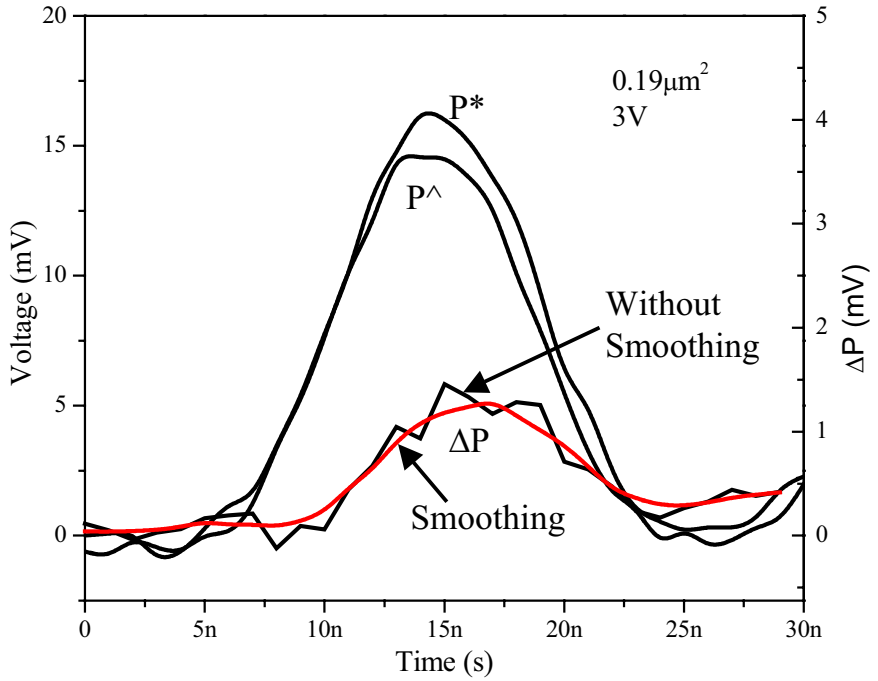

Figure 3.8: Switching (P^*), nonswitching ($P^\wedge$) and the $\triangle P$ transients for a 0.19 μm^2 capacitor. The figure also shows $\triangle P$ with and without curve smoothing.

As discussed in the following paragraph, this obtained value is comparable to the $\triangle P$ of the larger 21.5 μm^2 capacitor, thereby indicating there is no significant drop of the switched polarization when the device is scaled down to the submicron regime. In Fig. 3.9, we plot the $\triangle P$ as a function of the applied voltage for a 0.19 μm^2 capacitor, calculated using the three approaches outlined in the previous paragraph. Also shown is the value obtained after smoothing the $\triangle P$ response. All three approaches yield $\triangle P$ values that are mutually consistent. The $\triangle P$ values obtained from the deflection and extrapolation methods were approximately the same, whereas the values from zero voltage were generally higher. It is suspected that this difference is originating from the increased time interval over which the integration is performed for the zero-voltage method.

In Fig. 3.10, the $\triangle P$ was plotted as a function of applied voltage for three capacitor sizes, 21.5, 0.69, and 0.19 μm^2. There was no significant difference in the switched

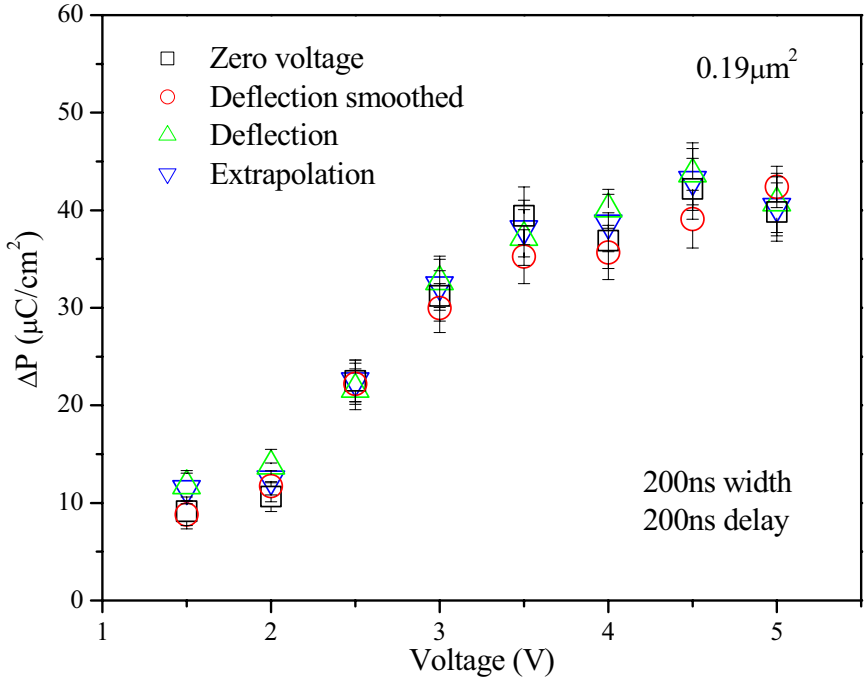

Figure 3.9: $\triangle P$ vs voltage as a function of the data analysis method.

polarization when the capacitor area is scaled down to 0.19 μm^2. For example, the $\triangle P$ values measured at 3 V for the 21.5, 0.69, and 0.19 μm^2 capacitors were found to be 32, 29 ($\pm$2), and 30 μm^2 ($\pm$3 μm^2), respectively.

Results summary

Figure 3.11 shows the switching transients $\triangle P$ for all the capacitors in this investigation for 225 (a), 49 (b), 21.5 (c), 7.74 (d), 0.69 (e), and 0.19 (f) μm^2 capacitors. Generally, the profiles of the switching transients measured as a function of voltage of the capacitors show the same trend with an increase of the maximum current i_{max} and a decrease of the corresponding time t_{max} as the applied voltage increases from 1 to 5 V. For example, Fig. 3.11(d) represents the ideal quality voltage profile of the switching transients. However, it can be seen that this ideal trend is deviated in the measurement of the submi-

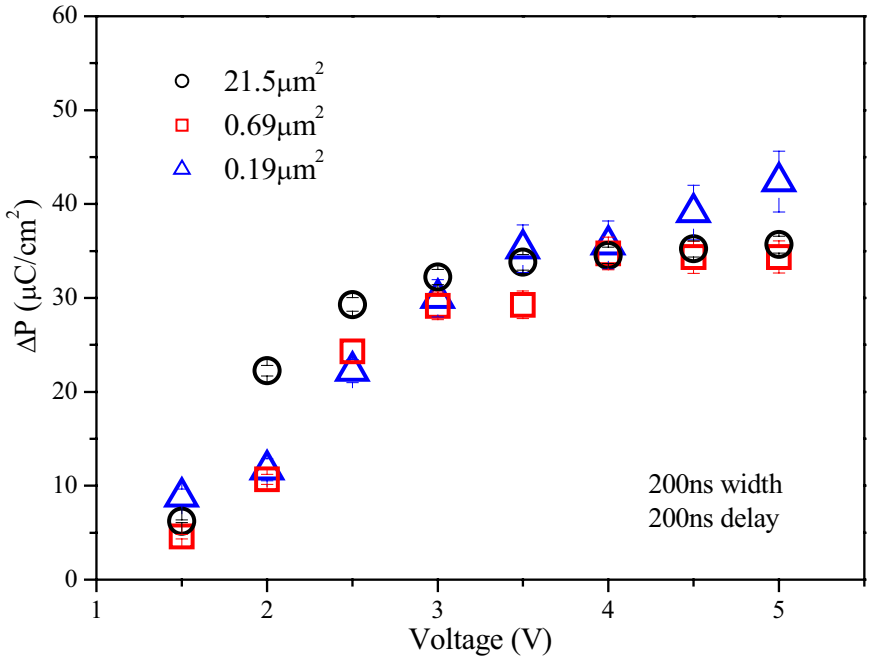

Figure 3.10: $\triangle P$ vs voltage as a function of lateral capacitor size, obtained by the deflection method. The plot shows that the switchable polarization for 21.5 and 0.19 μm^2 capacitors are comparable.

cron capacitors due to circuit effects such as noise and ringing [Fig. 3.11(f)]. Figure 3.12 shows the switching transients of 0.69 μm^2 capacitor measured under positive and negative pulses. The transient profiles show excellent symmetry indicating that the submicron capacitors are well behaved in both directions of switching.

Hysteresis vs. pulse switching

We now compare the results of these pulsed measurements for capacitors of various sizes with the polarization obtained from a quasistatic hysteresis measurement. Polarization hysteresis is considered to be a standard technique, which allows for fast characterization of ferroelectric thin films, but it does not test suitability for ferroelectric memories. Investigations on the time scale of memory operations, *i.e.*, in the range of 10-100 ns, are necessary. [33]. Figure 3.13 shows the $2P_r$ value obtained from quasistatic hysteresis

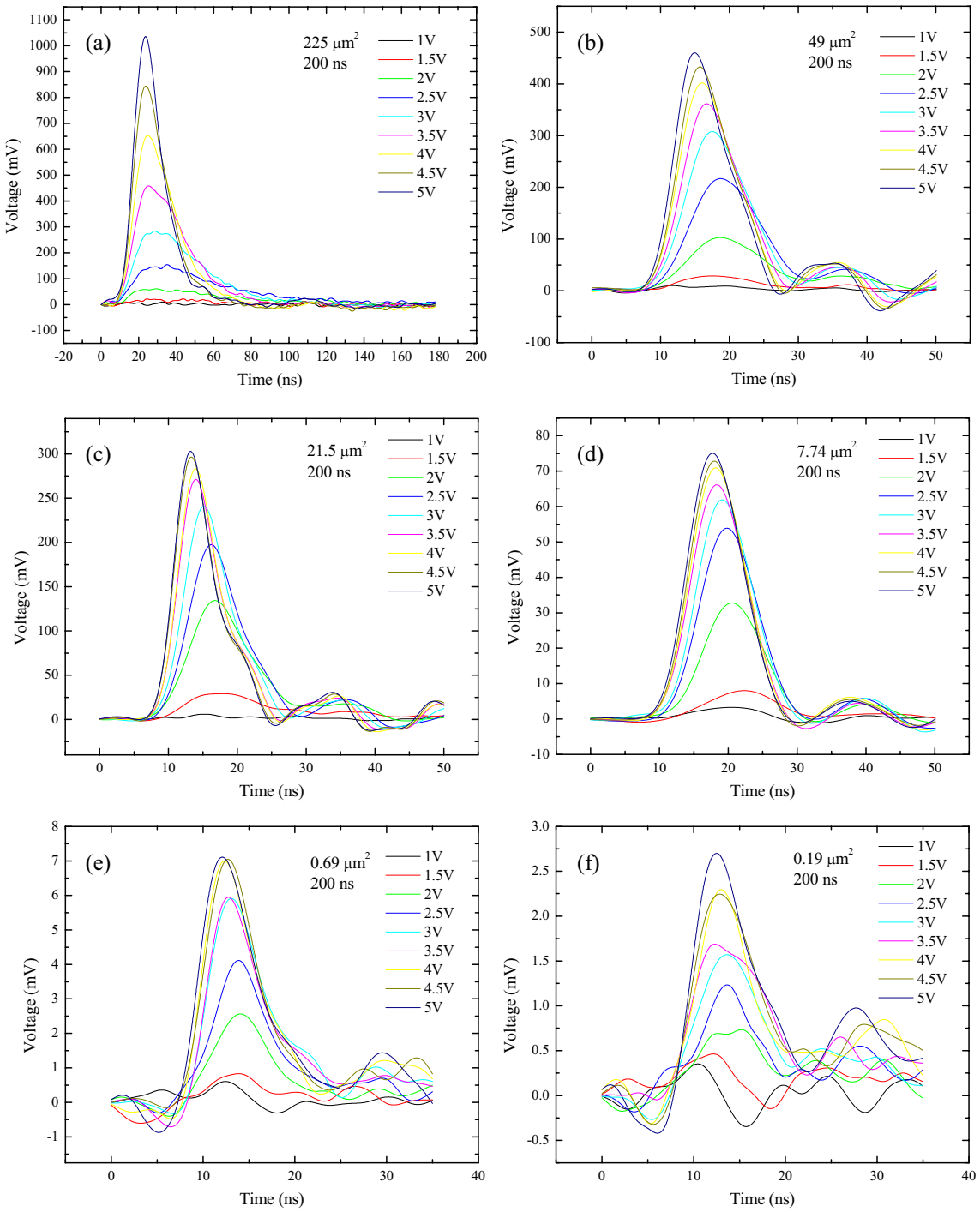

Figure 3.11: Switching transients as a function of voltage of (a) 225, (b) 49, (c) 21.5, (d) 7.74, (e) 0.69, and (f) 0.19 μm^2 capacitors.

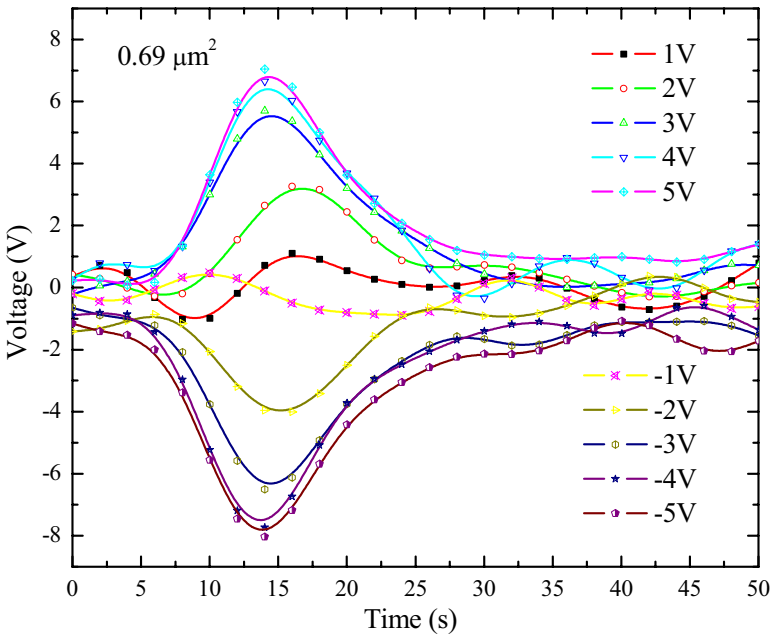

Figure 3.12: Switching transients of 0.69 μm^2 capacitor showing excellent symmetry when measuring under positive and negative pulses.

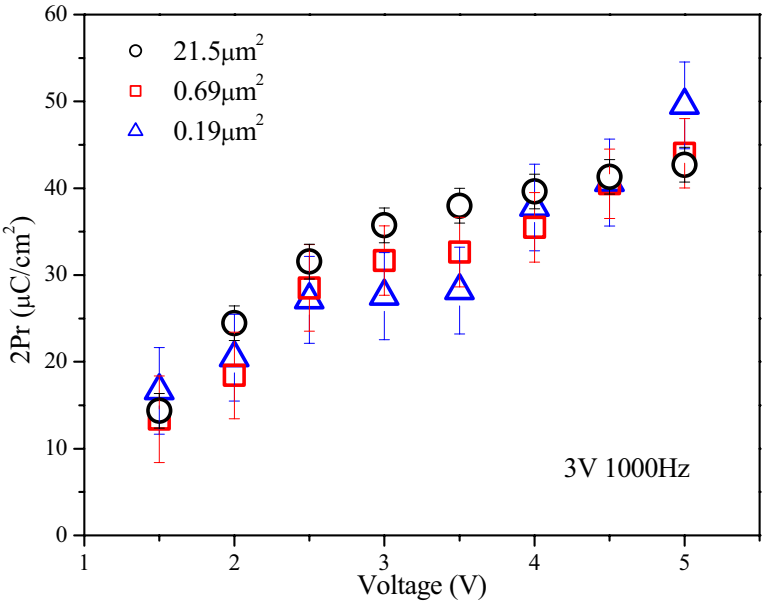

Figure 3.13: 2Pr vs voltage as a function of device size.

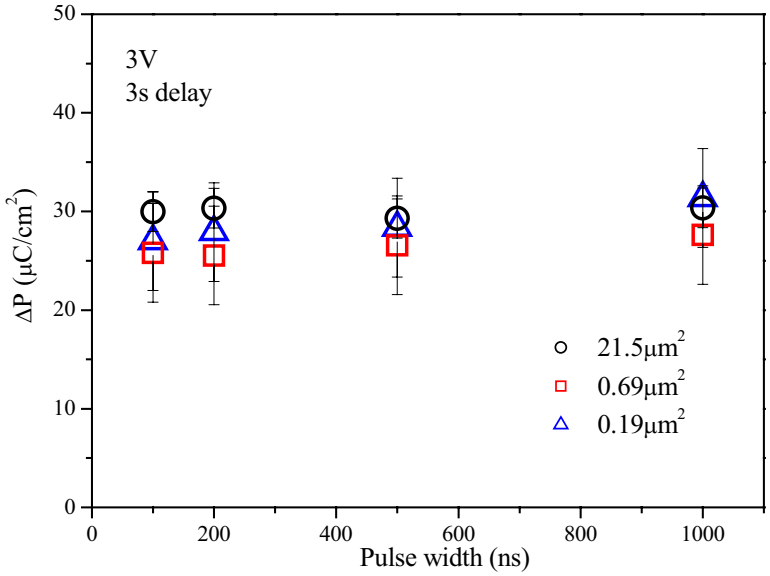

Figure 3.14: $\triangle P$ vs pulse width for all three capacitors measured by applying a pulse of 3 V with a 3 s delay. The plot shows no observable pulse width dependence, within experimental error.

loops as a function of applied voltage for capacitors of three sizes. The $\triangle P$ value was found to be lower than the $2P_r$ value as the hysteresis measurements were convoluted with leakage current.

Pulse width

Figure 3.14 shows $\triangle P$ versus pulse width for the three capacitor sizes. In the pulse width experiment we used a different pulse scheme, in which the P, U, N, and D pulses were applied individually, with a 3 s delay due to the data acquisition period. This scheme was necessary so that the pulse widths could be accurately controlled independent of the delay time. It is observed that within experimental error the $\triangle P$ value is independent of the pulse width.

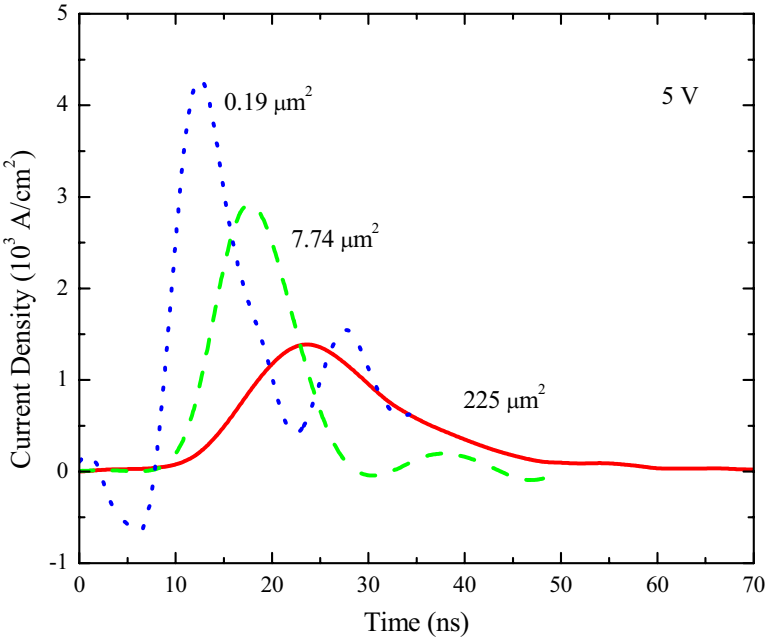

Figure 3.15: Current density vs. time of 225, 7.74, and 0.19 μm^2 capacitors. The shape of transients becomes narrower with reduction of the RC time constant as capacitor area decreases from micron to submicron range.

3.5 Analysis

3.5.1 Ishibashi Model

The classification of the switching process in ferroelectrics depends on the shape of reversed domains, initial size, and nucleation rate, shown in Fig. 3.16 for: a) one-dimensional plate-like nuclei, b) two-dimensional cylindrical nuclei, and c) three-dimensional spherical nuclei. In each case, it was assumed the boundary moved at a constant wall velocity ν under a constant applied field E. These switching processes are often analyzed on the basis of the Kolmogorov-Avrami (K-A) model. [16–18] While the Kolmogorov theory provides the probability of nucleation and growth, the Avrami theory can provide the basis for the switching by considering the different types of nucleation, and domain growth.

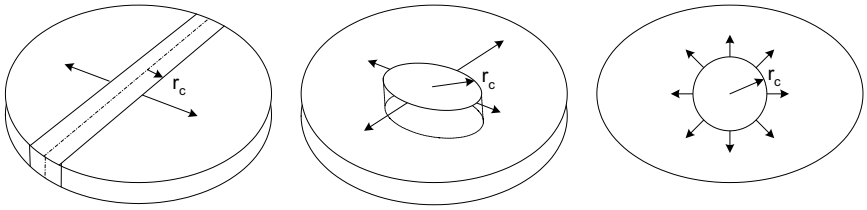

Figure 3.16: Type of domain growth and dimensionality (n) where (a) n=1, (b) n=2, (c) n=3.

Kolmogorov theory

The Kolmogorov theory [47] assumes that i) the probability of formation on crystallization center during the time between t and t + Δt is

$$\alpha(t)V'\Delta t + o(\Delta t), \tag{3.8}$$

where V' is the volume given at anytime, $o(\Delta t)$ is infinitesimal with respect to Δt, and ii) the crystal grows at a linear rate

$$c(t, n) = k(t)c(n), \tag{3.9}$$

depending on time t and direction n. The above equations holds true for uniform growth in all directions with crystals similarly oriented in space. Furthermore, probability of the nucleation and growth of ferroelectric domains can be divided into two categories; i) the α model where the number of domains increase continuously

$$q(t) = exp[-(t/t_0)^{n+1}], \tag{3.10}$$

and ii) β model where the domains are formed instantaneously

$$q(t) = exp[-(t/t_0)^{n}]. \tag{3.11}$$

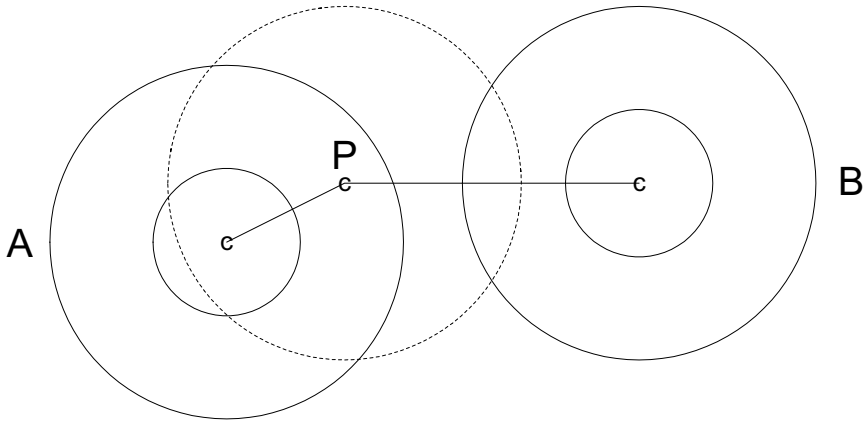

Figure 3.17: Switched volume diagram showing P in the volume A but not in volume B.

Avrami Theory

In the Avrami theory [16–18], the characteristic time, which describes the transformed volume of nuclei as a function of time, was introduced. Figure 3.17 shows the switched volume diagram where point P exists in volume A but not in volume B. From Fig. 3.17, the switched volume S after time t can be expressed as

$$S(t,\tau) = Cr_c + \nu(t-\tau)^n, \tag{3.12}$$

where n is the dimensionality, C is the factor determined by n (C=2, π, and $4\pi/3$ for n=1, 2, and 3, respectively), τ is the time when the domain originates, and r_c is the radius of a nucleus. If point P is the switched volume at time t, the probability of no nucleus formed in volume S is given by

$$1 - R(\tau)S\Delta\tau \tag{3.13}$$

where $R(\tau)$ is the probability of nucleation per unit volume per unit time. Hence, the probability of P not included in the switched area is

$$Q(t) = exp[-\int_0^t R(\tau)S(t,\tau)d\tau]$$
$$= exp(-A). \tag{3.14}$$

And the probability of the switched volume $q(t)$ is given as

$$q(t) = 1 - Q(t) = 1 - exp(-A), \tag{3.15}$$

where A is the Avrami extended volume.

Transients fitting

Using the expressions from the K-A theory, the current, which describes the ferroelectric switching, can be found from the derivative of q(t). This can be written as

$$i(t) = 2P_s\frac{dq(t)}{dt}, \tag{3.16}$$

, and therefore,

$$i(t) = (2P_sAn/t_0)(t/t_0)^{n-1}exp[-(t/t_0)^n], \tag{3.17}$$

where P_s is spontaneous polarization, A is capacitor area, t_0 is characteristic switching time, and n is dimensionality. [15, 19] This is a well-known expression and frequently referred to in the literatures. The theoretical calculation of a transient from equation 3.17 was plotted against the experimental results for micron and submicron capacitors (21.5, 7.74, 0.69, and 0.19 μm^2). These are shown in Fig. 3.18 for the micron size capacitors, and Fig. 3.19 for the submicron size capacitors, respectively.

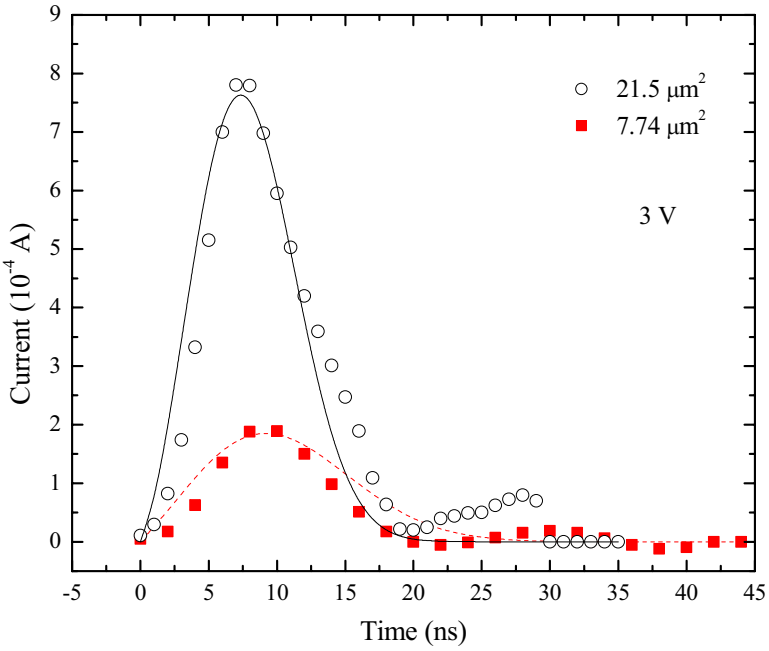

Figure 3.18: Comparison between experimental result and switching model for micron capacitors at 3 V where the dots represent the experimental results, and the lines the switching model.

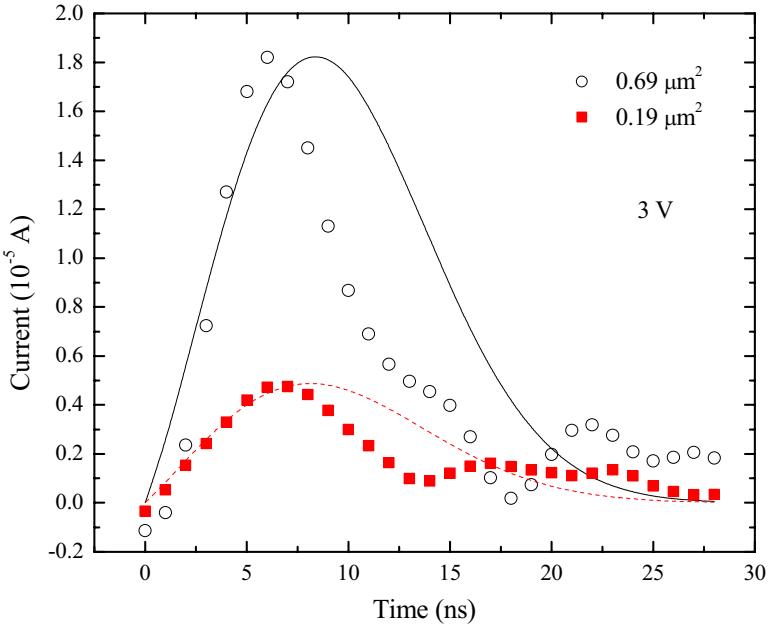

Figure 3.19: Comparison between experimental result and switching model for submicron capacitors at 3 V where the dots represent the experimental results, and the lines the switching model.

Here, the comparison was done at 3 V where the dots represent the experimental results, and the lines the switching model. The model fitting was adjusted to fit the experimental results by varying the dimensionality n, and the characteristic time t_0. Note: n and t_0 are the intrinsic properties. From Fig.3.18, and Fig. 3.19, it can be seen that there was good agreement between the experimental results, and the theoretical prediction for the micron capacitors but not for the submicron capacitors. The Ishibashi's model failed to describe the decaying part of the submicron capacitors. This was because the model did not take into the account of the circuit effect.

Intrinsic parameters ($i_m t_m/\triangle P$)

According to Ishibashi, the intrinsic behavior, could also be determined from the term $i_m t_m/\triangle P$ where i_m and t_m correspond to the maximum current (peak current transient) and the time (at maximum current), respectively. The value of $i_m t_m/\triangle P$ can describe the type of nucleation. The theoretical value of this term can be calculated from the following expressions. It is divided into two categories depending on the type of nucleation. [15]

Category I: Constant nucleation rate

$$i_{max} t_{max}/P_s = \frac{2n}{1+u} exp\left[\frac{n}{n+1}\{(\frac{u}{1+u})^{n+1} - 1\}\right], \tag{3.18}$$

Category II: Latent nuclei, no further nucleation

$$i_{max} t_{max}/P_s = \frac{2(n-1)}{1+u} exp(-\frac{n-1}{n}), \tag{3.19}$$

where n is the dimensionality and $u = t_0/t_m$. [15, 19, 22, 48] The values of the switching parameters such as i_m, t_m, t_0, n, and $\triangle P$ of the capacitors are summarized in Table 3.1. Table 3.1 also shows calculated values $i_m t_m/\triangle P$ obtained from the experimental results.

Capacitors (μm^2)	i_m (10^3 A/cm^2)	t_m (ns)	$\triangle P$ (μC/cm^2)	$i_m t_m/\triangle P$
21.5	3.56	13.8	30.55	1.61
7.74	2.57	18.1	24.57	1.89
0.69	2.57	12.8	22.65	1.46
0.19	2.48	13.7	26.63	1.28

Table 3.1: Summary of the switching parameters obtained from the switching transients of 21.5, 7.74, 0.69, and 0.19 μm^2 capacitors taken at 3V.

The magnitude of these values is in the same range and agrees with the study by Scott *et al*. which varies in between 1 and 2. [22] Ideally, $i_m t_m/\triangle P$ was expected to be a constant which only varies for different ferroelectrics, and not size dependent. However, from the results, it was also observed that $i_m t_m/\triangle P$ decreases as a function of the capacitor areas. For example, the values of $i_m t_m/\triangle P$ decreased from 1.61 to 1.28 as the capacitors were scaled down from 21.5 μm^2 to 0.19 μm^2. The $i_m t_m/\triangle P$ term is an intrinsic property. This could imply that there are size effects associated with the scaling i.e. there was a change in the nucleation and growth mechanism as a function of scaling.

As a comparison to the theoretical prediction, the values of n and t_0 obtained from the transient fitting were substituted into the equations 3.18 and 3.19, and the theoretical values of $i_m t_m/\triangle P$ were calculated. They are summarized in Table 3.2

By comparing the experimental values in Table 3.1, and the theoretical values in Table 3.2, it was concluded that experimental values lay closer to Category I. This indicates that the nucleation occurs at a constant rate.

Capacitors (μm^2)	t_0 (ns)	n	Category I	Category II
21.5	9	2.5	1.52	1.00
7.74	12	2.2	1.38	0.84
0.69	11	2.2	1.26	0.75
0.19	11	2.1	1.25	0.72

Table 3.2: Theoretical values of $i_m t_m / \triangle P$ of 21.5, 7.74, 0.69, and 0.19 μm^2 capacitors at 3V.

3.5.2 Shur model

Shur proposed a modification to the K-A theory. Shur, arguing that in reality, the dimensionality n, obtained from experimental results, is often non-integer. Therefore, the assumption of using the integer in the K-A theory is not practically appropriate. In addition, the work by Tanagerv, Shur, and Omura stated that the Ishibashi model was unrealistic and too simple to be applied to actual memory operations because only two states, an initial and a stable final state, were considered, but the intermediate state, likely to occur in the domain walls, was not taken into account.[49]

The key feature of the Shur model was the division of a current transient into smaller segments, I and II, where the dimensionality of segment I must be greater than segment II by one i.e. we can either have 3D and 2D, or 2D and 1D in I and II (see Fig. 3.20). The time where the dimensionality changed is called the catastrophe time t_c. Shur modified the K-A expression of the probability by adding the term (1-t/t_m), and thus, the α model becomes

$$q(t) = exp[-(t/t_0)^{n+1}(1 - t/t_m)], \tag{3.20}$$

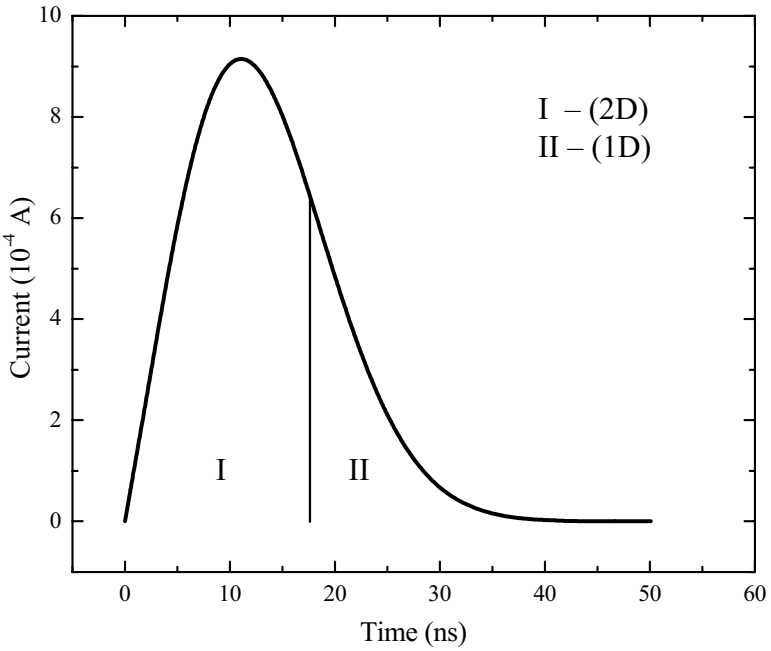

Figure 3.20: Current transient in Shur model is divided into segments I and II where the dimensionality of segment I must be greater than segment II by one i.e. we can either have 3D and 2D, or 2D and 1D in I and II.

and the β model becomes

$$q(t) = exp[-(t/t_0)^n(1 - t/t_m)], \tag{3.21}$$

where t_m is the impingement time. The impingement time is the time constant that accounts for the impingement of growing domains (individual transformed regions) on the boundary of the media i.e. the domains touch the edge of the sample. Note that t_m must be greater than t in order for the Shur model to be valid. In our study, the value of t_m was unknown, and obtained from the fitting of the transient by varying t_m, n, and t_0. The magnitude of t_m was found to be in the range of 100 ns in agreement with the data published by Shur. [21, 50–54] From the probability expression, the Shur expressions for the

α model can be expressed as

$$i(t) = (2P_s Ant^n/t_0^{n+1}\{1 - [1 + 1/(n+1)]t/t_m\}$$
$$\times exp[-(t/t_0)^{n+1}(1 - t/t_m)], \tag{3.22}$$

and for the β model as

$$i(t) = (2P_s Ant^{n-1}/t_0^n)[1 - (1 + 1/n)t/t_m]$$
$$\times exp[-(t/t_0)^n(1 - t/t_m)]. \tag{3.23}$$

According to Shur, the α model is used for the anisotropic growth whereas the β model is used for isotropic growth. Also, it should be pointed out that the time scales in the Shur experiment are much longer than Ishibashi. In several papers published by Shur, the β model was used to treat the fitting of an epitaxial film. In my experiment, it was found that the data was best fitted with the α model indicating that the domain growth was anisotropic. The result of fitting the submicron capacitor using the Shur model is shown in Fig.3.21. From the results, it can be seen that the Shur model fitted the experimental data very well which could indicate that the change in the dimensionality could occur in the submicron capacitors.

3.5.3 Ishibashi-Merz-Shur model

Another alternative of determining n and t_0 was to carrying the fitting in terms of fraction switching (normalized current). This type of fitting is also popular, as shown in the publication by Li, because it included the two extra terms describing the intrinsic and the experimental properties, activation field (α) and electric field (E), which Ishibashi did not

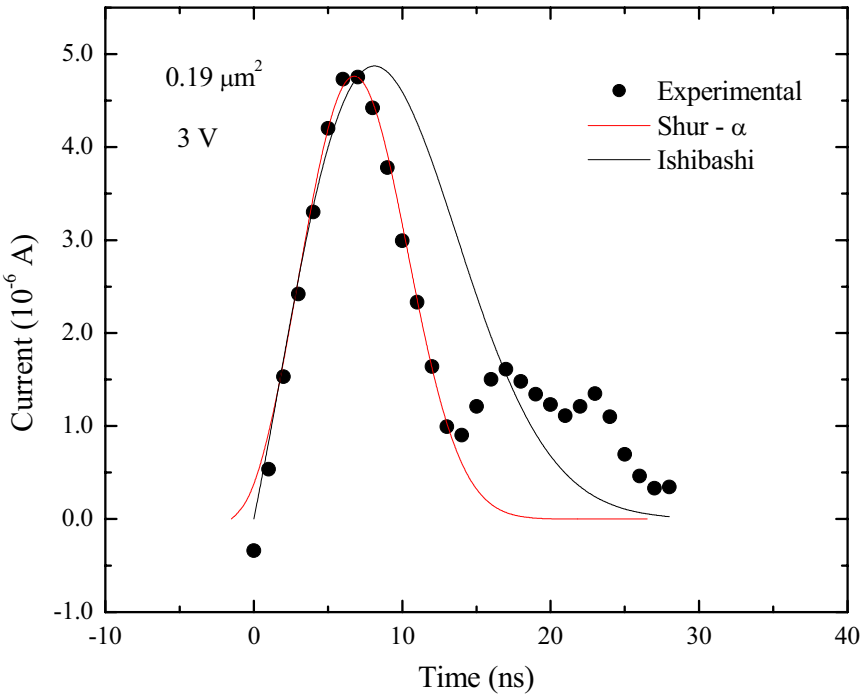

Figure 3.21: Comparison between experimental result and Shur's switching model for submicron capacitors.

take into the account. [32] Here, the displacement current, $\triangle i(t)$, related to the switching process can be expressed as

$$\triangle i(t) = \frac{V(t)}{R}. \tag{3.24}$$

Integrating the current transient gives the switching polarization,

$$\triangle P(t) = \frac{i(t)dt}{A}, \tag{3.25}$$

where A is the capacitor's area. The fraction switching, $f(t)$, can be expressed as

$$f(t) = f(switched) = \frac{\triangle P(t)}{P_{total}} \tag{3.26}$$

Or simply, f(t) is the normalization of $\triangle P(t)$.

Figure 3.22 shows the normalized polarization of 7.74 μm^2 capacitor, and Fig. 3.23 shows the normalized polarization of 0.19 μm^2 capacitor. The normalized polarization is

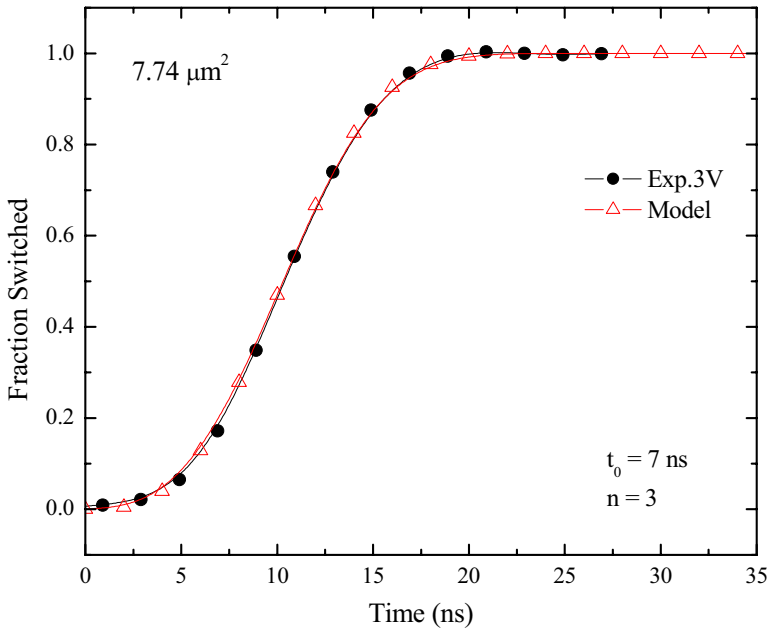

Figure 3.22: Normalized polarization, experimental results vs. Ishibashi-Merz model fitting, of 7.74 μm^2 capacitor.

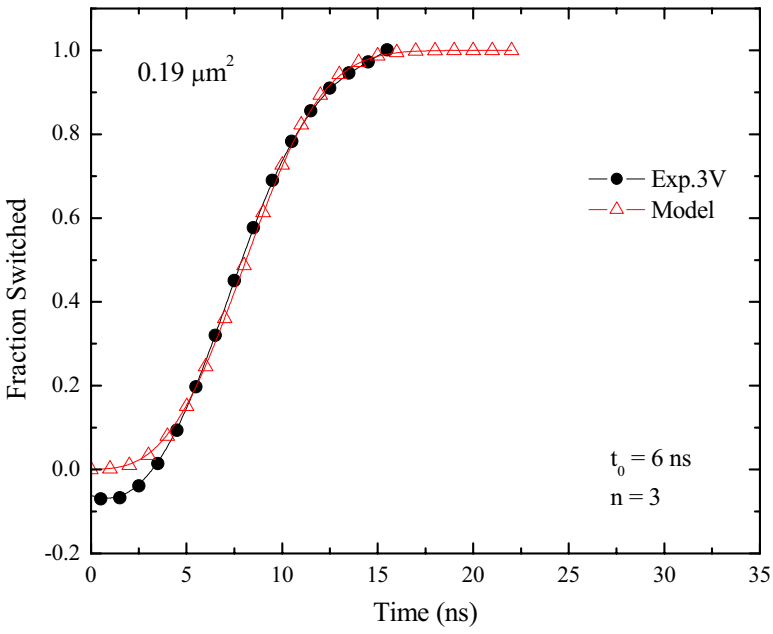

Figure 3.23: Normalized polarization, experimental results vs. Ishibashi-Merz model fitting, of 0.19 μm^2 capacitor.

given by the Ishibashi-Merz model, and can be expressed as

$$f(t) = 1 - exp[-exp(-\frac{\alpha}{E})(\frac{t}{t_0})^n] \tag{3.27}$$

where α is the activation field. This expression has the combination of both experimental and theoretical parameters. The original expression by Merz did not consider the experimental parameter i.e. the electric field. By combining the two expressions, the fraction switching becomes more meaningful. By fitting the experimental data with the model, we can extract t_0 and n which are the parameters related to the intrinsic switching properties. In addition, the Ishibashi-Merz model can be modified by combining to with Shur's model by adding the impingement time correction to give

$$f(t) = 1 - exp[-exp(-\frac{\alpha}{E})(\frac{t}{t_0})^n(1 - \frac{t}{t_m})]. \tag{3.28}$$

It should be remembered that the value of dimensionality (n), which represents types of nucleation and growth, used in the fitting should be an integer (n=1, 2, and 3) to give more meaningful results even though it was possible to use n as a fraction, i.e. n=1.1, 1.2, 1.3..., to get a better fitting, and round up the value of n to the nearest integer afterwards. [32] It was found that graph fittings, and the values of t_m and n obtaining from Ishibashi-Merz and Ishibashi-Merz-Shur models were the same. The addition of the impingement time t_m played an insignificant role. Table 3.3 shows the values of t_0 and n as function of the capacitor areas. From Table 3.3, it can be seen that the values of t_0 and n for the micron capacitors 49, 21.5, 7.74 μm^2 are constant, which indicates that there was no change in the intrinsic properties in this regime. However, it can be seen that these values are not constant for 225, 0.69, and 0.19 μm^2 indicating that the measurements were convoluted by the RC time constant. For example, the value of t_0 is greater for 225 μm^2 because

Capacitors (μm^2)	t_0 (ns)	n
225	11	2
49	7	3
21.5	6	3
7.74	7	3
0.69	3.5	2
0.19	7	3

Table 3.3: Theoretical values of t_0 and n obtained from the Ishibashi-Merz fraction switching curves of 21.5, 7.74, 0.69, and 0.19 μm^2 capacitors at 3V.

of a larger capacitance but lower for 0.69 μm^2. However, the value of the 0.19 μm^2 capacitor did not deviate. This was because the measurement itself was convoluted by noise. Otherwise, the value of t_0 was expected to be lower for the 0.19 μm^2 capacitor.

Considering the measurement error to be due to circuit effects, it can be concluded that the dimensionality did not change as a function capacitor scaling, and the characteristic time, an intrinsic property, decreased due to the circuit convolution.

Figure 3.24 shows the plot of characteristic switching time (t_0) vs. capacitor areas obtaining from the Ishibashi-Merz model (equation 3.17). Generally, it can be seen that t_0 was decreasing as the capacitor areas were reduced. This was because Ishibashi-Merz includes the activation fields (α) which were convoluted by the measuring circuits. In a later section which discusses activation fields, it will be shown that the activation field was also decreasing as a function of capacitor areas. It is very interesting to note that the t_0 values obtained from the Ishibashi model alone (equation 3.17) without consideration of α and E shows a constant value of $t_0 \sim 11$ ns.

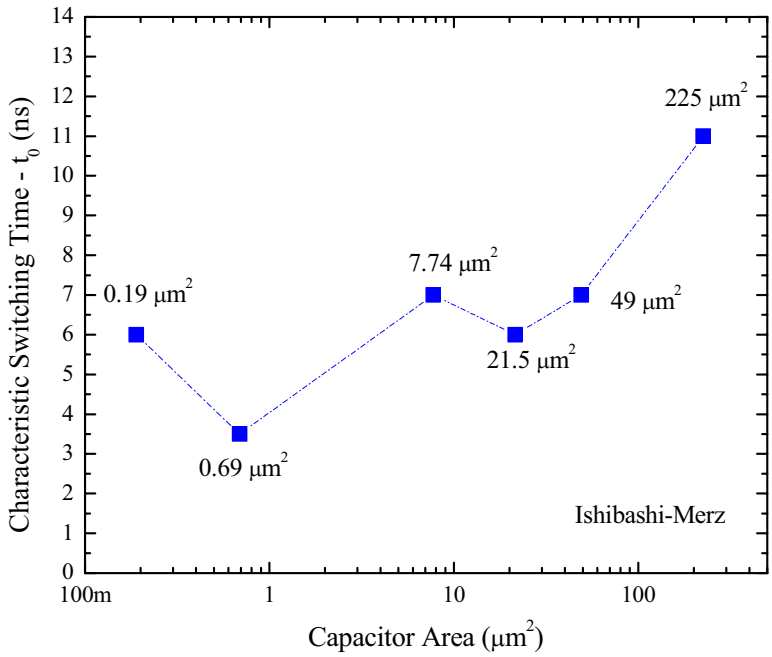

Figure 3.24: Characteristic switching time plotted as a function of capacitor areas obtained from the Ishibashi-Merz model.

3.5.4 Switching time

Another interesting aspect of the switching studies of the submicron capacitor was the determination of the switching time. There are two types of switching time, t_s and t_0, and one should not be confused with another. t_s is the switching time of a switching transient which measures the time of 90% switch completion which depends on the RC time constant of a capacitor and the measuring circuit; whereas t_0 is the characteristic switching time which is an intrinsic property and should not be affected by circuit parameters. Knowing switching speed could greatly improve the performance, efficiency, and capability of the ferroelectric memories. Currently, from the theoretical calculation, the switching time was expected to be in the tens of pico seconds range. The intrinsic switching time can be approximated from the equation

$$t_0 = \left[\frac{3}{2N_0V_\infty^2R_0}\right]^{1/3} \tag{3.29}$$

where V_∞=maximum domain wall velocity$\sim$4000 m/s, R_0=rate of nucleation$\sim 10^8$/cm^2. [1, 55] From the equation, t_0 was calculated to be $\sim$100 ps. Note: Values of R_0, N_0, and V_∞ have not been determined for thin films. [56] The only possible way of measuring was to employ switching equipment such as "Opto-Switching" used by Li to carry out the experiment. [32] However, the obstacle which prevented Li from measuring the intrinsic switching time was the large RC time constant of the micron size ferroelectric capacitor. In Li's experimental setup, only the micron size capacitors could be used. The smallest size measured, shown in the publication, was 4.5$\times$4.5 μm^2. As shown in Li's experimental results, the measurements were still convoluted by the RC time constant. However, the work illustrated the fastest switching time of a ferroelectric capacitors ever measured where t_s and t_0 were found to be 220 ps and 68 ps, respectively. Therefore, for a future improvement, it is important that we can combine the AFM setup with the opto switching experiment to allow us to measure the intrinsic switching time.

The early studies to determine the switching time were carried out by Merz. [7] These studies indicated that the switching time depends on the reversal of ferroelectric domains which was close to the speed of sound of approximately 4000 m/s. However, it was difficult to determine this quantity experimentally because the time resolution in the experimental setup was limited by the RC time constant. The RC time constant (in seconds) can be defined as the product of the circuit resistance (in Ohms) and the circuit capacitance (in Farads). It is the time required to charge the capacitor, through the resistor, to 63.2 percent of full charge; or to discharge it to 36.8 percent of its initial voltage. The RC time constant contains a contribution of capacitance from ferroelectric capacitors, and equipment setup. Hence, to minimize the RC time constant, it is desirable to use fer-

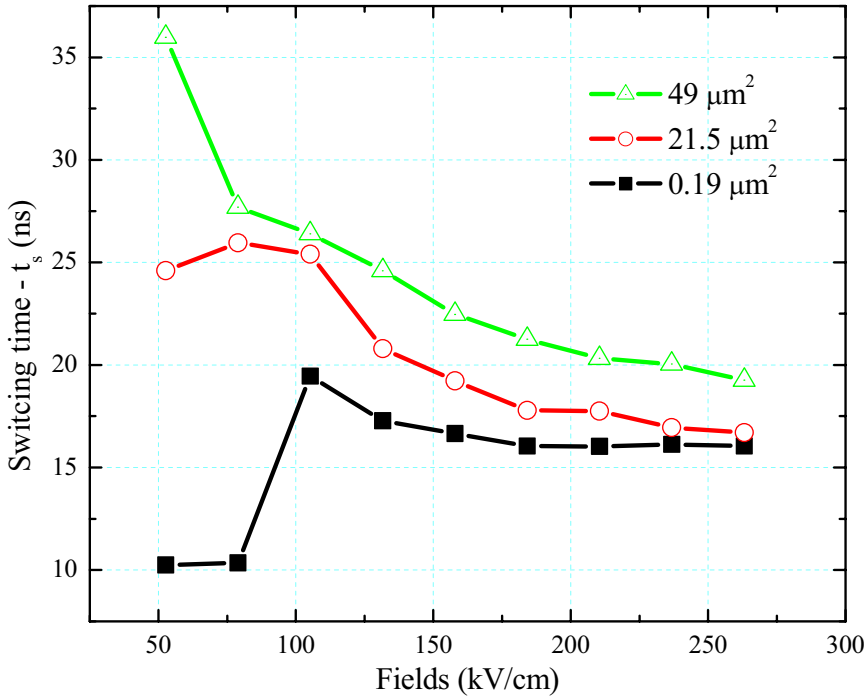

Figure 3.25: Switching time versus fields as a function of capacitor size.

roelectric capacitors that are as small as possible. Merz also indicated that the switching process depends on intrinsic factors such as the types of domains, and their mechanisms, and the extrinsic factors such as fields, and temperatures, all of which contribute to the switch time. Figure 3.25 shows how the switching time changes as a function of applied field of 49, 21.5, 0.19 μm^2 capacitors obtaining from the switching transient of voltage versus time. It can be seen that these capacitors switched at the same field of approximately 75-100 kV/cm (observed from the deflection on the graph).

Figure 3.26 shows that the switching time decreases as a function of the capacitor sizes. From theoretical studies, the magnitude of the switching time was expected to be in the pico seconds range. From the experimental results, the switching time decreased with decreasing area towards a constant value of $\sim$ 16 ns. This indicates that measurement of switching time for the submicron capacitors could be limited by the measurement setup

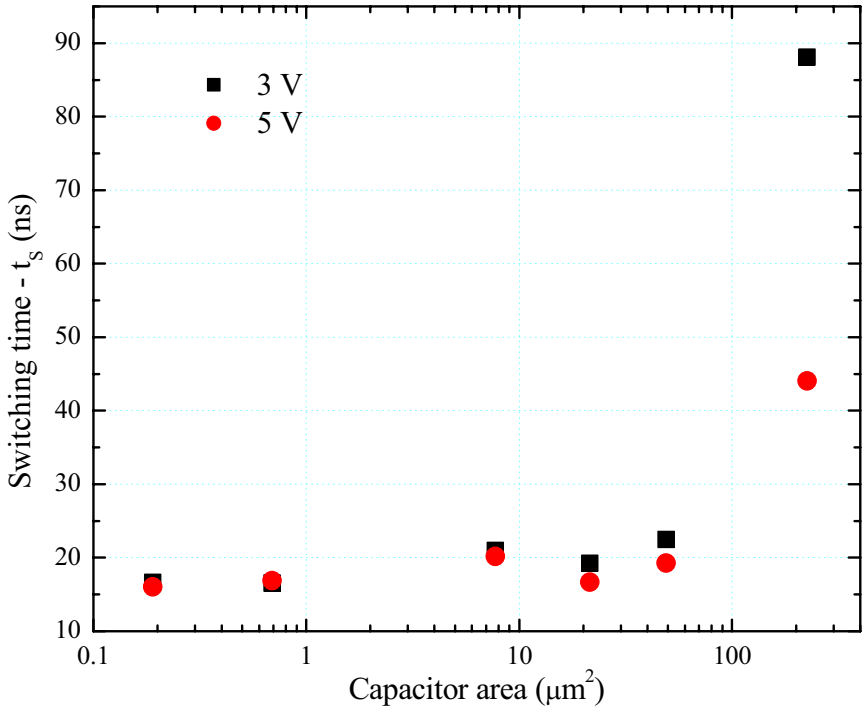

Figure 3.26: Switching time decreases as a function of capacitor areas indicating that measurements were limited by RC time constant.

RC time constant.

In Merz's study, it was found that from the linear relationship between the inverse time versus field, the activation energy could be calculated from the gradient of the graph. In addition, a distinction between the relationship at low and high fields was also observed. This agrees with Fatuzzo's proposal that there are different stages of nucleation and growth depending on the applied field. The recent publication by Kim shows the same conclusion where the different switching characteristics the low and high fields were also found. [7]

3.5.5 Activation field

The activation field describes the rate of reversal of polarization $i=dP/dt$, where i is the switching current density, and reflects the switching dynamics of the ferroelectric ma-

terial. The higher activation field implies the more resistant the domains are to switching during polarization reversal. The activation field also provides an indication of the switching performance of a ferroelectric capacitor and likewise can be used as a relative parameter to study the relationship between changes in the microstructure of the capacitor and the switching process. The parameter that most influences the activation field is the domain wall energy. Previous studies have shown that the spontaneous (or remanent) polarization is proportional to the square root of the spontaneous strain, or $P \propto z^{1/2}$. It has also been indicated that $\alpha \sim w(c/a-1)^{7/2}/(kT)$, where the tetragonality is shown to significantly impact the activation field. [1]

By studying the switching kinetics, it is possible to determine the type of domain switching process that was taking place during the polarization reversal. [19] Switching properties such as maximum current and switching time depended on the capacitor area and measuring circuit elements, but the activation field was independent of capacitor area and measuring circuit parameters. The activation field has the same unit as the coercive field. It could be determined i) as function of load resistance, ii) as function of capacitor area. In this thesis, the activation field was determined from the capacitor area dependence. The activation could be calculated using Merz's equation. If plotting $\log(i_{max}/\mathrm{A})$ vs. 1/E, the slope of the linear fits in the figure yields the activation field (α)[Fig.3.27]. Figure 3.28 summarizes the activation fields as a function of the capacitor area. It can be seen that the experimental data points were not aligned as a straight line as expected because the measurement results were convoluted by the circuit. The activation model did not account for the circuit effects. Generally, if we draw a straight fitted line to find the activation fields, it can be observed that there is a significant drop of activation fields as

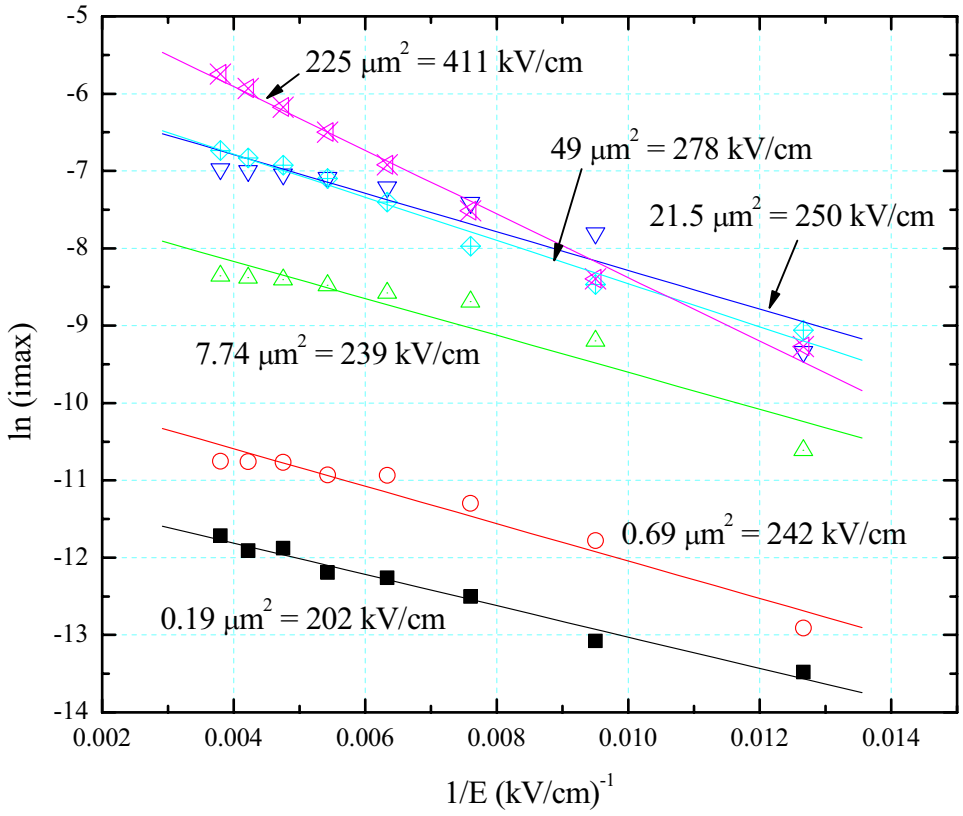

Figure 3.27: Plot of log(i_{max}/A) vs. 1/E (a) as function of capacitor area.

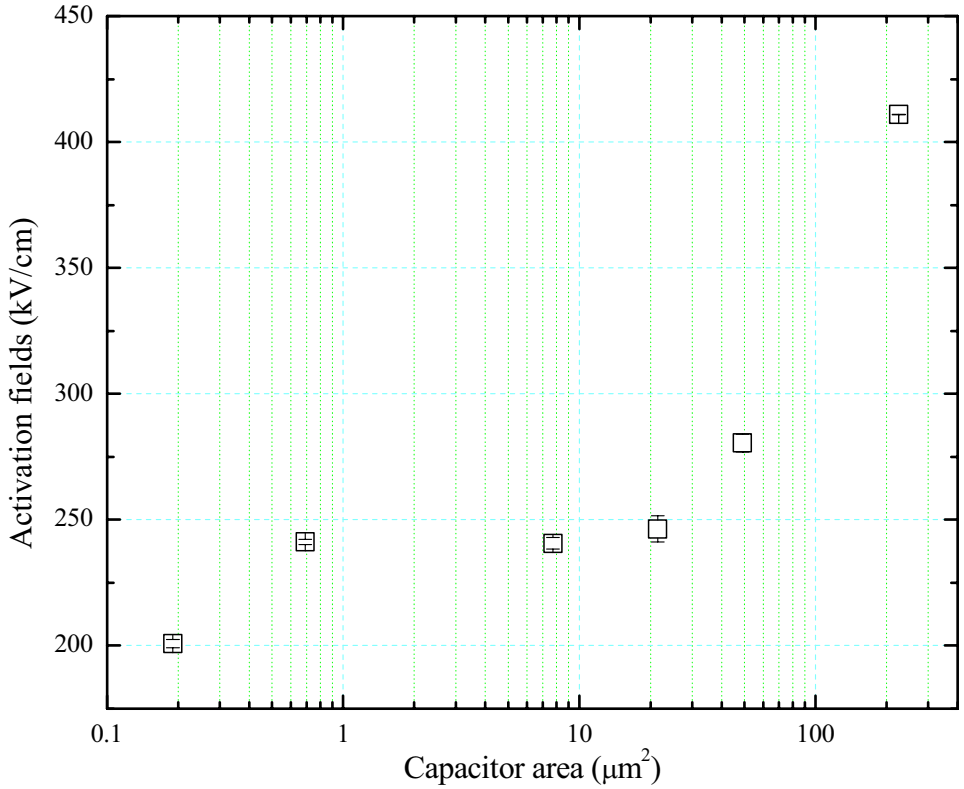

Figure 3.28: Plot of activation fields as a function of capacitor area from micron to submicron range.

the capacitor area decreases in the submicron region. This indicates changes in the intrinsic properties, and hence, there is the size effect as function of scaling. Theoretically, the activation fields are independent of the capacitor areas. Recently, Song *et al*. have shown the same finding. However, those calculations were done for the micron area capacitors, and not submicron capacitors as in this research study. The magnitude of the activation field calculated in Song's paper was approximately 300 kV/cm which agrees with my experimental results.[57]

3.6 Further Discussions

The most common cause of size effects was a decrease in ferroelectric properties due to the sidewall damage of a capacitor. [27] The variation in the ferroelectric properties could be mapped out by using the piezoelectric imaging technique. A typical size effect was the deviation of ferroelectric properties (typically the degradation of properties) caused by lateral damages of capacitors edges from fabrication such as etching which caused non-uniformity on the capacitor edges. Stolichnov *et al.* shows that a preferential polarization state observed in very small ferroelectric capacitors with 100×100 nm^2 size could affect the polarization, and that this phenomenon is explained by the accumulation of defects on the lateral surface.[30]

Theoretical studies on size effects estimated the minimum volume at which the polarization and the ferroelectric properties vanish (critical volume) to be about 1000 nm^3.[58] In lateral scaling, the number of switching charges per unit area are expected to remain for all capacitor sizes, and there is no size effect expected in terms of the switching polarization ($\triangle P$). However, the piezoelectric measurement of d_{33} has shown that the scaling behavior of submicron capacitors is possible from clamping and unclamping between a film and a substrate. This can give a large increase of the d_{33} value as the capacitor area decreased.[25]

From the literature, research on lateral scaling have been mostly experimental where the piezoelectric response measurements were commonly used in these studies. In these measurements, the switching behavior was observed through piezoelectric imaging or hysteresis. These studies show that abnormal behavior of switching at small nanometer

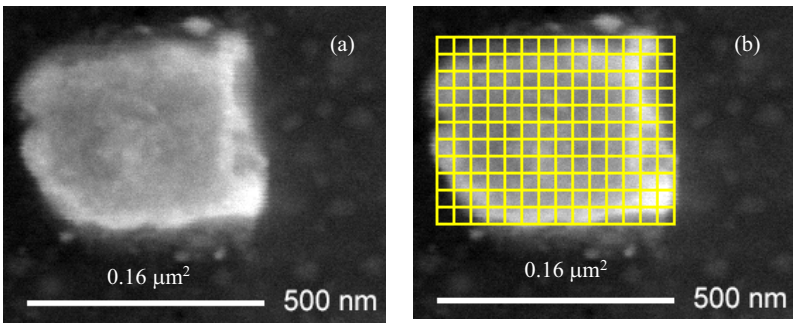

Figure 3.29: SEM image of submicron capacitor of 0.16 μm^2 as received (a) and with grid count (b).

scales could be induced by the clamping effect. Gruverman *et al*. had considered the d_{33} measurement as an indirect method, and experimental d_{33} values measured were converted into polarization. [40] through the relationship:

$$d_{33} = 2Q\varepsilon_{33}P, \tag{3.30}$$

where Q is the electrostrictive coefficient, and ε_{33} the dielectric permittivity of the ferroelectric material. However, it should be noted that that this relationship is only valid for single crystal ferroelectric, and does not hold true in this case. Therefore, the calculated polarization values in this paper were significantly deviated from what was expected.

There has been much speculation that the most likely cause of the size effects is from damage to capacitors from processing such as etching, or simply from degradation. Figure 3.29 shows a capacitor with damage around the edge caused by degradation. As a result, the capacitor area reduced, from 0.196 to 0.156 μm^2 by 20 percent. Hence, this would produce a significant change to the $\triangle P$ value. In the paper by Tiedke, the only size effects or a variation of polarization properties were from the parasitic compensation. [26] Thus, further study would be necessary to carry out PFM experiments as a function of capacitor sizes down to the submicron region, and observe the switchability as a function

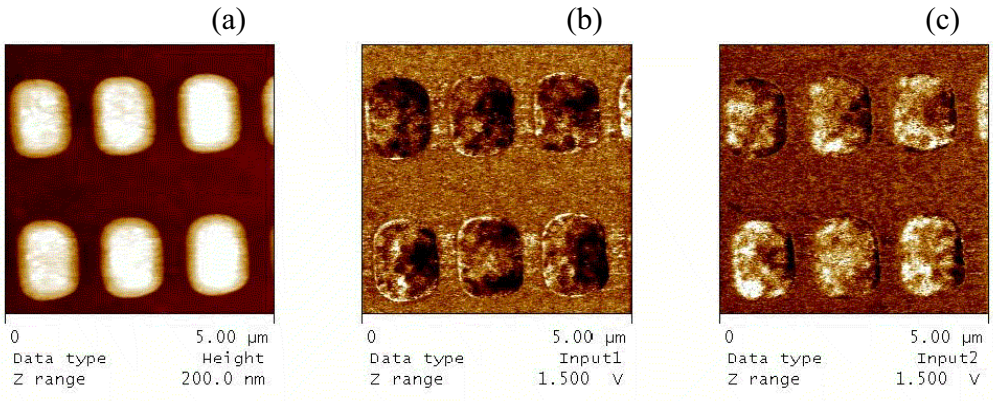

Figure 3.30: PFM images of a ferroelectric capacitor showing topography (a), d_{33} amplitude (b), and 180° phases (c).

of lateral sizes. The PFM measurements could be used qualitatively to observe the microstructure to support any findings from the quantitative polarization measurements. If the piezoelectric measurements were used, the tentative plan for the experiments would be to map out the domain structure across the capacitor area, then: i) measure the switching polarization, and ii) measure d_{33} across the top electrode area (specifically at the center and edge of the capacitor). Figure 3.30, PFM images of a ferroelectric capacitor, shows topography, d_{33} amplitude, and 180° phases. However, in this study, it must be emphasized that we are interested particularly in polarization switching. For this thesis, including piezoelectric measurements would be too wide a scope. Investigation of pulse switching would be sufficient at this point for investigating size effects.

There have been many studies on piezoelectric imaging which allowed for observation of the 180° domains. While the early studies were often carried out on samples without top electrodes [25], the most relevant experiments would be to investigate samples with top electrodes [30] so that we can observe polarization variations when the switching bipolar pulses are applied. Although the pulse switching measurements could be used

as an indicator of the size effects, it must be realized that there could be a change in the microstructure as well as the switching polarization. Thus, in addition to the pulse switching measurement, it would be useful to carry out the piezoelectric imaging experiment to investigate the size effects. From the microscopic point of view, Stolichnov *et al*. found that there is the formation of a preferential polarization state (Imprint) and non-uniform polarization across the capacitor area of 100 to 1000 nm thickness film. Switching was affected by charge injection through a surface dielectric layer. [30]

There are only a few theoretical studies on lateral and 3-dimensional behavior. One of the most interesting theoretical studies on lateral side scaling was done by Wang. [59] In his work, the phenomenological theory was used to study the correlation of the size dependence of the Curie temperature, and the polarization. Equation 3.31 shows the relationship between the Curie temperature as a function of the lateral dimensions a_0^2 and b_0^2 where D, and A are the phenomenological parameters.

$$T_c = T_{c(bulk)} - \frac{D}{A}\left[\frac{\pi^2}{a_0^2} + \frac{\pi^2}{b_0^2}\right] \tag{3.31}$$

Plotting this function shows the suppression of the polarization as function of the cell size. In Wang's study, it was found that the critical size which ferroelectricity becomes unstable for $BaTiO_3$ and $PbTiO_3$ were calculated to be 9.1 and 7.4 nm, respectively. [59]

3.7 Summary

The scaling effects of the ferroelectric capacitors, polycrystalline $PbZrTiO_3$, from micron to submicron sizes were investigated using a combination of a pulse switching setup and an atomic force microscope. The goal was to determine how the switching polarization

and the intrinsic properties change as a function of the capacitor area. In this thesis, I have studied the switching properties in terms of: i) the switching polarization ($\triangle P$), ii) the theoretical models that describe the switching transients, and iii) the intrinsic behaviors and the switching kinetics such as the switching time (t_0), dimensionality (n) of domains nucleation and growth, and the activation field (α).

1. The results show that there were no size effects in terms of the switching polarization ($\triangle P$). The switching polarization measured as a function of voltage was approximately the same for all capacitor sizes and shows no pulse width dependency. However, the intrinsic properties show peculiar results, which require better understanding and interpretation of the theoretical models and the experimental data.

2. All the properties measured rely heavily on the quality of the switching transient's shape, area, and parameters such as i_{max}, t_{max}, and t_s. The results show that the transient measurements of all the capacitor sizes were credible even for the smallest 0.19 μm^2 capacitor. The $\triangle P$ peaks were clearly visible with relatively high signal to noise (S/N) ratio. The $\triangle P$ measurements at 3 V were approximately equal to 30 μC/cm^2 for all capacitors. It must be remembered that the capacitor area measurements are very critical to the calculation of the polarization values. The effect becomes greater for the submicron capacitors.

3. This analysis, I have looked at three different theoretical models: i) Ishibashi model [15], ii) Shur model [52], and iii) Merz-Ishibashi-Shur model [32]. These models are based on the Kolmogorov-Avrami theory [16, 47], which was first

developed by Ishibashi [15] in 1971 to describe the switching transient. By fitting these models with the experimental data, the intrinsic properties such as the characteristic switching time (t_0) and the dimensionality (n) could be extracted from the curve fitting. In literature, these theories have been treated mostly on epitaxial films [22, 52, 60], and in some cases on polycrystalline film. [61] Epitaxial films were preferred because they provide an ideal system. There is nothing in these theories that precludes their being applied to the polycrystalline films. Recently, So et al. [62] showed that the K-A based theory show a better fit with the epitaxial film than the polycrystalline film. In this thesis, I attempted to use these theories to fit the transient data for polycrystalline film of discrete submicron capacitors in the nanosecond time scale.

4. From the analysis, it was found that the Ishibashi model fails to predict the behavior of submicron capacitors, and the Shur model (modification of the Ishibashi model by including the impingement time, t_m) shows an excellent fitting with the submicron capacitor data. The impingement is defined as the time taken for the domain growth to reach the boundary of the media. [60] Typically, this means the edge of a capacitor in a single crystal or a grain boundary in the polycrystal. In my polycrystalline samples, where the domain's size was expected to be the same for all capacitor sizes, t_m was expected to remain constant.

5. If we assume that a typical grain size was approximately 90 nm, using the speed of the domains growth of 4000 m/s, the impingement time is estimated to be picoseconds. However, using t_m in picoseconds would not give a good fitting for the

transients. The only way to fit the data was to assume the unrealistic value of t_m = 100 ns which is in the same magnitude as the measurement time scale.

6. The fitting using Merz-Ishibashi and Merz-Shur shows the same results. Therefore, the introduction of the impingement time had no impact after including the Merz expression into the fitting. Both Merz-Ishibashi and Merz-Shur models can fit the transient data of all capacitor sizes and yield the same values t_0 and n.

7. The finding of the characteristic time shows an interesting result. The characteristic switching time is often referred to as the intrinsic switching time or the switching time of the ferroelectric domains. [32] From thermodynamics theory, the switching time was calculated to be $\sim$ 100 ps. However, the switching time obtained from the model fitting with the experimental results was in the range of nanoseconds. This shows that a faster pulse switching setup, with the rise time comparable to the intrinsic switching time of the ferroelectric domains, in picoseconds is needed.

8. The finding of t_0 can be interpreted differently. In Li's publication, it was shown the even the fast measurement with a pulse rise time of less than 100 ps was still convoluted by the measurement circuit. The switching time measured decreases as the capacitor area decreases. Therefore, the validity of the theoretical model is questionable. Could the characteristic switching time (t_0) mean something else? To find out, the same experiment needs to be performed on the capacitors of the different compositions. If it gives the same value, this means that we were measuring the switching time of the experimental setup itself. If it gives the different value, this means that the characteristic switching time could be the material property.

9. From the fitting, it was possible to fit the n value in decimals but it was suggested that the fitting of n as an integer is more meaningful since it represents the dimensionality of n = 1, 2, and 3. In the analysis, the fitting of n in decimals has insignificant impact to the fitting.

10. Another interesting property obtained from the fitting is the dimensionality (n) of the domains growth. The results show that n varies between 2 and 3. There was no trend of n changing with the capacitor areas. However, the dimensionality of 3 was unrealistic because it is energetically unfavorable. Therefore; we expect to have the true dimensionality (n-1) of 1D and 2D in the α-model (reverse nuclei arise throughout).

11. The activation field (α) measurement shows size dependency. The results show a decrease in the activation field as the capacitor area decreases. There was a drastic drop of α from the 225 μm^2 to 49 μm^2, and from 0.69 μm^2 to 0.19 μm^2 capacitors. So what is responsible? Could this be the convolution of the experimental circuit as similar to the reduction of the switching time as a function of the capacitor size? It must be noted that the magnitude of the i_{max} was not a time dependent parameter. Therefore, the reduction of the activation could be convoluted by some other factor. From literature, researchers began to pay more attention to the interaction between the AFM tip and the sample. [63] It is possible that the AFM tip-sample interaction played a role in the drop of the activation field.

Chapter 4

Thickness scaling

4.1 Introduction

Thickness scaling of ferroelectric properties has been studied for the last three decades. The size effect in thickness scaling is a very important issue since it limits the minimum thickness that can be used in the ferroelectric applications. From the literature, most of the studies were done on PTO and BTO systems, and rarely on PZT.[64–68, 68–72] In addition, the studies were more theoretical[4, 67, 71] than experimental.[70, 73, 74] This was because of the difficulty in producing the ultra thin films with thickness less than 20 nm, and availability of measurement tools to quantitatively measure the film's properties.

The early quantitative study by pulse switching was carried out on the thick films in the micron range of 0.15-0.50 μm.[22] Other studies were mostly qualitative using x-ray diffraction, and piezoelectric imaging.[68] Even though, there were some quantitative studies with piezoelectric measurements, such measurements would be irrelevant to memory applications. Theoretical studies suggested that ferroelectricity would be suppressed due to depolarization as film thickness decreases while other studies suggested that the suppression could be caused by an intrinsic effect, such as phase instability.[66, 71]

From application point of view, it is necessary for the ferroelectric memories to maintain a large polarization even at smaller thicknesses. The important question is what

happens to the polarization at thickness levels below 100 nm which is important for memories development. There are many interesting questions in the scaling such as: i) What is the minimum thickness for a ferroelectric film before ferroelectricity suppresses and vanishes? and ii) What is the coercive behavior and the breakdown field? This thesis presents the direct polarization switching measurements of PZT thin films for thicknesses down to 4 nm (approximately 10 units cell).

4.2 Background

4.2.1 Theoretical studies

The space and polarization charge distributions and the electric fields play important roles in the properties of ferroelectric capacitors. If we consider a short-circuit condition for a ferroelectric sandwiched between two electrodes where the polarization charge is in the z-direction, and the lateral dimensions of x and y are infinite then in the case for a thin film, depolarization occurs when there is an incomplete cancelation of the space charge and polarization at the surface. This leaves a non-vanishing electric field at the film-electrode interface which has the opposite direction to the polarization of the applied field. The study by Mehta in 1973 indicates that depolarization had caused the polarization decay in ferroelectric capacitors.[5] The magnitude of depolarization also depends on the choice of electrodes. For example, the depoling field in the metallic electrode is much smaller than the semiconductor electrode due to the shorter screen length. The screening length λ is the length where the space-charge extends into the electrode. Although, it was suspected that the likely cause of the suppression came from depolarization, it was difficult to prove

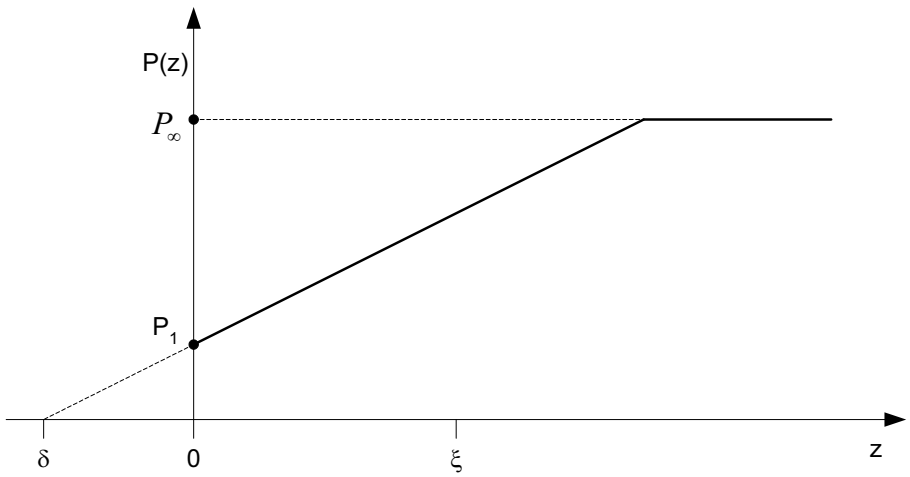

Figure 4.1: Variation of the local polarization P(z) in the vicinity of a plane free surface situated at z=0. The bulk polarization is denoted by P_∞ while P_1 denotes the polarization at the surface. δ is the so-called extrapolation length.

experimentally. Li *et al.* stated that with top electrodes, it was likely for the surface charges to be fully compensated, but without top electrodes, partial compensation could occur from the surface bending. Furthermore, the magnitude of the surface effect might be so small that the effect of the depolarization could be considered insignificant. [66]

In many recent studies, it has been postulated that ferroelectric suppression occurred from intrinsic effects. In Zembilgotov's study, the intrinsic effect was considered via the influence of the misfit strain imposed on the film lattice causing a reduction of polarization in the surface layers. Figure 4.1 shows the change of the local polarization P(z) near the plane surface z=0 where P_∞ and P_1 are the bulk and surface polarizations, respectively, and δ is the extrapolation length. [75] In Pertsev's work, the "misfit strain-temperature" phase diagrams for epitaxial $BaTiO_3$ and $PbTiO_3$ thin films were developed which show the range of a ferroelectric phase stability with spontaneous polarization parallel to the film surface. [4, 67, 76] It was shown that the ferroelectric phase's stability, hence polarization, could be altered from the strain effect. Figure 4.2 shows the phase

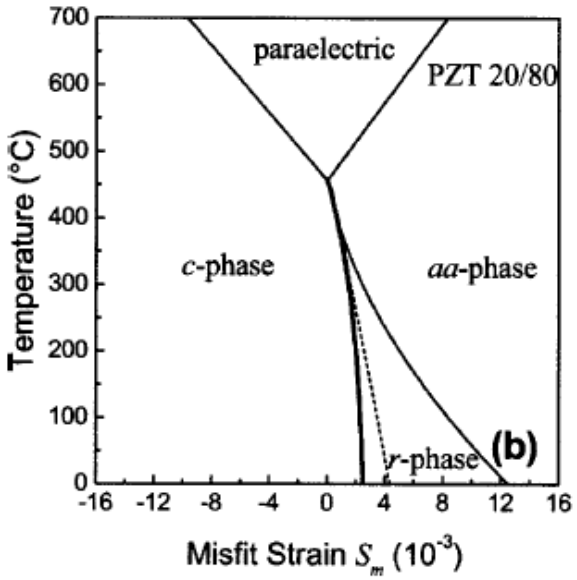

Figure 4.2: Phase diagram of PZT(20/80) epitaxial film grown on dissimilar cubic substrate. The second and first order phase transformations are shown by thin and thick lines. The quadruple point where S_m=0 is the Curie-Weiss temperature (θ). [4]

diagram of PZT(20/80) calculated as a function of strain. This phase diagram is particularly useful because in size effects calculations, the Curie temperature as a function of compressive strain may be needed. This information is often unavailable experimentally but can be obtained from this theoretical prediction.

4.2.2 Experimental studies

In the past couple of years, there have been several reports on experimental studies in thickness scaling of ferroelectrics. The most common types of experiments have been the piezoelectric measurements (mostly qualitative with only a few quantitative), polarization hysteresis, and structural measurement such as x-ray diffraction. To date, there are few publications on pulse switching measurements for film thicknesses below 10 nm. [77, 78]

Tybell *et al*. [74] used AFM with a combination of piezoelectric and electric-field

microscopy to study the time dependence of the measured signals where it reveals a stable ferroelectricity in single crystalline ($PbZr_{0.2}Ti_{0.8}O_3$)/NbSTO structure films down to 4 nm thickness. Piezoelectric measurement, which is insensitive to leakage currents, was used to measure the ferroelectricity. The results show that the piezoelectric signal detected as function of time was decaying as film thickness decreased. It was suggested that the ferroelectricity's decay was due to the misalignment and long-range electrostatic interaction of dipoles along the polarization axis. [74] Yanase *et al*. reported that a ferroelectric hysteresis could be detected in heteroepitaxial $BaTiO_3$ films as thin as 12 nm grown on $SrRuO_3$/$SrTiO_3$ (100) substrates. The study shows the polarization hysteresis measurements of thin films in the range of thickness from 80 nm to 12 nm. No polarization suppression was observed in this case. Very interestingly, the c-axis lattice constant was found to be 6 percent larger than the bulk value. Generally, T_c is expected to be suppressed as a function of decreasing thickness. This study suggests that the ferroelectric properties were maintained at small thickness because of the increase of the Curie temperature induced by the misfit strain. [70]

In another studies, Streiffer *et al*.[68] investigated the existence of 180° stripe domains as a function of thickness between 1.6 nm and 46 nm of fully strained epitaxial $PbTi0_3$ film on $SrTiO_3$ substrate. It was predicted that the film thickness of two unit cells (0.8 nm) could still exhibit ferroelectricity, and the suppression of T_c, and ferroelectricity were due to the existence of the 180° stripe domains.[68]

Apart from physical experiments, a study of thickness scaling was also carried out using computer simulation. In that recent work by Junquera and Ghosez, their first principles calculations show that the depolarizing field was responsible for the polarization

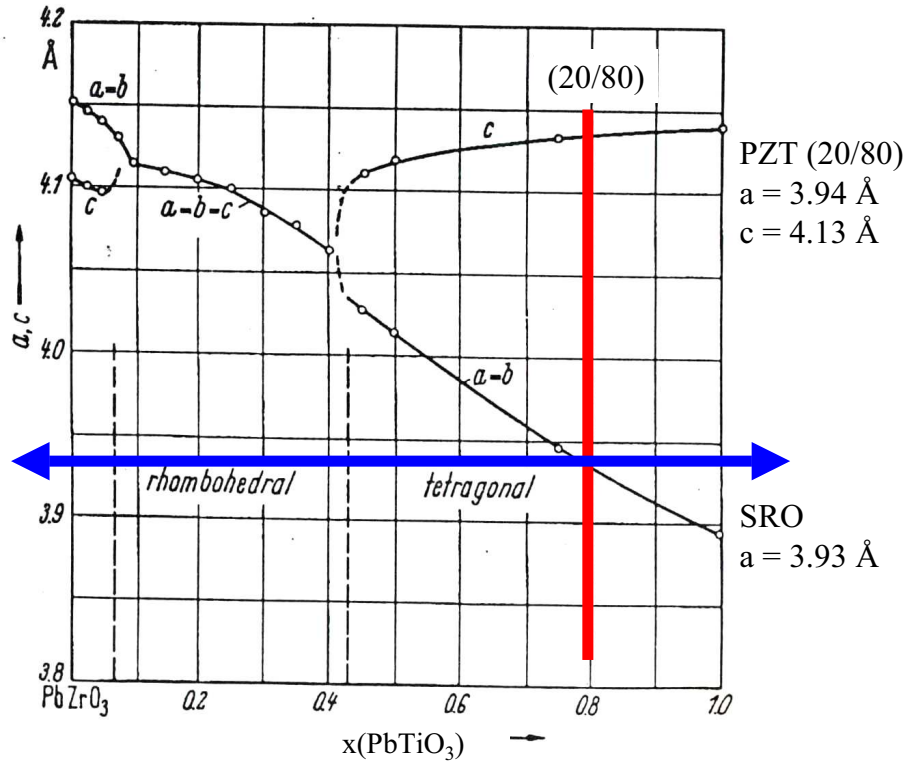

Figure 4.3: Model system (Landolt Bornstein Tables). [2]

suppression.[79]

4.3 Thin films preparation

Figure 4.3 shows the phase diagram of PZT where the vertical indicates the PZT $PbZr_{0.2}Ti_{0.8}O_3$ composition, and the horizontal line the lattice spacing of SRO. A 70-nm-thick SRO layer was grown on STO at 650 °C followed by the PZT layer via pulsed laser deposition. The deposition was carried out at 100 mTorr of oxygen and the sample was cooled down from the growth temperature at 1 atm of oxygen. The films in this study were 4 to 80 nm thick, entirely c-axis oriented, and did not have the 90° domain formation. The Radiant Technologies Precision Premier system and an AFM based pulsed probing technique with conductive PtIr tips was used to measure the

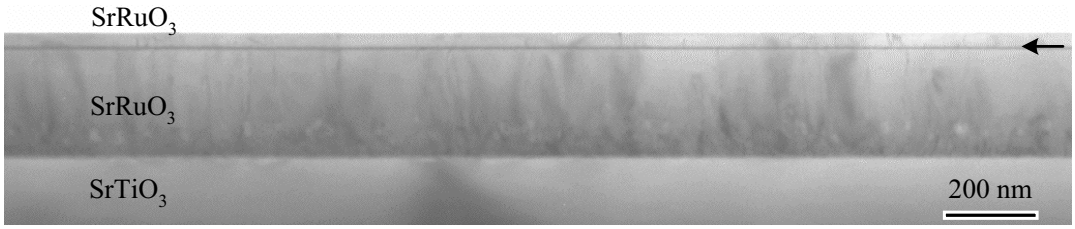

Figure 4.4: TEM image of 4 nm film.

polarization hysteresis, and the pulsed polarization, respectively. This thesis focuses on the PZT (20/80) composition which has the in-plane lattice parameter of 3.94 Å which was closely matched with the the lattice parameter of STO at 3.93 Å. The closed lattice matching reduces the number of defects, thus, the leakage currents, and provides an excellent capacitor structure for this study. According to Zimbilgotov, the misfit strain can be calculated from $S_m = (b^* - a_0)/b^*$, where b^* and a_0 are the lattice constants of the substrate and the film, respectively. [71] By substituting the values of b^* = 3.93 Å, and a_0 =3.94 Å, S_m was calculated to be -2.545$\times 10^{-3}$ m. The negative sign indicates the film is under compressive strain. Figure 4.4 shows the low magnification transmission electron microscopy (TEM) image of a cross-section of 4 nm PZT film with top and bottom $SrRuO_3$ (SRO) electrodes grown on $SrTiO_3$ (STO) substrate. The image shows a uniform PZT film sandwiched in between the SRO electrodes. In this study, we have grown the various film thicknesses between 4 nm and 80 nm.

In the experiments, it was desirable to reduce the leakage by making the capacitors as small as possible, especially for thicknesses below 10 nm. Thus, a submicron capacitor structure was needed. Hence, we employed the Focused Ion Beam (FIB) method to fabricate the submicron structures. [27] Figure 4.5 shows the switching polarization $\triangle P$ measured as a function of the pulse width for 8 nm and 15 nm capacitors at constant field.

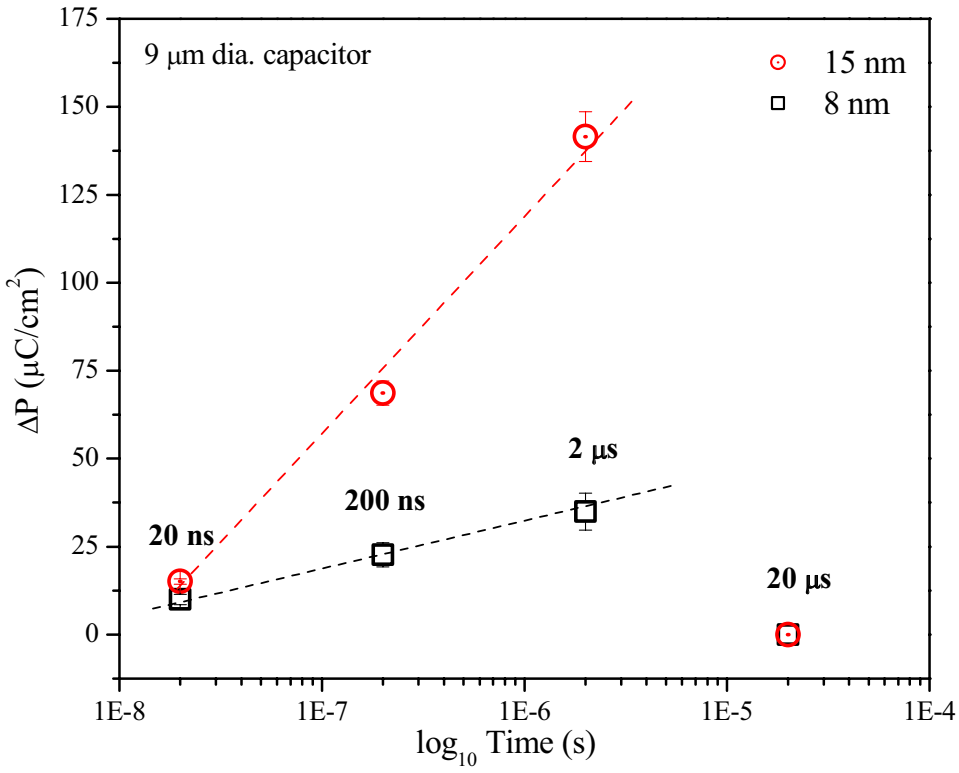

Figure 4.5: $\triangle P$ vs pulse width for 8 nm and 15 nm capacitors measured at constant field. The plot shows pulse width dependence indicating that 2 μs pulse width is the most suitable width to fully switch micron size capacitors without shorting them.

The plot shows indicates that the 2 μs pulse width is the most suitable pulse width to fully switch micron size capacitors without shorting them. Figure 4.6 shows an SEM image of the SRO/PZT/SRO structure with the capacitor area of 0.2×0.2 μm^2 of the 80 nm film fabricated by FIB, and Fig. 4.7 shows the comparison of the switching polarization of the continuous ($\triangle P$=140 μC/cm^2) vs. FIB ($\triangle P$=80 μC/cm^2) capacitors. The results show a decrease of switching polarization which indicates the degradation of the ferroelectric property after the FIB process. Additional post annealing treatment did not recover the film property. Thus, an alternative method of producing the submicron structure was needed.

Here, I developed the modified lift-off process to fabricate the submicron capacitor

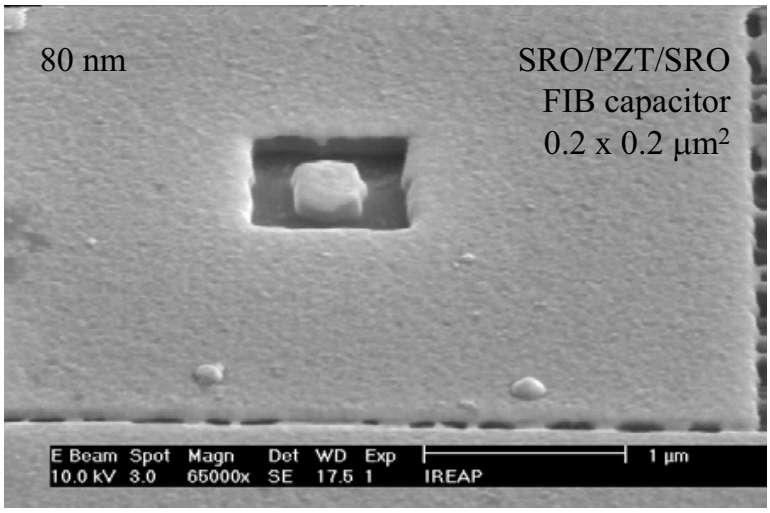

Figure 4.6: SEM image of the SRO/PZT/SRO structure with the capacitor area of 0.2×0.2 μm^2 of the 80 nm film fabricated by FIB.

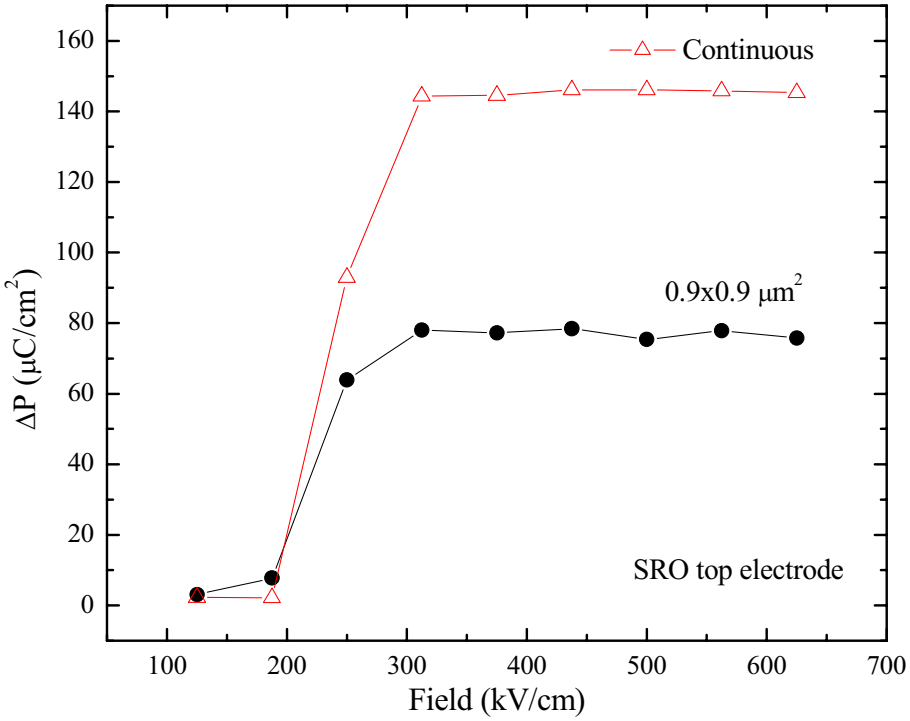

Figure 4.7: Comparison of the switching polarization of the continuous (micron size) and FIB (submicron size) capacitors.

structures where the photoresist was deliberately under developed. This reduced the short circuit paths, and also allowed the fast rise-time. This method was an excellent alternative for fabricating the submicron structure compared to the focused ion beam (FIB) process which damaged thin films of less than 10 nm thickness. However, the modified lift-off method has a limitation that it can successfully produce capacitors only with a platinum top electrode. Figure 4.8 shows a comparison of the switching polarization of the 80 nm film with SRO and Pt electrodes. It can be seen that both types of electrodes yield the same switching polarization $\triangle P$ 140 μC/cm^2. However, using the Pt top electrode increases the coercive field from 200 kV/cm to 500 kV/cm. According to Batra, the choice of electrodes will have an impact in thickness studies such as the depolarization (different screening length), and intrinsic property (suppression of Curie temperature). [80] The electrode effects as a function of thickness scaling will be proposed in future studies and will not be covered in this thesis.

Figure 4.9 shows AFM images of section analysis for the submicron capacitor from the modified lift-off method of the 4 nm thick film with a Pt top electrode. The AFM images show excellent: a) conformity (height profile) and b) uniformity (top view image) of the submicron capacitor. In these images, the red and green triangular markers shows the locations where the horizontal and the vertical distances were measured across the capacitor. From the section analysis, the horizontal distance (L), which represents the capacitor's diameter, was found to be 0.39 μm, and the vertical distance, which represents the electrode's height, as found to be 64 nm.

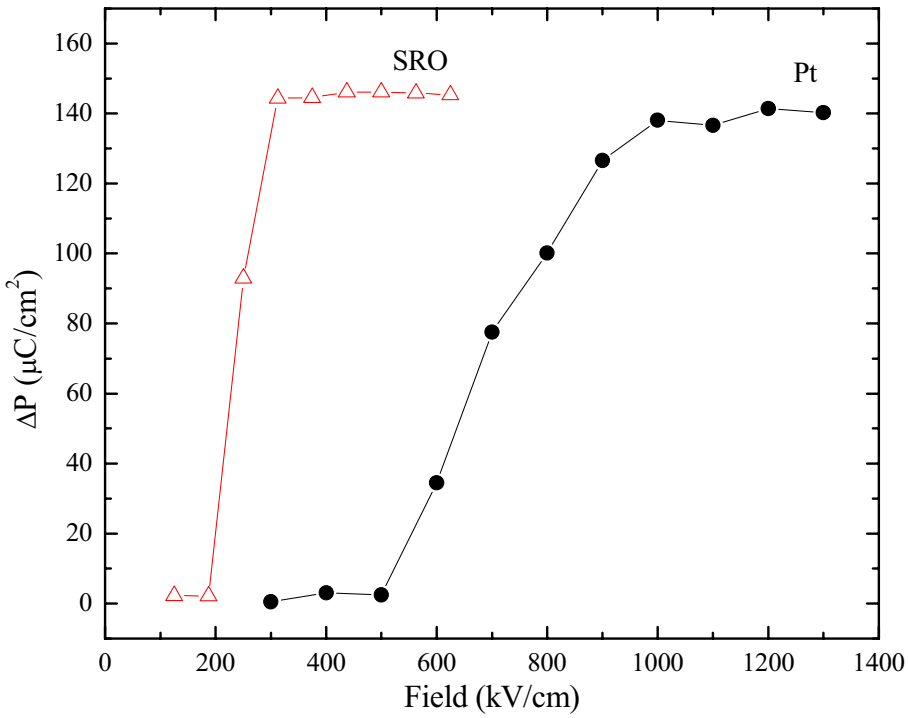

Figure 4.8: Comparison of switching polarization of 80 nm film with SRO and Pt electrodes.

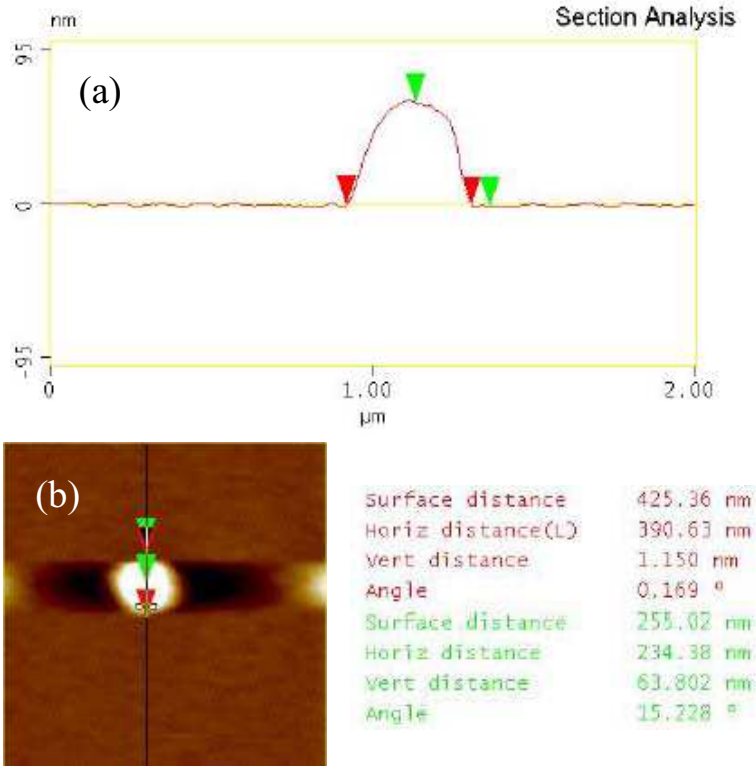

Figure 4.9: AFM section analysis images showing a) side-view, b) top view of submicron capacitor.

4.4 Results

4.4.1 Hysteresis

In the thickness scaling study it became apparent that the hysteresis measurement was not a suitable tool to study thickness scaling due to convolution of leakage current. The convolution was dependent on the frequency used. This caused a deviation of the polarization value, and the coercive fields. Ideally, the highest frequency of the triangle input pulses should be used. Figure 4.10 shows the polarization hysteresis of 160, 50, and 15 nm thin films measured at 2000 Hz. The $2P_r$ obtained for these films were approximately the same; 150 μC/cm^2. This is in a good agreement with the theoretical prediction of this film's composition under compressive strain.[4, 81] As the film thickness decreases, it can be seen that the coercive fields are progressively increasing. Attempts to measure the 10 nm thickness were unsuccessful due to the overwhelming leakage, and the results were not credible. Hence, the measurements by the pulse switching polarization were needed where they could be taken at high speed, which reduced the leakage effects.

4.4.2 Pulse switching

In the pulse switching measurements, the circular capacitors used were available in both micron and the submicron sizes ranging from 18 to 0.4 μm in diameter. In the experiments, we used two sets of the applied pulses depending on the capacitor size. The applied pulse consisted of either i) 2 μs pulse width, 2 μs pulse delay, or ii) 200 ns pulse width, 200 ns pulse delay. As a rule, the 2 μs pulse width is the minimum width required to switch the micron size capacitors. The 200 ns pulse width was sufficient to switch the

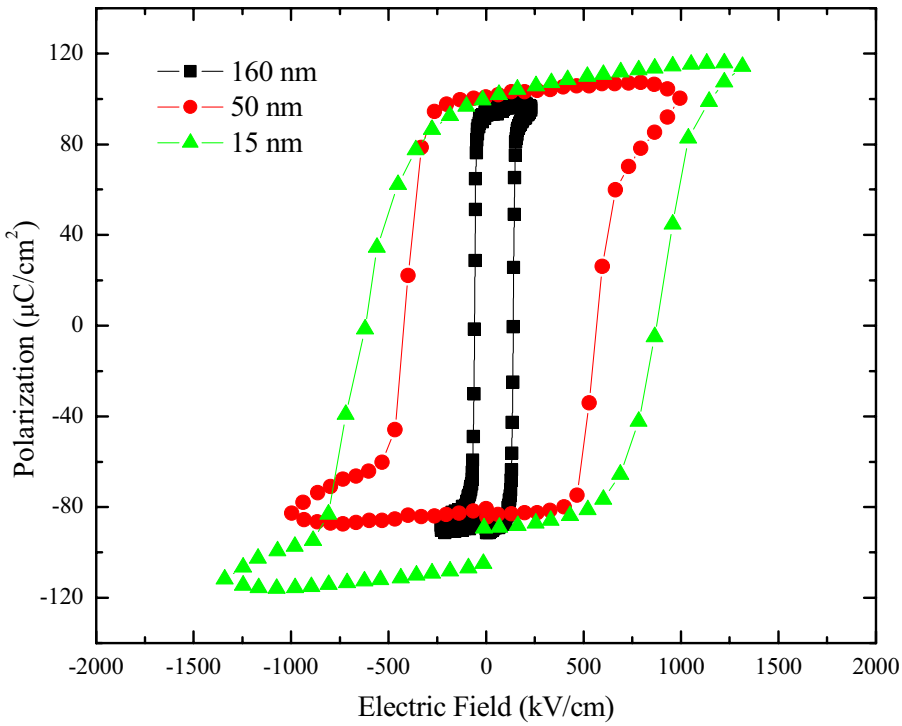

Figure 4.10: Polarization hysteresis as a function of thickness.

submicron capacitors, and the capacitors with diameters in the vicinity of 1 μm.

Figure 4.11 shows the switching transients of 15 and 8 nm at 2750 kV/cm, and 4 nm at 3250 kV/cm under the applied pulse (width) of 200 ns. These applied fields were required to obtain fully switched transients and the saturated polarization as a function of fields. The voltage of the 4 nm film is indicated by the scale on the right. It can be seen that the polarization, indicated by the area of the transients and the maximum transient's amplitude, was gradually decreasing as the film thickness was reduced. The calculated switching polarization for the 15, 8, and 4 nm films were found to be 140$\pm$3, 36$\pm$4, and 11.4$\pm$5 μm^2, respectively. The subset of Fig. 4.11 shows the transients of P^* and $P^\wedge$ indicating that their differences, hence the magnitude of the switching charge, is extremely small.

Figure 4.12 shows the switching polarization measured as a function of the applied

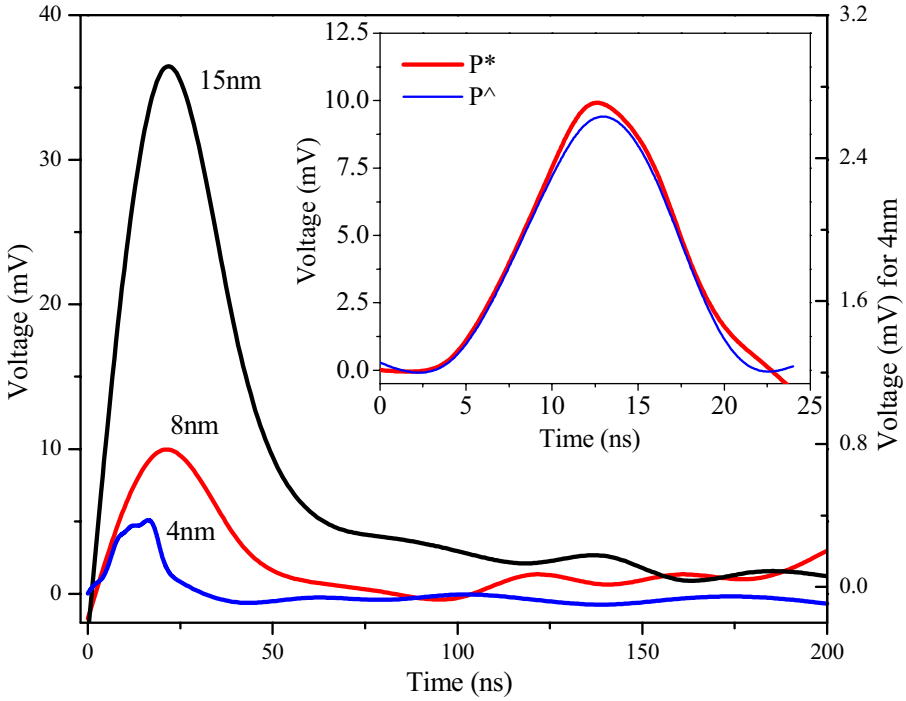

Figure 4.11: Voltage density showing suppression of the voltage signal measured from 15 nm, 8 nm, and 4 nm films. The inset shows P^* and $P^\wedge$ responses for the 4 nm thick film.

fields for the various film thicknesses. From this figure, we can extract two properties; saturated switching polarization $\triangle P$ and coercive fields E_c. These two properties are very crucial in helping us to determine the thickness scaling behavior. It should be noted that the polarization in this case is the polarization which saturates as a function of the applied fields. This represents the polarization of a fully switched capacitor. The coercive field is the field at which the polarization occurred i.e. the point where $\triangle P$ was observed, and increased from above 0 μC/cm^2. The switching polarization extracted from Fig. 4.12 was then plotted as a function of thickness, and is shown in Fig. 4.13. Here, the switching polarization obtained from the 60 μs (Radiant System) and 200 ns (AFM-pulse swtiching) pulse widths are compared. Note: The Radiant system's specifications offers the minimum pulse width of 50 μs but the actual minimum pulse width that could be used

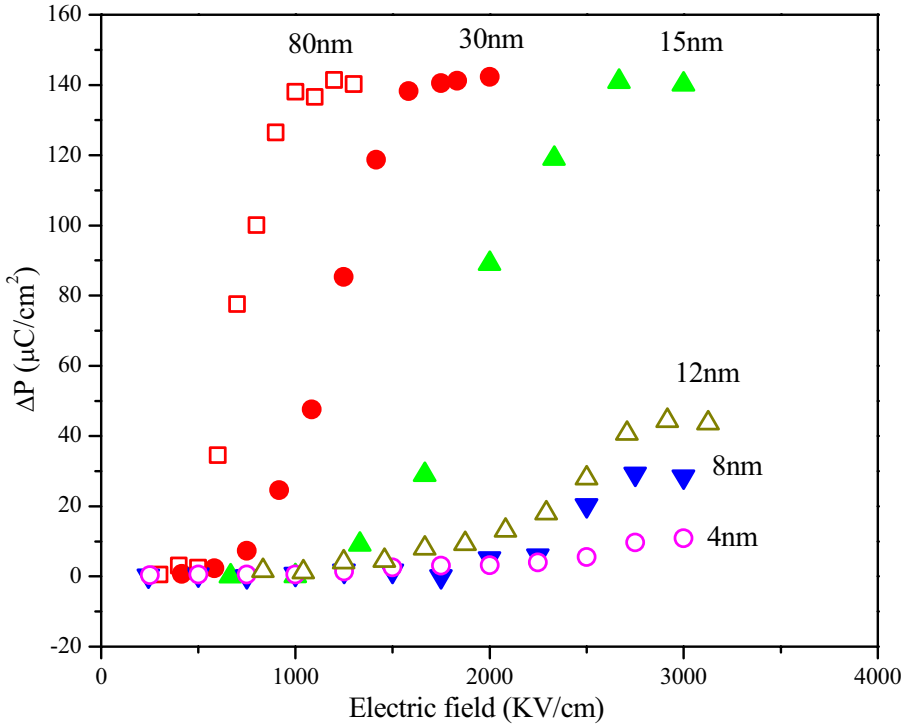

Figure 4.12: Switching polarization profile as a function of applied fields of different film thickness.

was 60 μs. According to Fig. 4.13, the 200 ns (squares) measurements show a sharper drop in polarization than the 60 μs (circles). This was observed from the larger gradient as the film decreased from 15 nm to 8 nm. For the 8 nm thickness film, the switching polarization obtained from a 200 ns pulse width was approximately 30 μC/cm^2. This was much lower than $\triangle P$ = 72 μC/cm^2 obtained from the 60 μs applied pulse. The discrepancy between the 60 μs and the 200 ns measurements could come from the fact that the 60 μs measurement was much slower than the 200 ns measurements (300 times slower), and measured from the larger capacitors (9 μm and 18 μm diameters). Therefore, it was likely that these measurements were convoluted by leakage. As a result, this would give a larger switching polarization value. The investigation of the sub 10 nm thin film needed a careful analysis of the switching transients. This could not be seen from the commer-

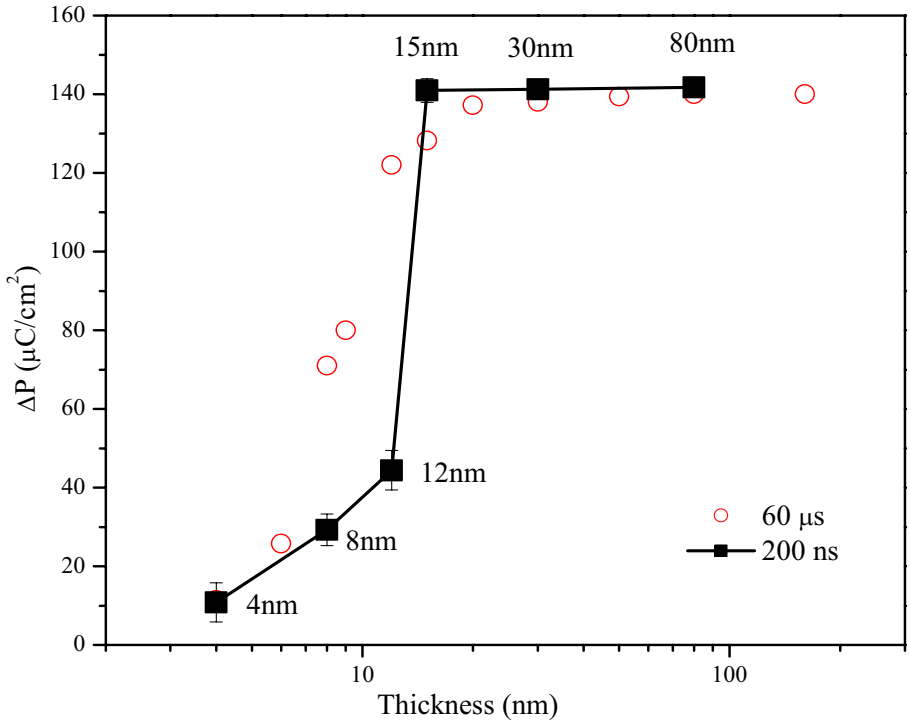

Figure 4.13: Switching polarization plotted as a function of film thickness.

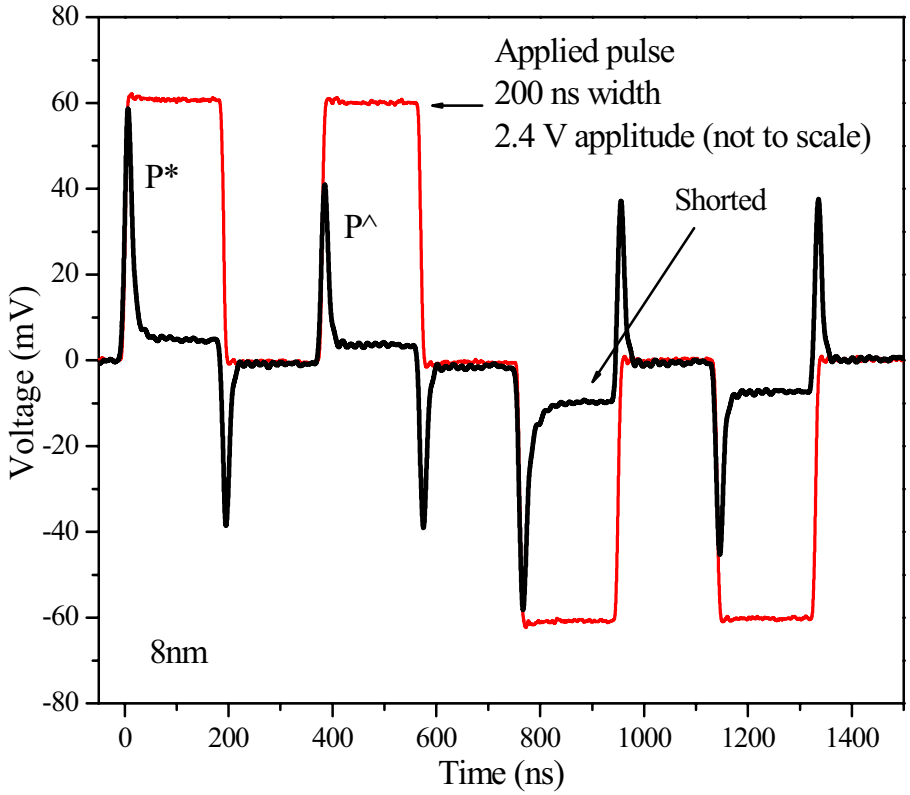

Figure 4.14: Switching transient shows a shorted capacitor of 8 nm thick film indicated by the shift of the base voltage level away from 0 V.

cial system. For example, integrating a leaky transient, shown in Fig. 4.14, of the 8 nm thick film gave higher switching polarization, and could go undetected in the commercial system. Thus, by using the AFM-pulse switching method, we were able to eliminate bad results. Thus, the results obtained from the AFM-pulse method for the sub 10 nm thick film were more accurate.

4.5 Analysis

In this section, we will consider the intrinsic and depolarization models in details. The theoretical polarization obtained from these models will be compared with the experimental results to determine the cause of suppression. Most theories, unless stated otherwise, were developed from the phenomenological theory (Landau-Ginzburg-Devonshire). Table 4.1 summarizes the data for PZT(20/80) which will be referred to often, and used in the analysis calculations.

4.5.1 Intrinsic model

There are two intrinsic models that we will consider in this section. First, the model proposed by Zembilgotov, and second, the model by Li.[66, 71] The model by Zembilgotov was developed from the Landau-type theory by considering the misfit strain, and the intrinsic surface effect.[76] The mean polarization $\bar{P}/P_s^0$ profile as function of thickness H can be found from the integral

$$\frac{\bar{P}}{P_s^0} = \frac{2\xi_0^*}{H}\int_0^{H\sqrt{1-t}/2\xi_0^*} \rho(\zeta)d\zeta \tag{4.1}$$

Type	Value
Correlation length (ξ)	2.4 nm [78]
Screening length (λ)	0.5 Å [82], 1 Å [78]
Extrapolation length (δ)	4.8 nm [66]
Dielectric stiffness (α)	-14.84$\times 10^7$ m/F [81]
Dielectric stiffness (β)	-3.050$\times 10^7$ m^5/C^{2}F [81]
Dielectric stiffness (γ)	2.475$\times 10^8$ m^9/C^{4}F [81]
Electro strictive constant ((Q_{12})	-2.446$\times 10^{-2}$ m^4/C^2 [81]
Elastic compliance (s_{11})	8.2$\times 10^{-12}$ Pa^{-1} [4]
Elastic compliance (s_{12})	-2.6$\times 10^{-12}$ Pa^{-1} [4]
Normalized coefficient (D_{11})	3$\times 10^{-15}$ [66]
Normalized coefficient (D_{44})	5$\times 10^{-16}$ [66]
Curie-Weiss temperature (θ)	460 °C [4, 81]
Curie-Weiss constant (C)	1.642$\times 10^5$ °C [81]
Dielectric constant of film (ϵ_f)	60 [78], 200 [83], 511 [84]
Dielectric constant of electrode (ϵ_e)	8 [82]
Spontaneous polarization (P_s)	70 μC/cm^2 [81], 62 μC/cm^2 [4]

Table 4.1: Summary of data for PZT(20/80) used in thickness analysis calculations.

where t is the relative temperature ($t = T/\theta^*$),ξ_0^* is the correlation length, θ^* is the Curie-Weiss temperature, and $\rho(\zeta)$ can be obtained from

$$\zeta = -\int_{\rho_c}^{\rho(\zeta)} \frac{dp}{\sqrt{p^4 - \rho_c^4 - 2(p^2 - \rho_c^2)}}. \tag{4.2}$$

According to the thickness scaling paper published, it was seen that our experimental results did not fit the theoretical model proposed by Zembilgotov. [78] In a recent study, Kim *et al.* had found a similar outcome where the Zembilgotov model did not explain their thickness scaling experimental results for $BaTiO_3$ films. [65]

Li's model also used the Landau-Ginzburg-Devonshire theory to investigate the intrinsic effect in terms of phase instability. [58] Here, the depolarization effect was neglected because it argues that the surface charges were fully compensated for due to the presence of the top and bottom electrodes. In this model, the free energy of a ferroelectric cell can be expressed as,

$$\begin{aligned} G = \int_v \big[& \frac{\alpha}{2}P^2 + \frac{\beta}{4}P^4 + \frac{\gamma}{6}P^6 + \frac{D_{11}}{2}(\nabla_z P)^2 \\ & + \frac{D_{44}}{2}(\nabla_z P)^2 \frac{D_{44}}{2}(\nabla_x P)^2 + \frac{D_{44}}{2}(\nabla_y P)^2 \big] dV \\ & + \int_{s1} \frac{D_{11}\delta_3^{-1}}{2} P^2 dxdy + \int_{s2} \frac{D_{44}\delta_1^{-1}}{2} P^2 dzdy \\ & + \int_{s3} \frac{D_{44}\delta_1^{-1}}{2} P^2 dzdx, \end{aligned} \tag{4.3}$$

where $\alpha = \alpha_0(T - T_{c0})$ and T_{c0} is the normalized Curie temperature of the bulk crystal; and α, β, and γ are normalized coefficients of the Landau free energy expression. For the first order phase transition, the critical temperature of a size-driven phase transition can be approximately determined by

$$T_c^* = T_{c0} + \frac{3\beta^2}{16A_0\gamma} - \left[\frac{2D_{44}}{\alpha_0\delta_1} \left(\frac{1}{a_0} + \frac{1}{b_0} \right) + \frac{2D_{11}}{\alpha_0 c_0 \delta_3} \right], \tag{4.4}$$

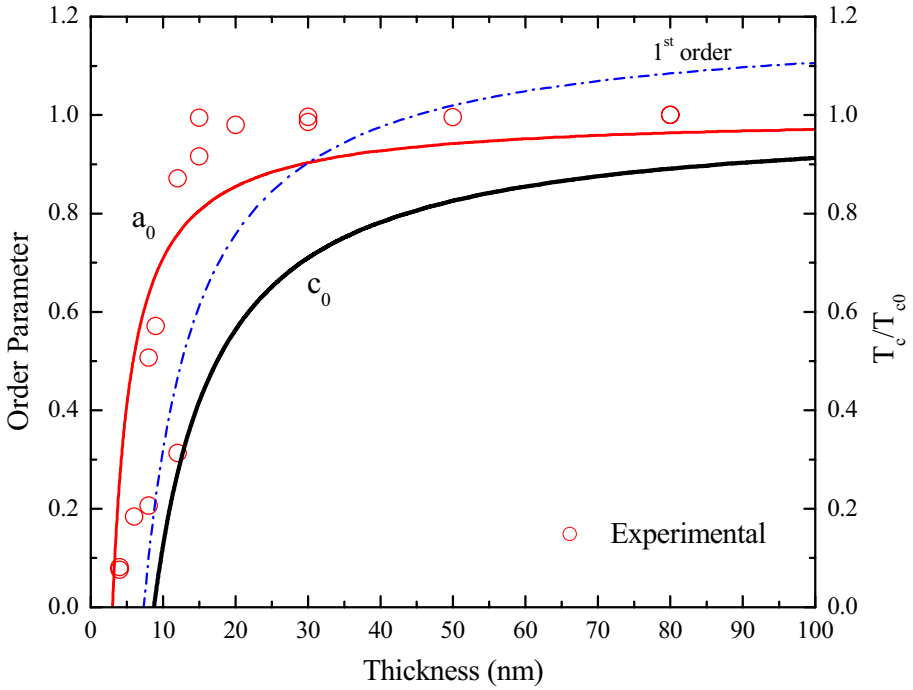

Figure 4.15: Theoretical fitting of Li's intrinsic model with the experimental data.

and the second order transition can be found by

$$T_c = T_{c0} - \left[\frac{2D_{44}}{\alpha_0\delta_1}\left(\frac{1}{a_0}+\frac{1}{b_0}\right)+\frac{2D_{11}}{\alpha_0 c_0\delta_3}\right]. \tag{4.5}$$

Figure 4.15 shows the comparison of the experimental results with Li's model undergoes the second order phase transformation where a_0=b_0 is the lateral dimension, and c_0 is the film thickness. In this figure, the 200 ns and 60 μs measurements were combined to give more data points for the fitting. There are three profiles plotted in this graph: i) a_0-second order, ii) c_0-second order, and iii) c_0-first order (indicated by a dashed line). The ferroelectrics described in this thesis undergo the second order transformation. Therefore, the c_0-second order profile is the most relevant. The other profiles were used merely for comparison. The theoretical comparison indicates that the polarization suppression of our film did not come from the intrinsic effects described by Li's model.

4.5.2 Depolarization model

In this section, we will be looking at the depolarization models proposed by Mehta, and Glinchuk. [5, 85] First, let's look at a depolarization model in more detail. As stated earlier, depolarization occurs from the incomplete cancelation between charges at the film-electrode interface, thus, generating an electric field opposing the direction of the polarization. This causes polarization suppression. Figure 4.16 shows the depolarization conditions of thin film showing a) boundary conditions, b) depolarization charges, and c) the potential profile across the capacitor and electrodes. Consider a thin film of ferroelectric material sandwiched between two metal electrodes as shown in Fig.4.16. The thickness of the ferroelectric is l and the thickness of each electrode is $\frac{1}{2}(L-l)$. Let the ferroelectric be poled to a polarization value P. This polarization induces compensation charges $\pm q_e$ in the metal electrodes. It is assumed that the ferroelectric is perfectly insulating and all the compensation charge resides in the electrodes. In the stand-by condition, the sample is short circuited. This approximates the usual condition during which the film is connected to a low-impedance source. Fig.4.16(b) and (c) schematically indicate the charge distribution and resulting potential distribution in the sandwich, respectively. It should be noted from Fig.4.16(c) that the electric field (slope of the potential) in the ferroelectric is non-vanishing and opposite to the polarization. This constitutes the depolarization field which we propose to be responsible for the poor retentivity observed in ferroelectric thin films.

The integrated charge at the electrode and the depolarization field can be calculated

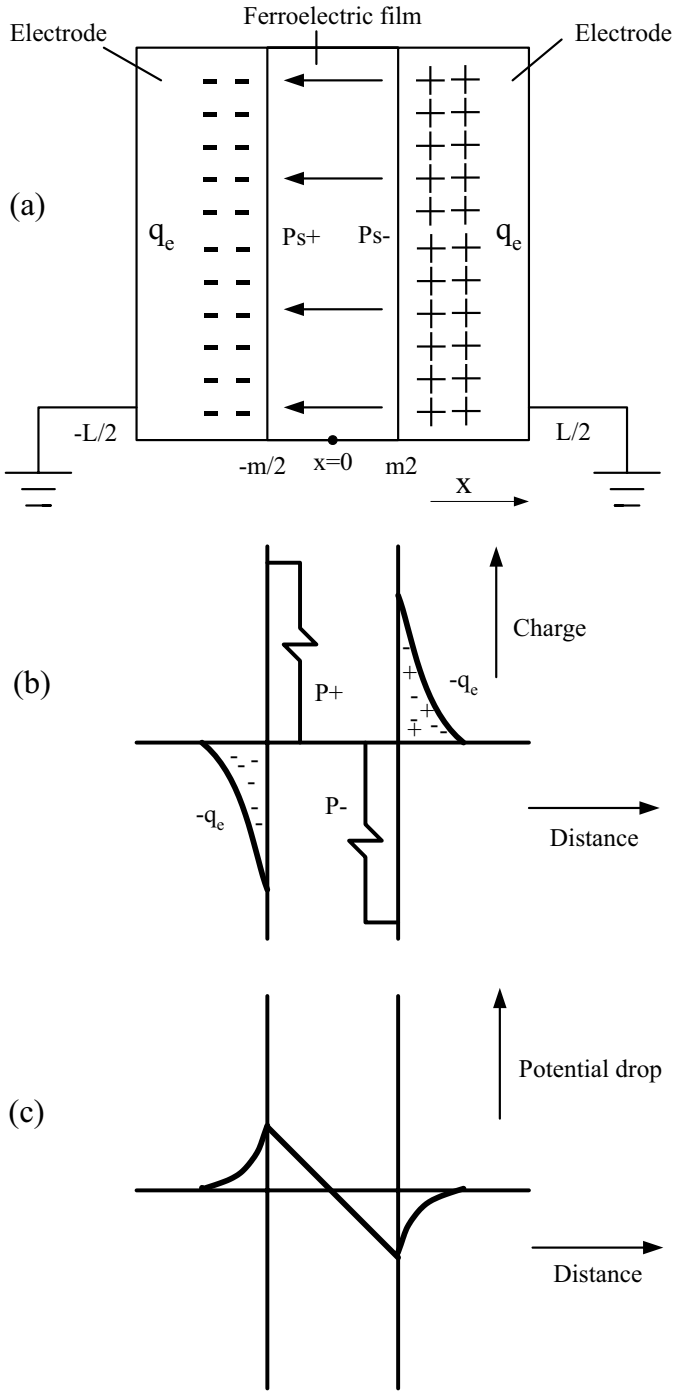

Figure 4.16: Depolarization conditions of thin film showing a) boundary conditions, b) depolarization charges, and c) potential profile across the capacitor and electrodes. [5]

from

$$q_e = -\theta P_s, \tag{4.6}$$

$$E_{dep} = -(P/\epsilon_F)(1-\theta), \tag{4.7}$$

where

$$\theta = \frac{\epsilon_e/\lambda}{2\epsilon_f/l + \epsilon_e/\lambda}. \tag{4.8}$$

These equations can be rearranged in terms of ϵ_f/ϵ_e as

$$E_{dep} = -\frac{2P_s}{\epsilon_e\epsilon_0}\frac{\lambda}{\left(l + 2\lambda\frac{\epsilon_f}{\epsilon_e}\right)}, \tag{4.9}$$

$$q_e = P_s\left[1 - \frac{2\epsilon_f}{\epsilon_e}\frac{\lambda}{\left(l + 2\lambda\frac{\epsilon_f}{\epsilon_e}\right)}\right], \tag{4.10}$$

where P_s = Spontaneous polarization, ϵ_0 = Relative permittivity = 8.8x10^{-12} F/m, l = film thickness, λ = Screening length, ϵ_f = Dielectric constant of thin film, ϵ_e = Dielectric constant of electrode. Equations 4.9, and 4.10 show that the values of E_{dep} and q_e were largely ϵ_f/ϵ_e dependent. Figure 4.17 shows the polarization profiles of different ϵ_f values; 60 [78], 200 [83], and 511 [84]. In all cases, the Mehta model shows that the polarization would vanish at zero thickness unlike in Li's case where the polarization disappears at 8 nm. Mehta's depolarization model did not show a good fit with the experimental data.

In Glinchuk's work, the depolarization model was obtained from the framework of the phenomenological theory. [86] It uses the same approach as Li by considering the free energy expression but with the addition of the depolarization contribution where

$$G = \frac{1}{l}\int_0^l \left[\frac{\alpha}{2}P_z^2(z) + \frac{\beta}{4}P_z^4(z) + \frac{\gamma}{2}\left(\frac{dP_z(z)}{dz}\right)^2 - E_z P_z(z)\right]dz$$
$$+ \frac{\gamma}{2l}\left(\frac{P_z^2(0)}{\delta_1} + \frac{P_z^2(1)}{\delta_2}\right) + 2\pi\left(\frac{1}{l}\int_0^1 P_z^2(z)dz - \left(\frac{1}{l}\int_0^1 P_z(z)dz\right)^2\right), \tag{4.11}$$

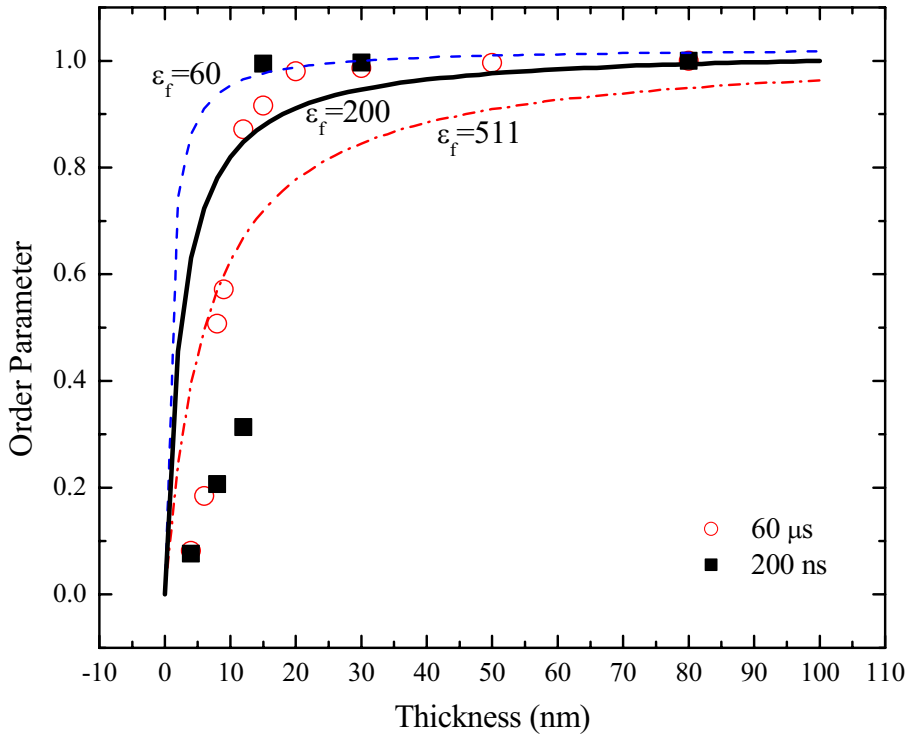

Figure 4.17: Theoretical fitting for depolarization of a different dielectric constant.

where l is the film thickness, α is the coefficient dependent of temperature, T_c is the Curie temperature, E_z is the external field, and δ is the extrapolation length. Here, the terms with $\gamma/2l$, and 2π represent the surface energy, and the depolarization energy, respectively. This is also known as the true coercive field. The derivative of the free energy expression from the equation gives the depolarizing field

$$E_z^d = -4\pi_P z + 4\pi \frac{1}{l} \int_0^l P_z dz \tag{4.12}$$

where the first and the second terms represent the depolarizing field of the film, and the compensating field of the free charges, respectively. Glinchuk derived the expression containing the relationship between the critical temperature and the film thickness as follows:

$$T_{cl} = T_c \left(1 - \frac{l_0^2(0)}{l}\left(\frac{1}{\delta_1 + l_d} + \frac{1}{\delta_2 + l_d}\right)\right), l_0(0) = \sqrt{\frac{\gamma}{\alpha_0 T_c}}. \tag{4.13}$$

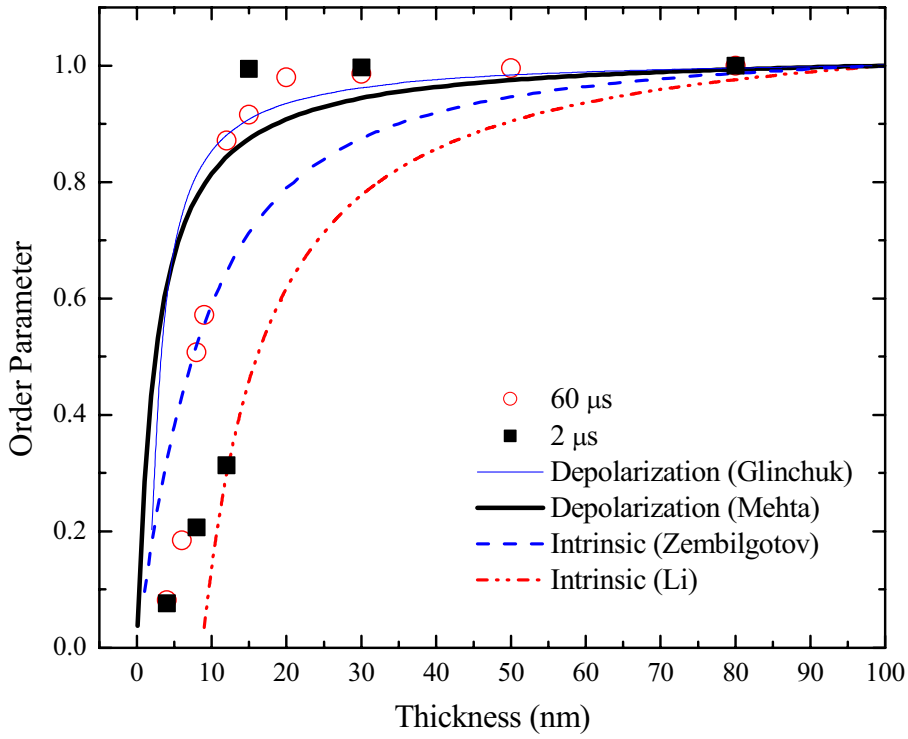

Figure 4.18: Comparison of the order parameter as a function of thickness with the theoretical prediction.

where $l_0(0)$ is the correlation length at zero temperature. Here we assume that δ_1=δ_2=δ. Therefore, the equation becomes

$$T_{cl} = T_c \left(1 - \frac{l_0^2(0)}{l}\left(\frac{1}{\delta + l_d}\right)\right), \tag{4.14}$$

where T_c=459.1°C, γ=2.475 $\times 10^8$m^9/C^{4}F, α=-12.84$\times 10^7$m/F, $l_d^2 = \gamma/4\pi$, and $\alpha_0 = \alpha/(T - T_c)$.[81]

Figure 4.18 summarizes all the theoretical predictions with the experimental results. Here, the solid circles are the experimental data, and the lines represent the theoretical calculations from the depolarization and intrinsic models. From the plot, it can be seen that the measurement data agrees closely with to the depolarization models by Mehta and Glinchuk. However, the measurement data of thinner films (<15 nm) falls closer to the intrinsic models. Therefore, this might suggest that it is possible that the cause of the

polarization suppression could be both depolarization and intrinsic effects. Kretschmer and Binder [75] show that the exponent ζ, related to the shift of the Curie temperature of thin film $T_{c(d)}$ relative to the bulk T_c, can indicate if the depolarization occurs where

$$\frac{T_{c(d)} - T_c}{T_c} \propto d^{-\zeta}, \tag{4.15}$$

and ζ=1 in the case with a depolarizing field. Therefore, plotting log($T_{c(d)} - T_c/T_c$) vs. log(d) gives the slope equal to ζ. In a recent paper by Nagarajan, it was shown that the modified Curie-Weiss law could be applied to relationship above (equation 4.15), and the slope = 1 was found. [78] It showed that the cause of polarization suppression was depolarization. Unlike Nagarajan's previous work, we obtained the Curie temperature ($T_{c(d)}$) of thin films directly from Pertsev's equation shown below without any modifications, and assume that the Curie temperature of the bulk remains constant. According to Pertsev, the relationship between $T_{c(d)}$ and the misfit strain S_m can be expressed as

$$T_{c(d)} = \theta + S_m \frac{4\epsilon_0 C Q_{12}}{s_{11} + s_{12}}, \tag{4.16}$$

where θ^*, and θ are the Curie-Weiss temperature of an epitaxial film, and the bulk, respectively, C is the Curie-Weiss constant, Q_{12} is the electrostrictive constant, and s_{ij} are the elastic compliances at constant polarization. According to Pertsev's phase diagram, Fig. 4.2 (temperature vs. misfit strain), the Curie-Weiss temperatures is the triple or quadruple point where all the phases meet. For the PZT (20/80) composition, the Curie-Weiss temperature was approximately equal to 460 °C. The values calculated from equation 4.16 were substituted into equation 4.15 to obtain the log($T_{c(d)} - T_c/T_c$) vs. log(d) relationship as shown in Fig. 4.19.

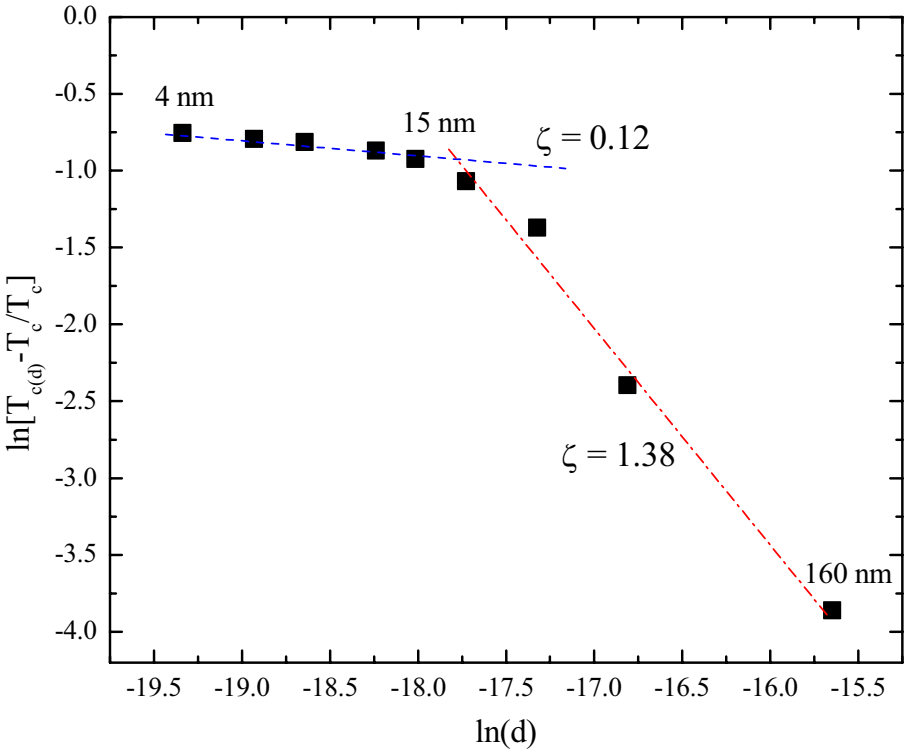

Figure 4.19: Plot of $\log(T_{c(d)} - T_c/T_c)$ vs. $\log(d)$ showing the transition of ζ as a function of thickness.

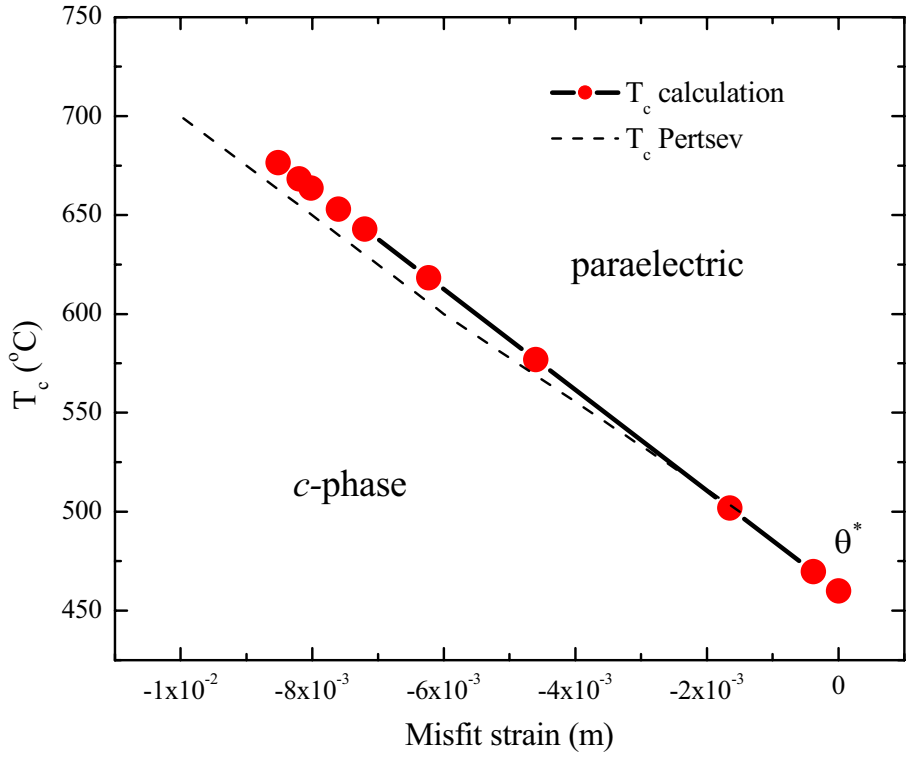

Figure 4.20: Plot of Curie temperature (T_c) as a function of misfit strain (S_m).

Here, we have found a very interesting result. Unlike the linear relationship shown by Nagarajan where ζ = 1, the plot of $\log(T_{c(d)} - T_c/T_c)$ vs. $\log(d)$ consisted of two slopes where ζ = 0.12 and 1.38, respectively. The deflection point where the slope changes indicate the critical thickness of 15 nm is where the ferroelectric suppression occurs. Furthermore, we have checked the accuracy of our calculated $T_{c(d)}$ values, and plotted them as a function of S_m, and found that they show a linear relationship where $T_{c(d)}$ increases as a function of S_m. This agrees with Pertsev's phase diagram (shown in Fig. 4.20).

4.5.3 Coercive Fields

The coercive field is a crucial factor in ferroelectric memory design since it determines the power used to switch a capacitor. In this section, we will look at how the coercive fields behave as a function of thickness reduction, and see if our experimental results agree with the theoretical predictions.

In general, ferroelectrics do not exhibit well-defined coercive fields. Their apparent thresholds strongly depend upon the length of time over which the field was applied.[3] As a result, it was important to distinguish between hysteresis data, typically obtained at a very slow rate (50 or 60 Hz), and displacement current transient data $I(t)$ obtained from switched capacitors on a 10-100 ns time scale. Except where otherwise noted, data reported here assumes driving voltages in the form of square pulses 200 ns wide, repeated approximately every 200 ns.[22] It should also be noted that in the measurements by AFM, the deviation of the coercive fields could also come from the experimental set up. In this case, it was found that peeling of the Pt-Ir coating from the AFM tip would cause a bad contact between the tip and the sample's top electrode. This results in a drop in

applied voltage, and an increase in the capacitor's coercive field.[28]

The coercive field of ferroelectrics can be calculated from the Ginzburg-Landau-Devonshire free energy expression where

$$G = \frac{\alpha}{2}P^2 + \frac{\beta}{4}P^4 + \frac{\gamma}{6}P^6, \tag{4.17}$$

and P_s can be found when

$$P_s = \frac{dG}{dP} = 0, \tag{4.18}$$

and E_c can be found when

$$E_c = \frac{dG}{dP}. \tag{4.19}$$

Typically, the theoretical E_c is much higher than the experimental (approximately 10-100 times higher). For example, for PTO_3, E_c theory = 1500 kV/cm and E_c observed = 100 kV/cm, and for $BaTiO_3$, E_c theory = 1000 kV/cm and E_c observed = 1 kV/cm [3]. The higher theoretical E_c is because the polarization reversal does not occur uniformly in ferroelectrics by dipole switching. For the PZT(20/80), using the values α, β, and γ from Table 4.1, and substituting them into equation 4.19, E_c(theoretical) was calculated to be 727 kV/cm. This value agrees with the theoretical approximation by Kim. [87] Kim *et al*. used the second derivative of the free energy expression where E_c=d^2G/dP^2. Kim's $E_c(theory)$ approximation is given as

$$E_c = \pm\frac{1}{3\sqrt{3}}\sqrt{\frac{\alpha^3}{\beta}} \tag{4.20}$$

where α = 1/2ϵ_f, $\beta \sim \alpha/P_s^2$, and P_s are the effective coefficient and spontaneous polarization, respectively. Using values of the coefficients obtained from Table 4.1, $E_c(theory)$ was calculated to be 761 kV/cm.

In Pertsev's work [88], $E_c(theory)$ was obtained from the nonlinear thermodynamic theory using the dielectric stiffness (a_{ij}). According to Pertsev, $E_c(theory)$ is given as

$$E_{th} = -8P_{cr}^3(a_{33}^* + 3a_{111}P_{cr}^2), \tag{4.21}$$

where critical polarization (P_{cr}), a_{33}^*, and a_{111} were calculated using the expressions given in Pertsev's papers. P_{cr} can be described as the minimum polarization which exists in an antiparallel electrical field. Using equation 4.21, P_{cr}, and E_c were calculated to be 40 μC/cm^2, and 1018 kV/cm, respectively.

Now, lets take a look at how the coercive field varies as a function of the film thickness. In the classical theory by Kay and Dunn (K-D), which is based on the Landau-Ginzburg theory, the relationship between the coercive field (E_c) and the film thickness (d) is given as E_c=$Ad^{-2/3}$ where A is a constant. The K-D theory is based on the assumption that there is no internal field in the ferroelectric film, and the coercive field measured externally across the electrodes is the same as the internal field inside the film. A logarithm plot of coercive field versus film thickness will give a linear fit of negative slope equal to 2/3. However, this only applies for low electric fields, and films of micrometer thickness. Figure 4.21 shows the experimental results of the coercive field measurements, and Fig. 4.22 shows the comparison between the theoretical predictions by Mehta (equation 4.7) and K-D, and the experimental results. [5, 6] From the experimental results, it can be seen that the coercive field increases as the film thickness decreases. At the film thickness of 80 nm, E_c was found to be 500 kV/cm but for a 4 nm thickness, E_c was found to be approximately 2000 kV/cm. This shows that the E_c increases by 4 times as

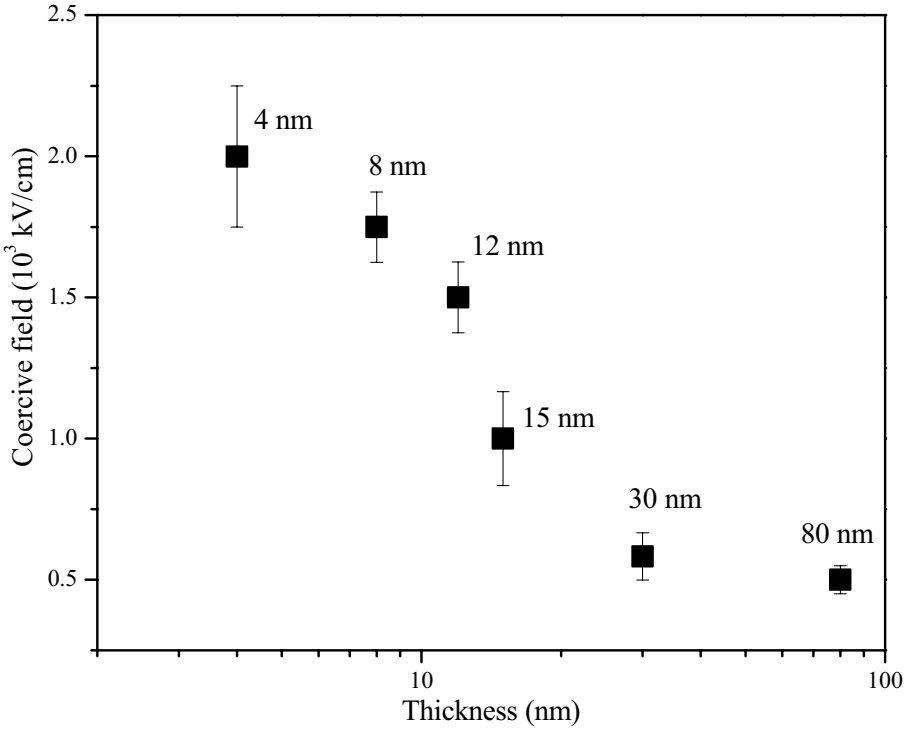

Figure 4.21: Coercive fields are plotted as a function of film thickness.

the film thickness is reduced to below 10 nm. Generally, the experimental results follow the same trend as the theoretical predictions. Although, the theories by Mehta and K-D show good agreement, and they suggest that E_c also increases as d decreases. However, they do not quite fit with the experimental data, but it can be seen that the experimental data follows the exponential decay function.

Figure 4.23 shows the plot of ln(E_c) vs. ln(thickness), where the slope was found to be -0.5. By substituting 0.5 into the K-D expression, we obtained data fitting with the experimental results where E_c(d)$\propto d^{-1/2}$. Although, this is a simple exponential decay function, it could describe the coercive field behavior as function of film thickness. The discrepancy between the K-D value of -0.66, and the fitting found here (-0.5) could be to the fact that the measurements in this thesis were done at the nanometers range, and there

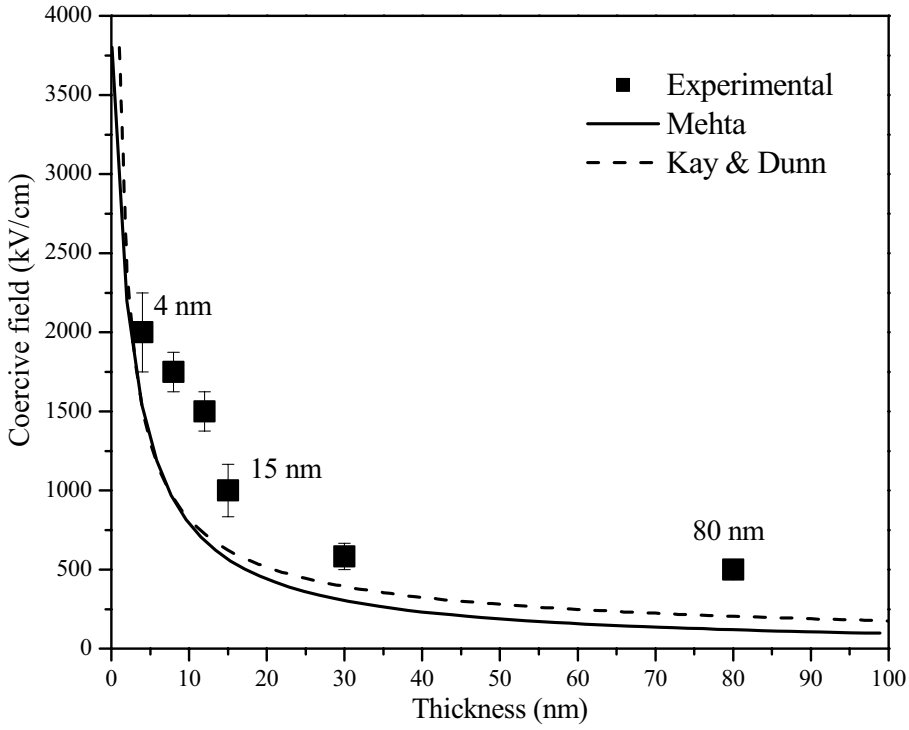

Figure 4.22: Comparison of experimental results with theoretical models from Mehta and Kay-Dunn. [5, 6]

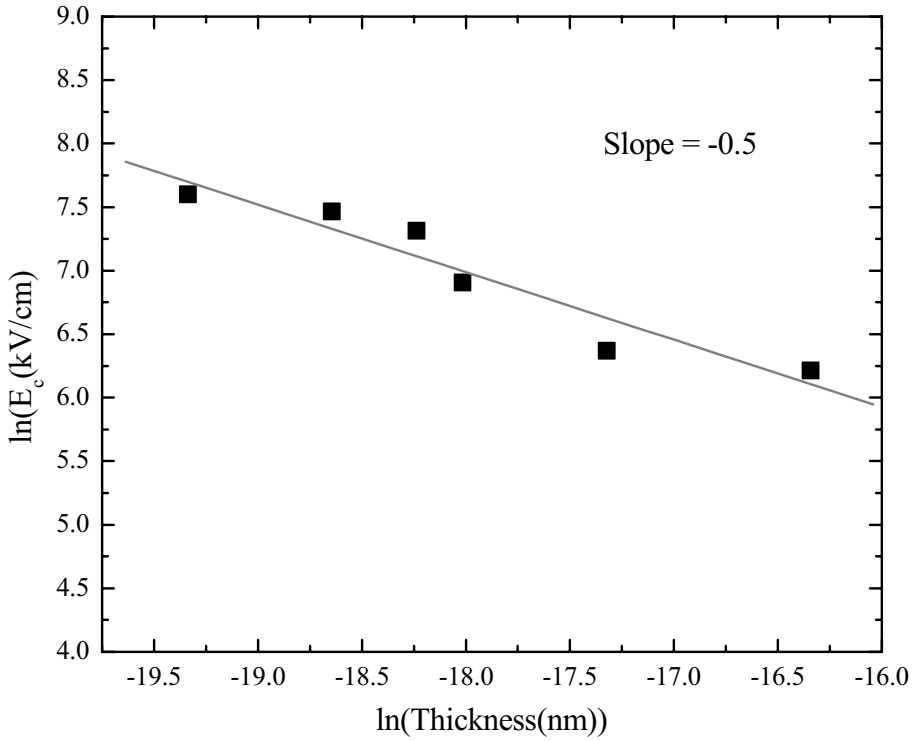

Figure 4.23: Plot of ln(E_c) vs. ln(thickness), where the slope was found to be -0.5.

could be circuit effects associated in the outcome of the E_c(experimental) values. The term $d^{-1/2}$ gives an excellent data but has no physical meaning. Figure 4.24 also shows the theoretical prediction by Dawber [6] which is given as

$$E_f = \frac{V + 8\pi P_s a}{d + e_f(2a)}, \tag{4.22}$$

where a=λ/ϵ_e. Dawber's expression is based on a simple relationship, E_c=V/d where V is the voltage measured across a capacitor. However, the expression includes two corrections: i) the depolarization field, and ii) electrode effects. Dawber suggested that as the film thickness is reduced below a certain thickness, depolarization will become more dominant. In addition, the screening length (according to the electrode effects consideration) will also contribute in coercive scaling. The results published by Dawber show a good agreement between the experimental results on the Polyvinylidene Fluoride (PVDF) ferroelectric film. Here, it was observed that there is a deflection point for the coercive field (from an increase to a decrease) at a film thickness of $\sim$2 nm which agrees with the experimental results. The deflection suggests the depolarization effects and polarization instability. However, from Fig. 4.24, it can be seen that Dawber's theory did not show a good prediction for our experimental results. The theory shows a good fit with the data above but not below the thickness of 15 nm. This suggests that the expression proposed by Dawber cannot be universally used with other films, and that the depolarization corrections were insufficient. There is another discrepancy between our results and Dawber's. Dawber suggested that the depolarization correction theory has two limitations where

$$E_f = \frac{V + 8\pi P_s \lambda/\epsilon_e}{d} if 4\pi P_s \gg \epsilon_f E \tag{4.23}$$

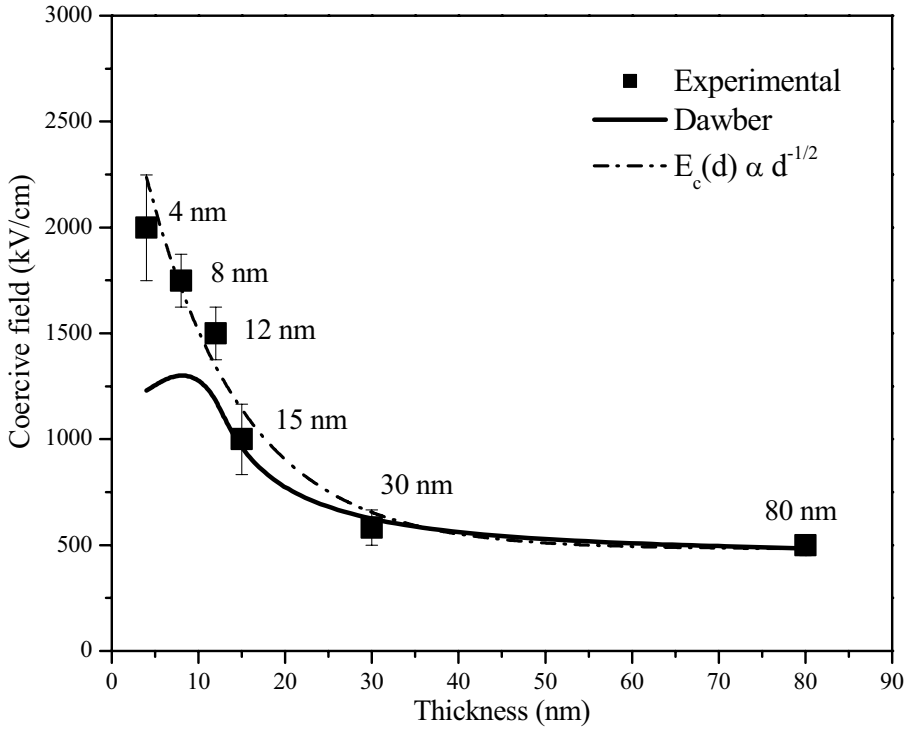

Figure 4.24: Fitting of the experimental data using Dawber's model and $d^{-1/2}$. Dawber's model did not fit the data at the thicknesses below 15 nm whereas the $d^{-1/2}$ expression shows a perfect fit.

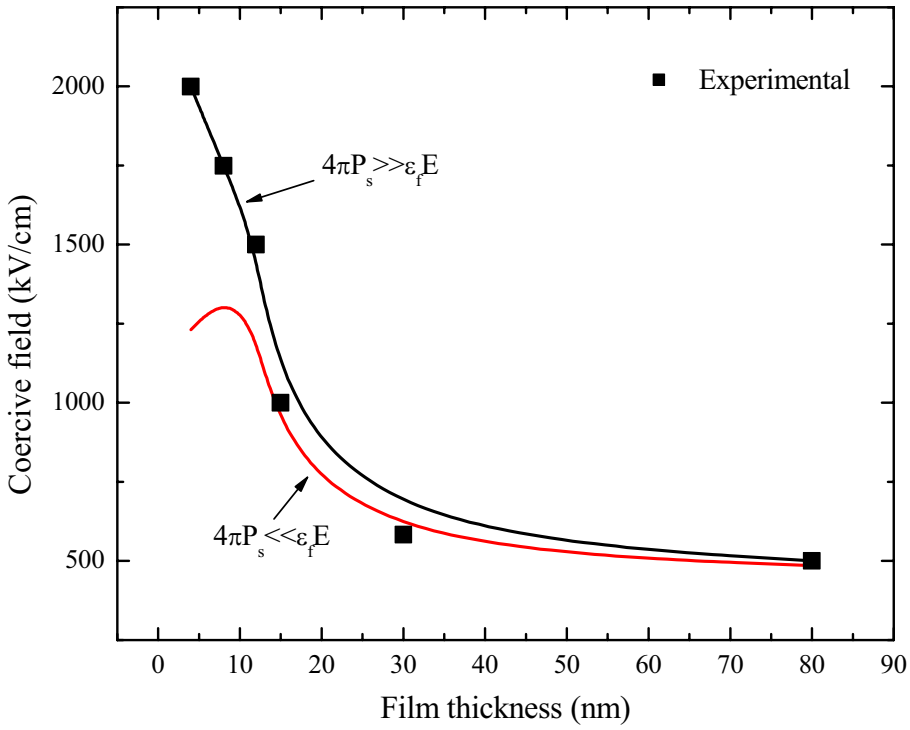

Figure 4.25: Coercive fields calculations with consideration of depolarization in the cases where $4\pi P_s \gg \epsilon_f E$ and $4\pi P_s \ll \epsilon_f E$.

, and

$$E_f = \frac{V}{d + (2\lambda)\epsilon_f/\epsilon_e} if 4\pi P_s \ll \epsilon_f E. \tag{4.24}$$

In Dawber's case, $4\pi P_s \gg \epsilon_f E$, and equation 4.23 applies, and gives the deflection curve. However, our calculations show that equation 4.23 applies to our results but gives the exponential decay curve (Fig. 4.25). This suggests that the we need to seek a theory to describe this thickness data.

4.6 Further Discussion

According to the measurements of the tetragonality of the PZT (20/80) films used in this study, it was found that the c/a ratio increased as the thickness decreased. This contradicts the fact that the higher c/a ratio gives a higher polarization (Fig. 4.26). If the c/a ratio

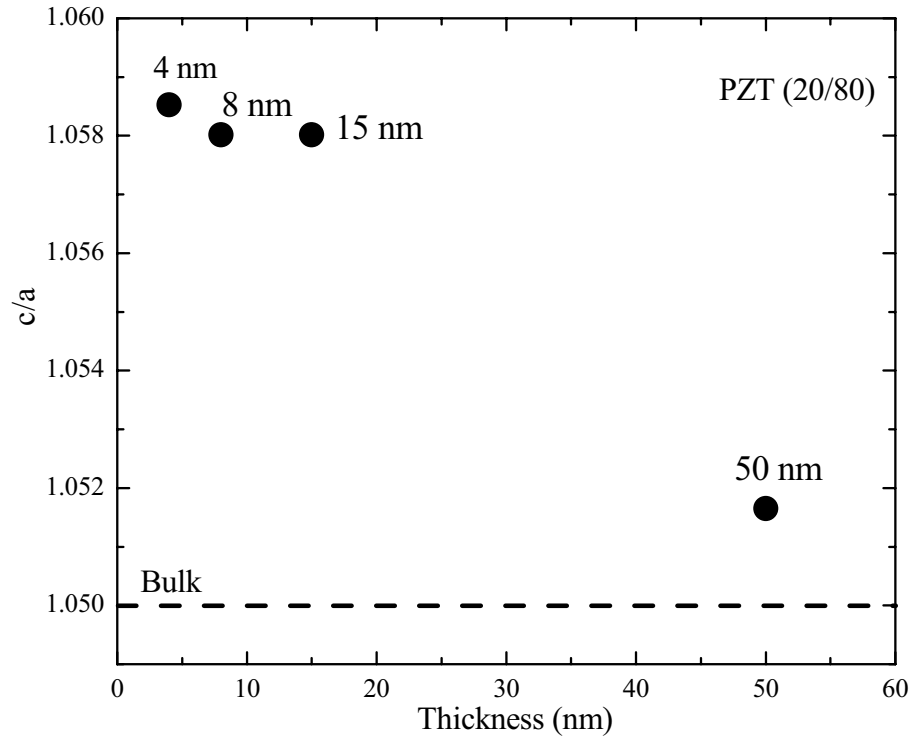

Figure 4.26: Tetragonality (c/a) measured as a function of thickness between 4 nm and 50 nm.

increases, we would expect that the polarization should increase. In the paper by Lichtensteiger, it was shown that the decrease of the tetragonality profile (normalized) agreed with the decrease in the polarization. [89] In the recent publication by Nagarajan, it was suggested that the pinned 180° domains are responsible for the ferroelectric decay. [77] Here, the voltage profile measured across the 4 nm thick sample shows the 0 V amplitude in the negative z-direction. This implies that the 180° domains only switch in the positive direction, and freeze in the negative. However, the measurement could be symmetrical but shifted along the y-axis. It can be seen that the shift even occurs at the 15 nm thickness (300mv +ve, 600mv -ve). In Yang's dissertation, the PFM measurements also showed the shift of the voltage profile in the positive direction, and there was no presence of the pinned domains. [90] Thus, it can be stated that measurement could be convoluted, and it

would be better if there is another piece of evidence to prove the existence of the pinned domains.

In thickness scaling studies, there has not yet been a publication that suggests the depolarization and intrinsic effects co-exist together, and both can contribute the ferroelectric decay as a function of thickness. Typically, the depolarization theory predicts that the polarization always goes to zero at zero thickness. However, it is also possible that the minimum thickness, shown by many intrinsic theories, does not necessarily have to be zero i.e. the minimum thickness where $\triangle P$ = 0 μC/cm^2 could be 4 nm. Figure 4.27 represents the idea of having the depolarization and intrinsic effects combined where

$$Suppression = Depolarization + Intrinsic. \tag{4.25}$$

4.7 Summary

This study of thickness scaling shows very interesting results. As the thickness was scaling from 100 nm to 4 nm, it was found that polarization suppression occurred at the thickness below 15 nm where the switching polarization showed a sudden drop from the bulk value of 140 μC/cm^2 to 11 μC/cm^2 for the 4 nm thick film. From the theoretical evaluations, it was found that either intrinsic effects and depolarization could be responsible for the suppression. In the coercive fields investigation, it was found that the coercive field was increased by approximately 4 times from 500 kV/cm to 2000 kV/cm for 80 nm and 4 nm, respectively. Although, the data can be fitted with the exponential term, $d^{-1/2}$, however this has no physical meaning.

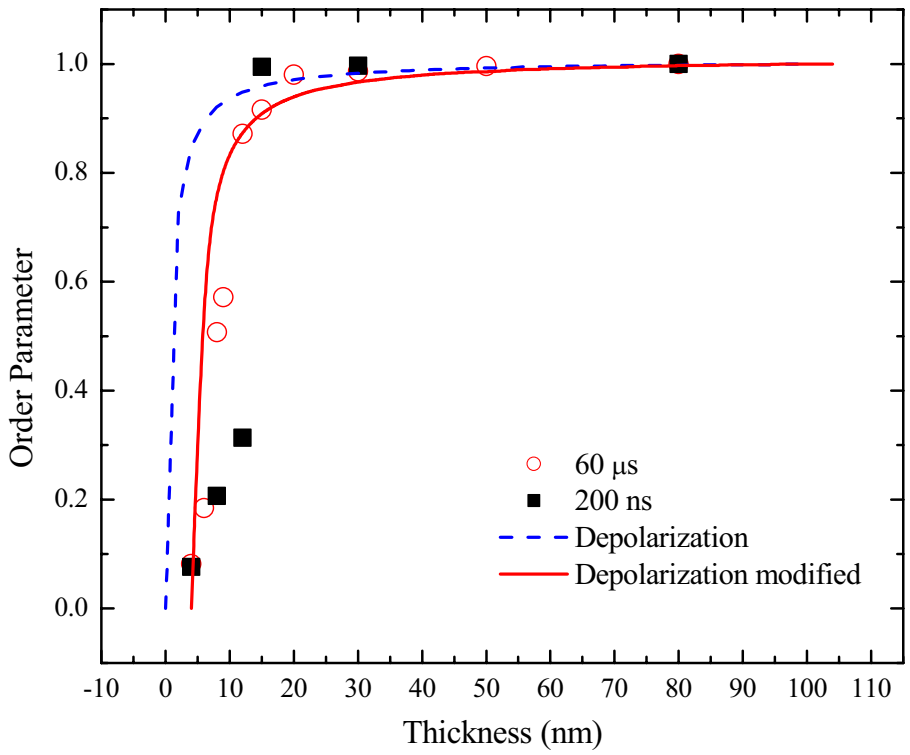

Figure 4.27: Modified depolarization model with intrinsic contribution.

Chapter 5

Conclusions and Further studies

The study on the lateral size effects revealed that there was no change in the switching polarization for the capacitor sizes investigated. The capacitors were well behaved as a function of lateral size scaling from 40000 μm^2 to 0.19 μm^2 where the switching polarization, $\triangle P \sim 30$ μC/cm^2, remained approximately the same for all capacitor sizes. However, the change of the intrinsic property was observed where activation field (α) was decreasing as the lateral size decreased. It was suspected the change of the intrinsic behavior was due to the circuit effects. Although, theoretical models could be fitting well with the transient data, the interpretation of the intrinsic properties found requires a better understanding and a careful analysis. The study of the film of different compositions, and exploration into a new theoretical model will be needed. It will be necessary, in the future, to investigate the interaction between the AFM tip-sample and the circuit effects in more depth.

The study of thickness scaling shows very interesting results. As the thickness was scaling from 100 nm to 4 nm, it was found that polarization suppression occurred at the thickness $\leq$ 15 nm where the switching polarization sharply decreased from the bulk value of 140 μC/cm^2 to 11 μC/cm^2 for the 4 nm thick film. From the theoretical evaluations, it was found that both the intrinsic effects and depolarization could be responsible for

the suppression. In coercive fields investigation, it was found that coercive field was increased by approximately 4 times from 500 kV/cm to 2000 kV/cm for 80 nm, and 4 nm, respectively. No critical thickness was observed but the coercive fields followed the exponential decay function of $d^{-1/2}$. The degradation behavior in thickness scaling prompts an urgent interest to improve the ferroelectrics fabrication so that the applicable ferroelectric properties can be maintained at the smaller dimensions to satisfy the scaling demand of ferroelectric devices from the industry.

In further studies, the lateral scaling should be investigated in terms of i) compositions of $PbZr_xTi_{(1-x)}O_3$, where x = 0.2, 0.4, 0.5, ii) processing (PLD vs. Sputtering vs. CVD), and iii) film structures (polycrystalline vs. epitaxial). During the course of my research, I have also investigated the switching properties of the epitaxial film $PbZrTiO_3$, and it would be possible to compare these results in further studies with the contents of the polycrystalline film in Chapter 3 (see Fig.5.1). This work is supported by National Science Foundation - Materials Research Science and Engineering Center (NSF-MRSEC).

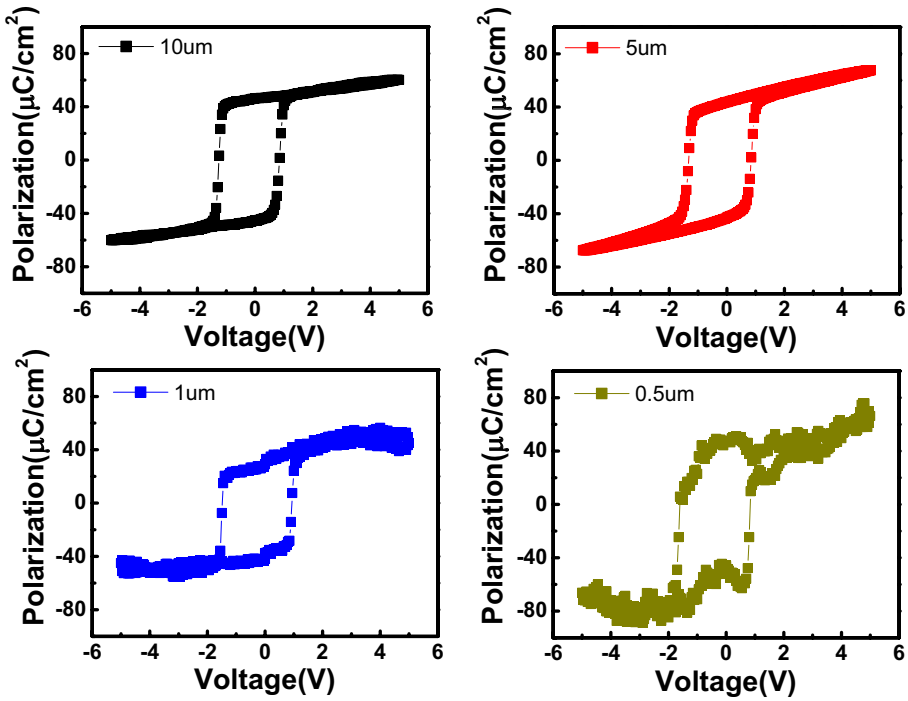

Figure 5.1: Hysteresis measurements as function of lateral scaling of epitaxial film $PbZrTiO_3$.

BIBLIOGRAPHY

[1] Ingrid G. Jenkins. *Switching Dynamics in Lead Based Thin Film Ferroelectrics*. PhD thesis, University of Maryland, 2000.

[2] M. E. Lines and A. M. Glass. *Principles and applications of ferroelectrics and related materials*. The international series of monographs on physics. Clarendon Press, Oxford, 1977.

[3] E. Fatuzzo and W. Merz. *Ferroelectricity*. North-Holland, Amsterdam, 1967.

[4] N. A. Pertsev, V. G. Kukhar, H. Kohlstedt, and R. Waser. Phase diagrams and physical properties of single-domain epitaxial $Pb(Zr_{1-x}Ti_x)O_3$ thin films. *Physical Review B*, 67:0541071 – 05410710, 2003.

[5] R. R. Mehta, B. D. Silverman, and J. T. Jacobs. Depolarization fields in thin ferroelectric films. *Journal of Applied Physics*, 44(8):3379–3385, 1973.

[6] M. Dawber, P. Chandra, P. B. Littlewood, and J. F. Scott. Depolarization corrections to the coercive field in thin-film ferroelectrics. *Journal of Physics: Condensed Matter*, 15:L393–L398, 2003.

[7] Walter J. Merz. Domain formation and domain wall motions in ferroelectric $BaTiO_3$ single crystals. *Physical Review*, 95(3):690–698, 1954.

[8] Bernard Jaffe, Jr. William R. Cook, and Hans Jaffe. *Piezoelectric ceramics*. Nonmetallic solids. A series of monographs. Academic Press Inc., London, 1971.

[9] Walter J. Merz. Switching time in ferroelectric $BaTiO_3$ and its dependence on crystal thickness. *Journal of Applied Physics*, 27(8):938–943, 1956.

[10] Robert C. Miller and Albert Savage. Velocity of sidewise 180° domain-wall motion in $BaTiO_3$ as a function of the applied electric field. *Physical Review*, 112(3):755–762, 1958.

[11] Robert C. Miller and Albert Savage. Further experiments on the sidewise motion of 180° domain walls in $BaTiO_3$. *Physical Review*, 115(5):1176–1180, 1959.

[12] H. L. Stadler. Ferroelectric switching time of $BaTiO_3$ crystals at high voltages. *Journal of Applied Physics*, 29(10):14851487, 1958.

[13] Ennio Fatuzzo. Theoretical considerations on the switching transient in ferroelectrics. *Physical Review*, 127(6):1999–2006, 1962.

[14] James F. Scott. *Ferroelectric memories*. Springer series in advanced microelectronics. Springer, Verlag Berlin Heidelberg New York, 2000.

[15] Yoshihiro Ishibashi and Yutaka Takagi. Note on ferroelectric domain switching. *Journal of the Physical Society of Japan*, 31(2):506–510, 1971.

[16] Melvin Avrami. Kinetics of phase change. I: General theory. *Journal of chemical physics*, 7:1103–1112, 1939.

[17] Melvin Avrami. Kinetics of phase change. II: Transformation-time relations for random distribution of nuclei. *Journal of chemical physics*, 8:212–224, 1940.

[18] Melvin Avrami. Kinetics of phase change. III: Granulation, phase change, and microstructure. *Journal of chemical physics*, 9:177–184, 1941.

[19] Adrijan Levstik, Marija Kosec, Vid Bobnar, Cene Filipic, and Janez Holc. Switching kinetics in thick film and bulk lead lanthanum zirconate titanate ceramics. *Japanese Journal of Applied Physics*, 36(Part 1, No. 5A):2744–2746, 1997.

[20] O. Lohse, M. Grossmann, D. Bolten, U. Boettger, and R. Waser. Relaxation mechanisms in ferroelectric thin film capacitors for feram application. *Integrated Ferroelectrics*, 33:39–48, 2001.

[21] Vladimir Shur, Evgenii Rumyantsev, and Sergei Makarov. Kinetics of phase transformations in real finite systems: Application to switching in ferroelectrics. *Journal of applied physics*, 84(1):445–451, 1998.

[22] J. F. Scott, L. Kammerdiner, S. Traynor M. Parris, V. Ottenbacher, A. Shawabkeh, and W. F. Oliver. Switching kinetics of lead zirconate titanate submicron thin-films memories. *Journal of Applied Physics*, 64(2):787–792, 1988.

[23] Hiroshi Ishiwara, Masanori Okuyama, and Yoshihiro Arimoto, editors. *Ferroelectric random access memories: Fundamentals and applications*. Topics in Applied Physics. Springer, Heidelberg, 2004.

[24] Hidemi Takasu. Ferroelectric memories and their applications. In *Insulating films on Semiconductors, 12th Bi-annual conference*, Udine, Italy, 2001.

[25] C. S. Ganpule, A. Stanishevsky, S. Aggarwal, J. Melngailis, E. Williams, R. Ramesh, V. Joshi, and Carlos Paz de Araujo. Scaling of ferroelectric and piezoelectric properties in Pt/$SrBi_2Ta_2O_9$ /Pt thin films. *Applied Physics Letters*, 75(24):3874–3876, 1999.

[26] S. Tiedke, T. Schmitz, K. Prume, A. Roelofs, T. Schneller, U. Kall, R. Waser, C. S. Ganpule, V. Nagarajan, A. Stanishevsky, and R. Ramesh. Direct hysteresis measurements of single nanosized ferroelectric capacitors contacted with an atomic force microscope. *Applied Physics Letters*, 79(22):3678–3680, 2001.

[27] Chandan S. Ganpule. *Nanoscale phenomena in ferroelectric thin films*. PhD thesis, University of Maryland, 2001.

[28] Klaus Prume, Andreas Roelofs, Thorsten Schmitz, Bernd Reichenberg, Stephan Tiedke, and Rainer Waser. Compensation of the parasitic capacitance of a scanning force microscope cantilever used for measurements on ferroelectric capacitors of submicron size by means of finite element simulations. *Japanese Journal of Applied Physics*, 41(Part1, 11B):7198–7201, 2002.

[29] S. Tiedke, T. Schmitz, K. Prume, A. Roedlofs, C. Szot, and R. Waser. In *Workshop on Polar Oxides*, Capri, Italy, 2003.

[30] Igor Stolichnov, Enrico Colla, Alexander Tagantsev, S. S. N. Bharadwaja, Seungbum Hong, Nava Setter, Jeffrey S. Cross, and Mineharu Tsukada. Unusual size effect on the polarization patterns in micron-size Pb(Zr,Ti)O_3 film capacitors. *Applied Physics Letters*, 80(25):4804–4806, 2002.

[31] Y. Kisler S. Collins S. D. Bernstein R. Hallock B. Armstrong J. Shaw J. Evans B. Tuttle B. Hammetter S. Rogers B. Nasby J. Henderson J. Benedetto R. Moore B. Pugh A. Fennelly S. Bernacki, L. Jack. Standardized ferroelectric capacitor testing methodology for nonvolatile semiconductor memory applications. In *Forth international symposium on integrated ferroelectrics (ISIF1992)*, Monterey, California, 1992.

[32] J. Li, B. Nagaraj, H. Liang, W. Cao, Chi. H. Lee, and R. Ramesh. Ultrafast polarization switching in thin-film ferroelectrics. *Applied Physics Letters*, 84(7):1174–1176, 2004.

[33] P. K. Larsen, G. L. M. Kampschoer, M. J. E. Ulenaers, G.A.C.M. Spierings, and R. Cuppens. Nanosecond switching of thin ferroelectric films. *Applied Physics Letters*, 59(5):611–613, 1991.

[34] Katsuhiro Aoki, Tomoyuki Sakoda, and Yuko Fukuda. Characterization of switching properties of lead-zirconate-titanate thin films in Ti-rich phase. *Japanese Journal of Applied Physics*, 37:L522–L524, 1998.

[35] Kazuhide Abe, Naoke Yanase, and Takashi Kawakubo. Asymmetric switching of ferroelectric polarization in a heteroepitaxial $BaTiO_3$ thin film capacitor. *Japanese Journal of Applied Physics*, 39(Part1, 7A):4059–4063, 2000.

[36] M. Grossmann, D. Bolten, O. Lohse, U. Boettger, R. Waser, and S. Tiedke. Correlation between switching and fatigue in $PbZr_{0.3}Ti_{0.7}O_3$ thin films. *Applied Physics Letters*, 77(12):1894–1896, 2000.

[37] P. K. Larsen, R. Cuppens, and G. J. M. Dormans, editors. Science and Technology of Electroceramics Thin Films. Kluwer Academic, Dordrecht, 1995.

[38] P. K. Larsen, R. Cuppens, and G.A.C.M. Spierings. Ferroelectric memories. *Ferroelectrics*, 128:265–292, 1992.

[39] H. Fujisawa and M. Shimizu. In *Proceedings of the 13th IEEE International Symposium on Applications of Ferroelectrics (ISAF 2002)*, page 4911, Nara, Japan, 2002. IEEE, New York, 2002.

[40] Alexei Gruverman. Scaling effect on statistical behavior of switching parameters of ferroelectric capacitors. *Applied Physics Letters*, 75(10):1452–1454, 1999.

[41] Jungwon Woo, Seungbum Hong, Nava Setter, Hyunjung Shin, Jong-Up Jeon, Y. Eugene Pak, and Kwangsoo No. Quantitative analysis of the bit size dependence on the pulse width and pulse voltage in ferroelectric memory devices using atomic force microscopy. *Journal of Vacuum Science and Technology B*, 19(3):818–824, 2001.

[42] *LabVIEWTM: Getting Started with LabVIEW*. National Instruments, Texas, USA, april 2003 edition, 2003.

[43] Dong Hoon Chang, Yung Sup Yoon, and Seong Jun Kang. Study of the switching characteristics of PLT thin films. *Journal of the Korean Physical Society*, 38(3):277–281, 2001.

[44] James F. Scott and Carlos A. Paz De Araujo. Ferroelectric memories. *Science*, 246(4936):1400–1405, 1989.

[45] James F. Scott. Limitations on ULSI-FeRAMs. *IEICE TRANS. ELECTRON.*, E81-C(4):477–487, 1998.

[46] Clare. D. McGllem and George R. Cooper. *Continuous and Discrete Signal and System Analysis*. Electrical Engineering, Electronics, and Systems. Holt, Rinehart, and Winston, Inc., New York, 1974.

[47] A. N. Kolmogorov. *A. N. Kolmogorov. On the papers on probability theory and mathematical statistics*, volume 2 of *Selected works of A. N. Kolmogorov: vol. 2 probability theory and mathematical statistic*. Kluwer Academic Publisher, the Netherlands, 1 edition, 1986.

[48] K. Dimmler, M. Parris, D. Butler, S. Eaton, B. Pouligny, J. F. Scott, and Y. Ishibashi. Switching kinetics in KNO ferroelectric thin-film memories. *Journal of applied physics*, 61(12):5467–5470, 1987.

[49] Masayoshi Omura, Takashi Mihara, and Yoshihiro Ishibashi. Simulations of switching characteristics in ferroelectrics. *Japanese Journal of Applied Physics*, 32(Pt. 1, No. 9B):4388–4391, 1993.

[50] M. Alexe, C. Harnagea, D. Hesse, and U. Gosele. Polarization imprint and size effects in mesoscopic ferroelectric structures. *Applied Physics Letters*, 79(2):242–244, 2001.

[51] S. B. Ren, C. J. Lu, J. S. Liu, H. M. Shen, and Y. M. Wang. Size-related ferroelectric-domain-structure transition in a polycrystalline $PbTiO_3$ thin film. *Physical Review B*, 54(20):14 337–14 340, 1996.

[52] V. Ya. Shur, S. D. Makarov, N. Yu. Ponomarev, V. V. Volegov, N. A. Tonkacheva, L. A. Suslov, N. N. Salashchenko, and E. B. Klyuenkov. Kinetics of polarization switching in lead zirconate-titanate epitaxial thin films. *Physics of Solid State*, 38(6):1044–1047, 1996.

[53] V. Ya. Shur and E. L. Rumyantsev. Kinetics of ferroelectric domain structure: Retardation effects. *Ferroelectrics*, 191:319–333, 1997.

[54] T. Tybell, P. Paruch, T. Giamarchi, and J.-M. Triscone. Domain wall creep in epitaxial ferroelectric $PbZr_{0.2}Ti_{0.8}O_3$ thin films. *Physical Review Letters*, 89(9):097601–1 – 097601–4, 2001.

[55] D. A. Porter and K. E. Eastering. *Phase Transformations in Metals and Alloys*. Chapman and Hall, London, second edition edition, 1992.

[56] R. Bruce Godfrey, J. F. Scott, H. Brett Meadows, Manooch Golabi, C. Araujo, and L. McMillan. Analysis of electrical switching in sub-micron KNO_3 thin films. *Ferroelectrics Letters*, 5:167–172, 1986.

[57] T. K. Song, S. Aggarwal, Y. Gallais, B. Nagaraj, R. Ramesh, and Jr. J. T. Evans. Activation fields in ferroelectric thin film capacitors: Area dependence. *Applied Physics Letters*, 73(23):3366–3368, 1998.

[58] S. Li, J. A. Eastman, Z. Li, C. M. Foster, R. E. Newnham, and L. E. Cross. Size effects in nanostructured ferroelectrics. *Physics Letters A*, 212(6):341–346, 1996.

[59] Y. G. Wang, W. L. Zhong, and P. L. Zhang. Lateral size effects on cells in ferroelectric films. *Physical Review B*, 51(23):17 235 – 17 238, 1995.

[60] V. Ya. Shur, S. D. Makarov, N. Yu. Ponomarev, V. V. Volegov, N. A. Tonkacheva, L. A. Suslov, N. N. Salashchenko, and E. B. Klyuenkov. Switching kinetics in epitaxial PZT thin films. *Microelectronic Engineering*, 29:153–157, 1995.

[61] V. Ya. Shur, E. L. Rumyantsev, and S. D. Makarov. Kinetics of polarization switching in finite-size ferroelectric samples. *Phys. Solid State*, 37(6):917–919, 1995.

[62] Y. W. So, D. J. Kim, T. W. Noh, Jong-Gul Yoon, and T. K. Song. Polarization switching kinetics of epitaxial $PbZr_{0.4}Ti_{0.6}O_3$ thin films. *Applied Physics Letters*, 86:092905–1 – 092905–3, 2005.

[63] S. Bhlmann, E. Colla, and P. Muralt. Polarization reversal due to charge injection in ferroelectric films. *Physical Review B*, 72:214120 – 7, 2005.

[64] Ph. Ghosez and K. M. Rabe. Microscopic model of ferroelectricity in stress-free $PbTiO_3$ ultra films. *Applied Physics Letters*, 76(19):2767–2769, 2000.

[65] Y. S. Kim, D. H. Kim, J. D. Kim, T. W. Noh, J. H. Kong, Y. D. Park, S. D. Bu, and J.-G. Yoon. Fabrication and thickness dependent properties of ferroelectric heterostructure. *Journal of the Korean Physical Society*, 46(1):55–58, 2005.

[66] Shaoping Li, Jeffrey A. Eastman, James M. Vetrone, Christopher M. Foster, Robert E. Newnham, and L. Eric Cross. Dimension and size effects in ferroelectrics. *Japanese Journal of Applied Physics*, 36(8):5169–5174, 1997.

[67] N. A. Pertsev, A. G. Zembilgotov, S. Hoffmann, R. Waser, and A. K. Tagantsev. Ferroelectric thin films grown on tensile substrates: Renormalization of the Curie-Weiss law and apparent absent of ferroelectricity. *Journal of Applied Physics*, 85(3):1698–1701, 1999.

[68] S. K. Streiffer, J. A. Eastman, D. D. Fong, Carol Thompson, A. Munkholm, M. V. Ramana Murty, O. Auciello, G. R. Bai, and G. B. Stephenson. Observation of nanoscale 180° stripe domains in ferroelectric $PbTiO_3$ thin films. *Physical Review Letters*, 89(6):0676011 – 0676014, 2002.

[69] C. L. Wang, Y. Xin, X. S. Wang, and W. L. Zhong. Size effects of ferroelectric particles described by the transverse ising model. *Physical Review B*, 67(17):11 423–11 427, 2000.

[70] Naoko Yanase, Kazuhide Abe, Noburu Fukushima, and Takashi Kawakubo. Thickness depedence of ferroelectricity in heteroepitaxial $BaTiO_3$ thin film capacitors. *Japanese Journal of Applied Physics*, 38:5305–5308, 1999.

[71] A. G. Zembilgotov, N. A. Pertsev, H. Kohlstedt, and R. Waser. Ultrathin epitaxial ferroelectric films grown on compressive substrates: Competition between the surface and strain effects. *Journal of Applied Physics*, 91(4):2247–2254, 2002.

[72] W. L. Zhong, B. D. Qu, P. L. Zhang, and Y. G. Wang. Thickness dependence of the dielectric susceptibility of ferroelectric thin films. *Physical Review B*, 50(17):12 375–12 380, 1994.

[73] A. V. Bune, V. M. Frikin, Stephen Ducharme, L. M. Blinov, S. P. Palto, A. V. Sorokin, S. G. Yudin, and A. Zlatkin. Two-dimensional ferroelectric films. *Letters to nature*, 391:874–877, 1998.

[74] T. Tybell, C. H. Ahn, and J.-M Triscone. Ferroelectricity in thin perovskite films. *Applied Physics Letters*, 75(6):856–858, 1999.

[75] R. Kretschmer and K. Binder. Surface effects on phase transitions in ferroelectrics and dipolar magnets. *Physical Review B*, 20(3):1065–1076, 1979.

[76] A. G. Zembilgotov, N. A. Pertsev, U. Bottger, and R. Waser. Effect of anisotropic in-plane strains on phase states and dielectric properties of epitaixial ferroelectric thin films. *Applied Physics Letters*, 86:052903–1 – 052903–3, 2005.

[77] V. Nagarajan, J. Junquera, J. Q. He, C. L. Jia, R. Waser, K. Lee, Y. K. Kim, S. Baik, T. Zhao, R. Ramesh, Ph. Ghosez, and K. M. Rabe. Scaling of structure and electrical properties in ultrathin epitaxial ferroelectric heterostructures. *Journal of Applied Physics*, 100:051609–1 – 051609–10, 2006.

[78] V. Nagarajan, S. Prasertchoung, T. Zhao, H. Zheng, J. Ouyang, R. Ramesh, W. Tian, X. Q. Pan, D. M. Kim, C. B. Eom, H. Kohlstedt, and R. Waser. Size effects in ultrathin epitaxial ferroelectric heterostructures. *Applied Physics Letters*, 84(25):5225–5227, 2004.

[79] Javier Junquera and Philippe Ghosez. Critical thickness for ferroelectricity in perovskite ultrathin films. *Nature*, 422:506–509, 2003.

[80] I. P. Batra, P. Wurfel, and B. D. Silverman. Depolarization field and stability considerations in thin ferroelectric films. *Journal of Vacuum Science and Technology*, 10(5):687–692, 1973.

[81] M. J. Haun, Z. Q. Zhuang, E. Furman, S. J. Jang, and L. E. Cross. Thermodynamic theory of the lead zirconate-titanate solid solution system, Part 3: Curie constant and sixth-order polarization interaction dielectric stiffness coefficients. *Ferroelectrics*, 99:45–54, 1989.

[82] Charles T. Black and Jeffrey J. Welser. Electric-field penetration into metals: Consequences for high-dielectric-constant capacitors. *IEEE Transactions on Electron Devices*, 46(4):776–780, 1999.

[83] Ryoichi Takayama and Yoshihiro Tomita. Preparation of epitaxial $Pb(Zr_{1-x}Ti_x)O_3$ thin films and their crystallographic, pyroelectric, and ferroelectric properties. *Journal of Applied Physics*, 65(4):1666–1670, 1989.

[84] A. Wu, P. M. Vilarinho, V. V. Shvartsman, G. Suchaneck, and A. L. Kholkin. Domain populations in lead zirconate titanate thin films of different compositions via piezoresponse force microscopy. *Nanotechnology*, 16:2587–2595, 2005.

[85] M. D. Glinchuk, E. A. Eliseev, and V. A. Stephanovich. The influence of depolarization field on dielectric and pyroelectric properties of ferroelectric films. *Semiconductor Physics, Quantum Electronics and Optoelectronics*, 5(2):142–151, 2002.

[86] M. D. Glinchuk, E. A. Eliseev, and V. A. Stephanovich. The depolarization field effect on the thin ferroelectric film properties. *Physica B*, 322:356–370, 2002.

[87] Sungwon Kim and Venkatraman Gopalan. Coercive fields in ferroelectrics: A case study in lithium niobate and lithium tantalate. *Applied Physics Letters*, 80(15):2740–2742, 2002.

[88] N. A. Pertsev, J. Rodriguez Contreas, V. G. Kukhar, B. Hermanns, H. Kohlstedt, and R. Waser. Coercive field of ultrathin $Pb(Zr_{0.52}Ti_{0.48})O_3$ epitaxial films. *Applied Physics Letters*, 83(16):3356–3358, 2003.

[89] Celine Lichtensteiger and Jean-Marc Triscone. Ferroelectricity and tetragonality in ultrathin $PbTiO_3$ films. *Physical Review Letters*, 94:047603–1 – 047603–4, 2005.

[90] Seung-Yeul Yang. *Complex Metal Oxide Thin Film Growth by Metalorganic Chemical Vapor Deposition*. PhD thesis, University of Maryland, 2005.